RECEIVED
APR 26 1961
NATIONAL LEAD CO., INC.
WINCHESTER, MASS.

Volume 7, No. 3
March, 1961

THE SOVIET JOURNAL OF

ATOMIC ENERGY

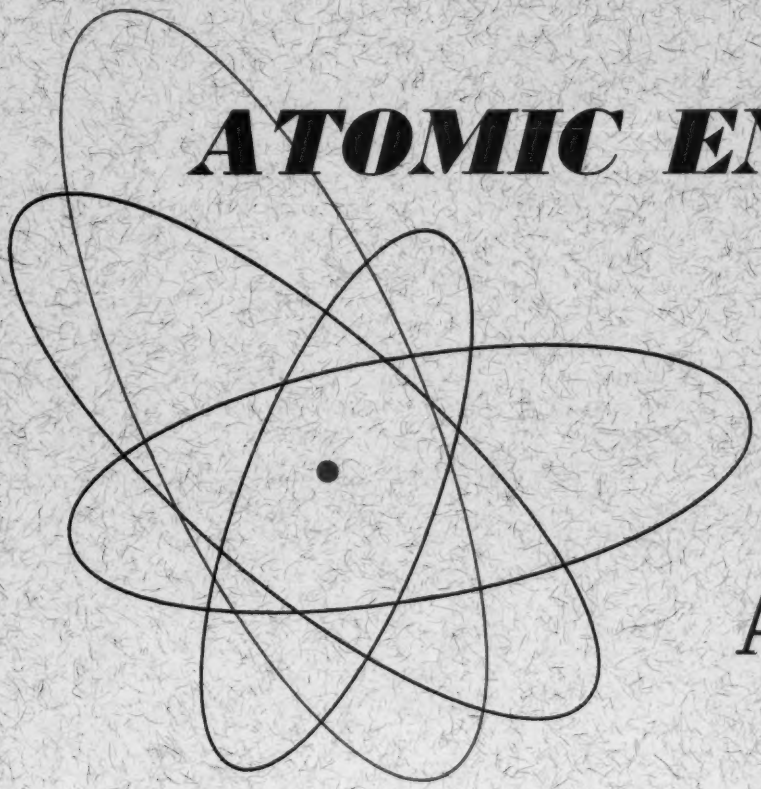

Атомная энергия

TRANSLATED FROM RUSSIAN

CONSULTANTS BUREAU

2 outstanding new Soviet journals

KINETICS AND CATALYSIS

The first authoritative journal specifically designed for those interested (directly or indirectly) in kinetics and catalysis. This journal will carry original theoretical and experimental papers on the kinetics of chemical transformations in gases, solutions and solid phases; the study of intermediate active particles (radicals, ions); combustion; the mechanism of homogeneous and heterogeneous catalysis; the scientific grounds of catalyst selection; important practical catalytic processes; the effect of substance – and heat-transfer processes on the kinetics of chemical transformations; methods of calculating and modelling contact apparatus.

Reviews summarizing recent achievements in the highly important fields of catalysis and kinetics of chemical transformations will be printed, as well as reports on the proceedings of congresses, conferences and conventions. In addition to papers originating in the Soviet Union, KINETICS AND CATALYSIS will contain research of leading scientists from abroad.

Contents of the first issue include:

Molecular Structure and Reactivity in Catalysis. A. A. Balandin

The Role of the Electron Factor in Catalysis. S. Z. Roginskii

The Principles of the Electron Theory of Catalysis on Semiconductors. F. F. Vol'kenshtein

The Use of Electron Paramagnetic Resonance in Chemistry. V. V. Voevodskii

The Study of Chain and Molecular Reactions of Intermediate Substances in Oxidation of *n*-Decane. Z. K. Maizus, I. P. Skibida, N. M. Emanuél' and V. N. Yakovleva

The Mechanism of Oxidative Catalysis by Metal Oxides. V. A. Roiter

The Mechanism of Hydrogen-Isotope Exchange on Platinum Films. G. K. Boreskov and A. A. Vasilevich

Nature of the Change of Heat and Activation Energy of Adsorption with Increasing Filling Up of the Surface. N. P. Keier

Catalytic Function of Metal Ions in a Homogeneous Medium. L. A. Nikolaev

Determination of Adsorption Coefficient by Kinetic Method. I. Adsorption Coefficient of Water, Ether and Ethylene on Alumina. K. V. Topchieva and B. V. Romanovskii

The Chemical Activity of Intermediate Products in Form of Hydrocarbon Surface Radicals in Heterogeneous Catalysis with Carbon Monoxide and Olefins. Ya. T. Eidus

Contact Catalytic Oxidation of Organic Compounds in the Liquid Phase on Noble Metals. I. Oxidation of the Monophenyl Ether of Ethyleneglycol to Phenoxyacetic Acid. I. I. Ioffe, Yu. T. Nikolaev and M. S. Brodskii

Annual Subscription: $150.00

Six issues per year – approx. 1050 pages per volume

JOURNAL OF STRUCTURAL CHEMISTRY

This significant journal contains papers on all of the most important aspects of theoretical and practical structural chemistry, with an emphasis given to new physical methods and techniques. Review articles on special subjects in the field will cover published work not readily available in English.

The development of new techniques for investigating the structure of matter and the nature of the chemical bond has been no less rapid and spectacular in the USSR than in the West; the Soviet approach to the many problems of structural chemistry cannot fail to stimulate and enrich Western work in this field. Of special value to all chemists, physicists, geochemists, and biologists whose work is intimately linked with problems of the molecular structure of matter.

Contents of the first issue include:

Electron-Diffraction Investigation of the Structure of Nitric Acid and Anhydride Molecules in Vapors. P. A. Akishin, L. V. Vilkov and V. Ya. Rosolovskii

Effects of Ions on the Structure of Water. I. G. Mikhailov and Yu P. Syrnikov

Proton Relaxation in Aqueous Solutions of Diamagnetic Salts. I. Solutions of Nitrates of Group II Elements. V. M. Vdovenko and V. A. Shcherbakov

Oscillation Frequencies of Water Molecules in the First Coordination Layer of Ion in Aqueous Solutions. O. Ya. Samilov

Second Chapter of Silicate Crystallochemistry. N. V. Belov

Structure of Epididymite $NaBeSi_2O_5OH$. A New Form of Infinite Silicon–Oxygen Chain (band) $[Si_4O_{10}]$. E. A. Podedimskaya and N. V. Belov

Phases Formed in the System Chromium–Boron in the Boron-Rich Region. V. A. Epel'baum, N. G. Sevast'yanov, M. A. Gurevich and G. S. Zhdanov

Crystal Structure of the Ternary Phase in the Systems Mo(W)–Fe(CO,Ni)–Si. E. I. Gladyshevskii and Yu. B. Kyz'ma

Complex Compounds with Multiple Bonds in the Inner Sphere. G. B. Bokii

Quantitive Evaluation of the Maxima of Three-Dimensional Paterson Functions. V. V. Ilyukhin and S. V. Borisov

Application of Infrared Spectroscopy to Study of Structure of Silicates. I. Reflection Spectra of Crystalline Sodium Silicates in Region of 7.5-15μ. V. A. Florinskaya and R. S. Pechenkina

Use of Electron Paramagnetic Resonance for Investigating the Molecular Structure of Coals. N. N. Tikhomirova, I. V. Nikolaeva and V. V. Voevodskii

New Magnetic Properties of Macromolecular Compounds with Conjugated Double Bonds. L. A. Blyumenfel'd, A. A. Slinkin and A. E. Kalmanson

Annual Subscription: $80.00

Six issues per year – approx. 750 pages per volume

Publication in the USSR began with the May-June 1960 issues. Therefore, the 1960 volume will contain four issues. The first of these will be available in translation in April 1961.

c/b CONSULTANTS BUREAU 227 W. 17 ST., NEW YORK 11, N. Y.

EDITORIAL BOARD OF
ATOMNAYA ÉNERGIYA
A. I. Alikhanov
A. A. Bochvar
N. A. Dollezhal'
D. V. Efremov
V. S. Emel'yanov
V. S. Fursov
V. F. Kalinin
A. K. Krasin
A. V. Lebedinskii
A. I. Leipunskii
I. I. Novikov
(Editor-in-Chief)
B. V. Semenov
V. I. Veksler
A. P. Vinogradov
N. A. Vlasov
(Assistant Editor)
A. P. Zefirov

THE SOVIET JOURNAL OF

ATOMIC ENERGY

A translation of ATOMNAYA ÉNERGIYA,
a publication of the Academy of Sciences of the USSR

(Russian original dated September, 1959)

Vol. 7, No. 3 March, 1961

CONTENTS

	PAGE	RUSS. PAGE
Ways of Saving Steel in Reactor Construction. A. N. Komarovskii	701	205
Intermittent Increase of Electron Current on a Probe During a Discharge in a Magnetic Field. A. V. Zharinov	710	215
On the Diffusion of Electrons in a Magnetic Field. A. V. Zharinov	715	224
Investigation of the Energy Characteristics of the External Proton Beam in the Six-Meter Synchrocyclotron. I. M. Vasilevskii and Yu. D. Prokoshkin	719	224
Phase Diagram of the Zirconium – Rhenium System. E. M. Savitskii, M. A. Tylkina, and I. A. Tsyganova	724	231
Extraction Properties of Diisoamyl Methylphosphinite. V. B. Shevchenko, I. G. Slepchenko, V. S. Shmidt, and É. A. Nenarokomov	728	236
Some Principles for the Design and Use of Powerful Irradiators. A. V. Bibergal', M. M. Korotkov, and T. G. Ratner	735	244
LETTERS TO THE EDITOR		
General Relation for Critical Thermal Loading. I. I. Nokikov	742	252
Influence of an Internal Heat Source on the Heat-Transfer Coefficient. S. S. Kutateladze, N. I. Ivashchenko, and T. V. Zablotskaya	743	253
Heat Transfer in Transverse Flow of Molten Sodium Around a Single Cylinder. A. A. Andreevskii	745	254
Gamma-Ray Spectrum of the IRT Reactor. I. V. Groshev, A. M. Demidov	748	257
Measurement of Radiative Capture Cross Sections of Fast Neutrons, Using Gallium Isotopes. Yu. Ya. Stavisskii, V. A. Tolstikov	750	259
Cascade γ Transitions in Cl^{36} Accompanying Thermal Neutron Capture. V. R. Burmistrov	752	260
A Large Alpha Spectrometer. S. M. Baranov, A. G. Zelenkov, G. Ya. Shchepkin, V. V. Beruchko, and A. F. Malov	756	262
Finding the Optimum Geometry of a Shielding Barrier. L. P. Kimel'	759	265
Angular Distribution of Radiation Emitted by Au^{198}, Scattered in the Air Above the Earth. V. N. Sakharov, V. I. Kolesnikov-Svinarev, V. A. Nazarenko, and E. I. Zabidarov	761	266
Gamma Rays Emitted in Inelastic Scattering of Neutrons at 3 Mev Energy. A. L. Androsenko, D. L. Broder, and A. I. Lashuk	763	268
The Effect of the Space Charge on the Motion of Particles in Accelerators. V. I. Kotov and V. A. Pushtarik	764	268

Annual subscription $75.00
Single issue 20.00
Single article 12.50

© 1961 Consultants Bureau Enterprises, Inc., 227 West 17th St., New York 11, N. Y.
Note: The sale of photostatic copies of any portion of this copyright translation is expressly prohibited by the copyright owners.

CONTENTS (continued)

	PAGE	RUSS. PAGE
Relation Between the Thermal Properties and the Atomic and Molecular Structure of Carbon in Homogeneous Graphitization. V. I. Kasatochkin, V. K. Zamoluev, and A. T. Kaverov	769	272
The Transport Equation in Isotope Separation Gear. G. Barvikh and R. Ya. Kucherov	772	275
The Internal Circulation of Extractables and Technological Design of an Extraction Column in Tributylphosphate extraction. A. M. Rozen	774	277
A New Graphical and Analytical Method for Calculating the Dose Field of Extended Sources. A. V. Bibergal'	779	281
NEWS OF SCIENCE AND TECHNOLOGY		
Sixth Session of the Learned Council of the Joint Institute for Nuclear Research. M. Lebedenko	783	285
Fourth Scientific and Technical Conference on Nuclear Electronics	783	285
New Items at the Exposition in the "Atomic Energy for Peaceful Purposes" Pavilion. V. Orlov	788	290
[Contour Activity of Boiling Reactor		294]
[Working Nuclear Fuel at Marcoule		277]
Brief Communications	792	299
BIBLIOGRAPHY		
New Literature	793	303

NOTE

The Table of Contents lists all material that appears in Atomnaya Énergiya. Those items that originated in the English language are not included in the translation and are shown enclosed in brackets. Whenever possible, the English-language source containing the omitted reports will be given.

Consultants Bureau Enterprises, Inc.

WAYS OF SAVING STEEL IN REACTOR CONSTRUCTION

A. N. Komarovskii

Translated from Atomnaya Énergiya, Vol. 7, No. 3, pp. 205-214
September, 1959
Original article submitted April 4, 1959

The basic methods for saving steel in reactor construction are considered in this article. It is shown that, in stationary nuclear reactors, the basic method for saving steel is its replacement with concrete. The article provides data indicating that the mechanical strength and the radiation resistance of concretes are not being utilized to the fullest extent at the present time, and that capillary cracks, which appear in concrete, do not affect its protective properties. The problem of the application of protective explosion-proof shells is considered. The project of the Soviet Boiling Reactor is described as an example proving the efficiency of using a protective chamber (instead of a protective shell) which is designed for excess internal pressure.

In reactor construction, a considerable saving of steel can be achieved by a rational and efficient design of the entire reactor plant.

Let us consider a few basic design approaches whereby such a saving could be secured:

1) the use of prestressed reinforced concrete instead of steel in the construction of the reactor vessel;

2) dispensing with thermal shielding (usually steel);

3) the use of the reactor chamber, which consists of reinforced-concrete side and top shielding, as an air-tight explosion-proof shielding instead of constructing a separate protective steel shell;

4) considerable reduction in or total dispensation with the reinforcement of concrete biological shield structures.

The Reactor Vessel

The thickness of concrete shields (usually 2-3 m), which is determined with respect to the maximum biologically allowable radiation level, is considerably greater than the thickness required for the static strength and rigidity of the chamber which is formed by the side and top reactor shielding.

In this case, the compressive stresses in protective concrete are several times smaller than the ultimate strength of the material. For instance, at the lower part of a 20 m high lateral shield made of ordinary concrete, the compressive stress is 4.6 kg/cm^2.

If such a shield were made of concrete with scrap steel, which would have a specific weight of 4.5 tons/m^3, the compressive stress would be 9.0 kg/cm^2.

The ultimate compressive strength of ordinary Concrete 300 of different compositions is ~ 140 kg/cm^2, and for concrete of different compositions with scrap steel, the ultimate compressive strength is 110-150 kg/cm^2 [1]. Thus, the compressive strength of concrete is not fully utilized in lateral shields, even in the case of very large reactors. For the most adverse thermal stress distribution, the safety factor will be reduced; however, it will still be equal to 3-7.

The safety factors in compression for the reactor top shield are somewhat smaller although still considerable.

Tensile stresses can arise as a result of temperature drops only in the outside shield layers. These stresses are small, and, in large reactors, they are usually borne by a small part of the steel reinforcement.

Ragardless of the fact that the concrete strength is utilized to such a small extent, a metallic (usually steel) vessel, which is subjected to considerable temperature stresses, is mounted inside the concrete chamber. This vessel is designed for possible accidental and, in certain reactor types, for operational internal liquid or gas pressures. In the majority of reactors, the pressure in the vessel does not exceed 15 atmos. The thermal stresses in the vessel can be considerable.

While the concrete in the lateral biological shield is mainly subjected to compression, the material of the steel vessel is under tensile stresses. Naturally, in the case of such a difference in stresses, the question arises whether concrete biological shield structures could be additionally stressed. By changing the shape and the dimensions of the chamber which is formed by the shielding, the chamber can be used as a pressurized vessel.

The maximum allowable tensile stress for concrete is small: for ordinary Concrete 300, it is equal to 10.5 kg/cm^2. The ultimate tensile strength of such concrete is ~ 30 kg/cm^2, and, for instance, for heavy Concrete 300 with scrap steel, it is 16 kg/cm^2 [2].

Obviously, without special measures and without transmitting the main portion of tensile stresses to the steel armature, ordinary concrete biological shield structures cannot withstand the assigned loads. One of such measures is the compression of concrete by means of the so-called prestressed (usually by means of jacks) armature (rods, high-strength wire, or steel cable). In recent years, prestressed concrete has been used in practice on an ever increasing scale.

However, in using prestressed reinforced concrete for reactor vessels, the following difficulties arise:

1. If a massive concrete biological shield is brought close to the reactor core, the thermal stresses in the shield become much larger.

2. Since reliable data on the behavior of structures made of prestressed reinforced concrete under conditions of violent temperature changes are not available, it is obviously necessary to secure large safety factors.

3. If the nonuniformity in heating is taken into account, the design of such a structure becomes very complicated. In this, possible errors for an isotropic body can yield not only quantitatively inaccurate results, but also qualitative deviations from the actual values (changes in the sign of stresses in concrete).

4. The great number of openings in the walls and the bottom of the vessel require a number of inserts, which complicates the construction of reinforced concrete structures.

These difficulties forced the joint Soviet-Czechoslovak Commission of Experts to reject an interesting project of a prestressed reinforced concrete vessel, which has been developed by Academician Bekhine of the Czechoslovak Academy of Sciences for the Czechoslovak Atomic Power Station A-1. Nevertheless, the commission of experts confirmed, in principle, the possibility of constructing such a vessel.

A perfectly gas-proof concrete cannot be prepared in practice, and therefore, the inside of the chamber must be lined with welded steel sheets which are fitted to the concrete and are not designed to withstand gas pressure. Such a steel casing can simultaneously serve as the internal lining in making a concrete vessel.

The advantages of a vessel made of prestressed reinforced concrete consist in the over-all saving of steel (taking into account the prestressed armature of reinforced concrete and the internal lining) and in being able to dispense with the complex work in the preparation of curved sheets, in their welding at the place of assembly, and in releasing thermal stresses arising in welding individual vessel parts. These advantages determined the application of such a vessel in French horizontal reactors G-2 and G-3 (Figs. 1 and 2).

The main reasons for not using an ordinary metallic vessel are the expected difficulties in welding and in the stress release of a cylindrical vessel 14 m in diameter and 18 m long. Calculations show that cracks in prestressed reinforced concrete in such a structure can arise only for internal pressures which are twice as large as the calculated pressure, i.e., for 30 atmos. The authors of the project consider that the provision of the necessary openings in the walls and the bottom of vessels is simpler when the latter are made of reinforced concrete. On the inside, the vessel has the shape of a cylinder which, at the bottom, passes into

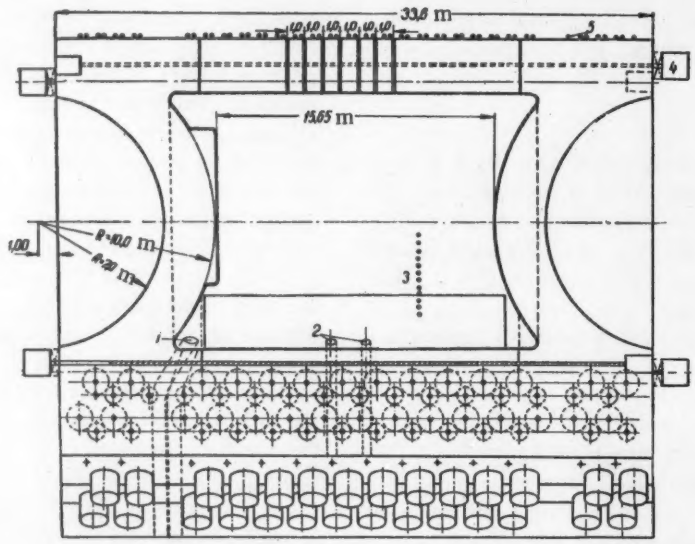

Fig. 1. Longitudinal cross section of the G-2 reactor vessel. 1) CO_2 inlet; 2) ionization chambers; 3) CO_2 outlet; 4) longitudinal cable; 5) transverse cables.

two inclined planes. In the authors' opinion, this makes the prestressing of reinforced concrete vessels easier.

Steel cables, made of strands of high-strength wire, serve as the armature securing the prestressing of concrete. Each cable was strained with a force of 1200 tons by means of jacks. Besides stressed cables, band armatures (hoops) were provided in the vessel concrete.

In order to provide an air-tight seal, the internal part of the vessel was lined with welded sheets of soft steel. This lining was fastened to the vessel concrete by means of a number of welded stays, and it permitted the mounting of the reactor inside the vessel simultaneously with the construction of its reinforced concrete part. The end faces of the vessel were covered with spherical reinforced concrete domes, each having a thickness of 3 m. The longitudinal forces acting on the end-face domes were carried by the longitudinal cable armature.

An over-all amount of 500 tons of armature of ordinary steel (besides the 2500 tons of steel for the base) and 760 tons of steel wire [2, 3] were used in constructing the vessel.

According to data in [4], due to the saving achieved by using a shield-vessel made of prestressed reinforced concrete, the construction costs were substantially reduced.

The above-mentioned indicates that steel can be saved by using reactor core chambers made of prestressed reinforced concrete, which serves as the biological reactor shield at the same time. However, the absence of convincing design estimates does not permit definite conclusions about the efficiency of this method.

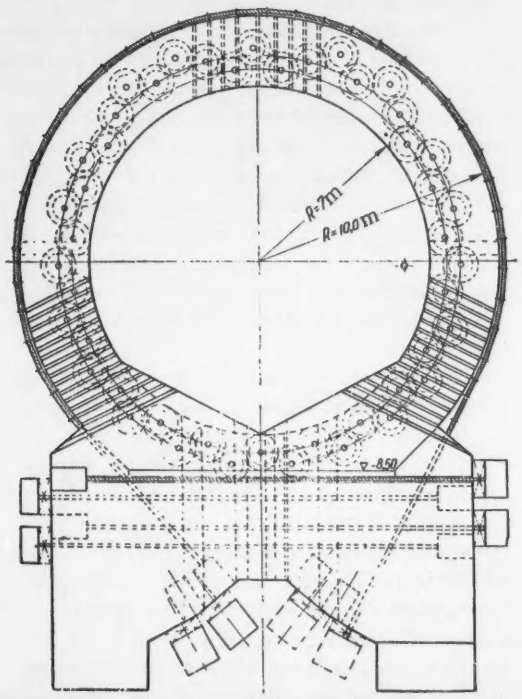

Fig. 2. Transverse cross section of the G-2 reactor vessel.

In reactors with a graphite moderator and a water coolant, which flows through pipes (i.e., in reactors without internal gas or liquid pressure exerted directly on the vessel), the construction of vessels made exclusively of reinforced concrete, which serves as the biological shield at the same time (without prestressed armature) is, in a number of cases, technically possible and provides a saving in steel. In this, the internal concrete layer (~ 50 cm thick) should be heat resistant, and the internal chamber surface should be lined with thin steel sheets in order to provide an air-tight seal; in the case where a steel thermal shield is provided, it should be combined with this lining.

The Thermal Shield

As a result of radiation heat release, the internal part of the reactor concrete shield can be heated to a considerable extent during operation. A thermal shield is used with the aim of reducing excessive heating of concrete (which causes large temperature stresses and sharply reduces the content of chemically bound water in concrete, due to which the protective properties of concrete deteriorate).

In the majority of cases, this shield consists of a low-carbon steel screen 15-20 cm thick. In individual cases, it is made of lead or of boron-containing materials. If considerable amounts of energy are released, thermal and biological shields are provided with artificial cooling. The weight of thermal shields is considerable. For instance, in the reactors of the English atomic power stations in Calder Hall and Berkeley, the weight of the steel thermal shields is 1925 and 4340 tons, respectively.

Sometimes the design of thermal shields is very complicated. For instance, in the experimental reactor FR-2 (German Federal Republic), the aluminum reactor vessel is surrounded with a thermal shield consisting of boral (7 mm) and steel (15 mm) layers which are cooled by circulating water, and of lead (60 mm), steel (35 mm), and iron (180 mm) layers, which are cooled by air.

However, the experience gained in the use of reactors and the results of a number of investigations give rise to serious doubts as to whether the application of thermal shields is justified. Their efficiency in bringing about a considerable reduction in the undesirable heating of concrete is not great.

Actually, a thermal shield can hardly affect the amount of heat transmitted from the reactor vessel to the concrete shield, and the amount of heat released in the concrete shield by the absorption of radiation in it is small. In the majority of cases, the procedure of constructing a thermal shield for a comparatively

small reduction in radiation fluxes incident on the concrete shield is not efficient.

In a number of papers from abroad, based on the experience in the design and operation of reactors, the authors take a skeptical attitude toward the advisability of using thermal shields. For instance, it is noted in [5] that, in the experimental reactor of the Brookhaven laboratory (USA), which is not provided with thermal shielding, no noticeable damage has been observed in the concrete shield, which is located in the immediate vicinity of the reactor core. Tests of concrete specimens cut from this shield showed that the strength and the moisture content of specimens have not decreased (it should be noted that the concrete shield of this reactor has an external bitumen insulation). In [6-8], it is also noted that dispensing with a thermal shield is possible and advisable from the point of view of saving material.

The use of thermal shields is mainly connected with the problem of stresses caused by heat release in the shield. Let us consider this problem in more detail.

Influence of Temperature on Concrete Strength

In a concrete shield, a relatively thin internal layer is subjected to highly intensive heating.

According to data from [6], the thickness of this layer is only a few centimeters. The temperature distribution throughout the concrete shield thickness is shown in Fig. 3 [9]. It follows from the figure that the use of a thermal shield shifts the temperature maximum toward the internal shield surface by only 0.15-0.20 m, i.e., only a distance equal to the usual thickness of steel thermal shields.

It was reported in [7] that, for a steady action of temperatures from 65-95° C on ordinary concrete, the deterioration of concrete strength is insignificant, and

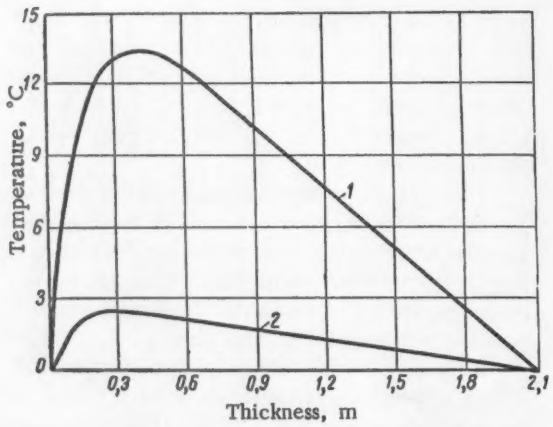

Fig. 3. Temperature distribution throughout the biological shield thickness. 1) without a thermal shield; 2) with a thermal shield.

even for temperatures in the 260-315° C range, the deterioration of structural properties of concrete in a number of shielding structures is considered to be admissible in the case of uniform heating. For limonite concrete, which is comparatively seldom used, a maximum allowable temperature limit of ~ 200° C is recommended regardless of the fact that, according to the performed experiments, the ultimate compressive strength of this concrete is reduced by only 5% at a temperature of 350° C. If the temperature is raised to ~ 600° C, the ultimate strength decreases by 35%. According to data from [7], for intensive and frequent temperature variations, the deterioration of concrete strength is two to three times greater than that resulting from a constant action of high temperatures.

Some other authors recommend somewhat lower maximum allowable concrete temperatures.

In [10], it is recommended to limit the temperature of ordinary concrete to 250° C. In this, it should be taken into account that the concrete strength can be reduced by 20-25% in prolonged heating in the temperature region of 100-250° C. It is recommended that the temperature of barite and limonite concretes be limited to 200° C, since, at temperatures from 100 to 200° C, capillary cracks appear in these concretes, and, at temperatures above 200° C, deformations which are more dangerous to the safety of structures can appear.

It is reported in [8] that limonite concrete can be used for the shielding of reactors at temperatures not exceeding 100° C.

The maximum allowable compressive strength of concrete at high temperatures (even for limonite concretes which are the weakest under high-temperature conditions) are considerably larger than the compressive stresses acting in lateral reactor biological shields. For instance, the ultimate compressive strength of 28-day old limonite concrete at a high temperature (540° C) is 47 kg/cm^2 even in the case of sharp and frequent temperature variations. At the same time, a compressive stress of 5.4 kg/cm^2 will be acting in a 20 m high shield wall made of limonite concrete [1].

If temperature stresses arising in concrete shields are taken into account, the safety factor for ordinary (nonlimonite) concrete will be not less than 3 or 4. Thus, the ultimate thermal stresses in the outside shield layer (usually carried by the armature) and the physicochemical processes in the heated concrete mass rather than the compressive stresses should be taken as the strength criteria for concrete shields at higher temperatures. In the worst case, both these factors can cause only nonthrough capillary cracks in the outside stretched concrete layer, which do not affect the compactness and the efficiency of concrete structures.

The top concrete biological shield of reactors represents a separate problem. In this case, the concrete

TABLE 1. Average Moisture Loss in Heating Different Types of Concrete to 100° C over a period of Seven Days.

Concrete	Moisture loss, %
Ordinary	5.1
Limonite	12.7
Magnetite	6.0
Barite	3.4
With scrap iron and sand	2.5
With scrap iron and limonite	1.7

(usually demountable slabs) is subject to bending and, consequently, tension, if it does not lie on a rigid frame.

The ultimate tensile strength of concrete is low, especially at higher temperatures. Thus, according to data from [7], in heating 120-day old limonite concrete from 85 to 350° C, the ultimate tensile strength is reduced by 30.5%. Therefore, concrete in the top shield, which is subject to bending, should be insulated against intensive heat, or an adequate reinforcement of the extension zone must be secured.

Effect of Capillary Cracks on the Protective Properties of Concrete

Experiments and calculations [8] show that cracks in concrete do not have geometrically smooth surfaces which would permit a penetration of radiation through the shield parallel to these surfaces. The surface of these cracks is rough and broken. In concrete, even a through crack 1.6 mm wide has a minimum deviation of 5 mm from a straight line [8]. The intensity of direct radiation through such a crack is small, and, on the whole, the radiation intensity at the outside shield surface in the capillary crack region is approximately the same as the intensity over the entire concrete surface.

Thus, the following conclusions on thermal stresses in concrete can be drawn:

1. In using ordinary high-quality concrete for biological protection, even in the case of powerful reactors operating under steady conditions, there is no danger that the concrete shielding would collapse or be damaged due to thermal stresses, including the case where thermal shields between the reactor vessel and the biological shield and a special cooling arrangement are not provided.

2. In using limonite concrete for the internal biological shield layer in reactors where the vessel temperature is in the range from 150 to 300° C, thermal shields or a cooling arrangement are apparently necessary. In certain cases, both these measures are necessary. Therefore, the use of limonite concrete for the internal shield layer is undesirable.

3. In the case of frequent and sharp temperature variations in the shield, it is advisable to apply thermal shielding or cooling of concrete or to use special heat-resistant types of concrete for the internal portion of the biological shield.

4. For the top concrete shield, which is subject to bending stresses, each individual case requires a study of the question whether it would be more efficient to lower the concrete temperature by installing a thermal shield or to provide suitable reinforcement of the concrete zone subject to tensile stresses.

Effect of Temperature on the Composition and Protective Properties of Concrete

heating concrete, its content of free and chemically bound water decreases. For different types of cement and fillers, and also for different concrete ages, these reductions are of unequal magnitude. The resultant deterioration of the ability of concrete to provide protection from neutron radiation along with a decrease in concrete strength is the main reason for the tendency to reduce the concrete temperature and to use special thermal shielding.

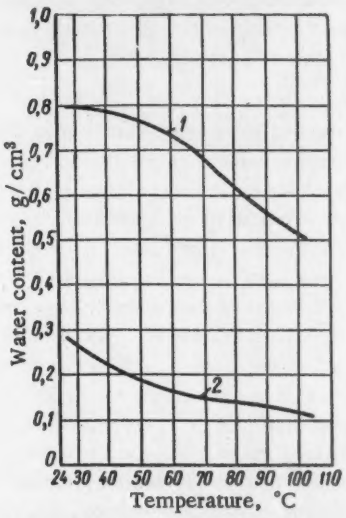

Fig. 4. Water content in cement gravel in dependence on temperature. 1) Magnesium hydroxychloride cement; 2) Portland cement.

TABLE 2. Temperature Dependence of the Amount of Chemically Bound Water in Cement Gravel

Specimen temperature, °C	Amount of water % by weight	Relative water Content, %
50	22,3	100
100	17,8	80
200	12,2	55
300	10,1	45,5
400	8,0	36,3
500	3,0	13,6
600	2,1	5,5

Figure 4 provides data on the water content in cement gravel in dependence on temperature [8], Table 1 provides data on the weight loss due to water evaporation in different concretes heated to 100° C [11], and Table 2 gives data characterizing the temperature dependence of the amount of chemically bound water in cement gravel consisting of ordinary sand and Portland cement [12].

It is reported in [13 and 14] that limonite ores can be considered as a water-containing material until their temperature reaches ~ 190-200° C.

Table 3 provides data obtained in investigating the moderation of neutrons in slabs made of concrete of different compositions and heated to different temperatures [15]. It follows from these data that the neutron relaxation length increases with an increase in concrete temperature. Similar data were obtained for ordinary and magnetite concretes [11]. Thus, with respect to moisture content, the use of thermal shielding or of biological shield cooling (or the simultaneous application of these measures) is justified only when the temperature of ordinary concrete exceeds 200-250° C or when the temperature of limonite concrete exceeds 100-150° C (with a certain margin).

Effect of Radiation on Concrete Strength

No systematic research data on the effect of radiation on the mechanical properties of concrete are available. Data on failure or damage in the concrete of biological shields of nuclear reactors or accelerators under the influence of radiation have not been recorded in practical work with nuclear reactors for peaceful purposes. Individual cases of shielding concrete deformations (capillary cracks) are mainly the consequence of the usual shrinkage or thermal stresses).

In experiments performed on the VERO reactor [15], it was established that ordinary concrete in shields can be utilized in operation over a period of at least ten years for a flux of 10^{11} neutrons/cm^2·sec. Experiments [16] showed that also concrete with Portland cement can sustain a certain damage if it is subjected to an integral flux of over 3×10^{20} neutron/cm^2 sec (or if subjected to γ radiation). (These data are based on a very small number of experiments and are not conclusive).

Comparative investigations of concrete specimens with a water-cement ratio of 1:3 and dimensions equal to 5 x 5 x 20 cm which were irradiated in a reactor (for a γ-radiation dose rate of 10^6 r/hr) and of specimens which were not irradiated showed that concrete is resistant to radiation [8]. These and a number of other data indicate that ordinary high-quality concrete has a good resistance to radiation. In individual cases, the omission of thermal shields will necessitate the use of somewhat thicker concrete biological shields; this, as a rule, is simpler and less expensive than the construction of thermal shields, and it provides a substantial saving in metal.

All the above-mentioned indicates that, in many cases, the necessity of providing thermal shields cannot be substantiated if a concrete biological shield of good quality is available. The application of special thermal shielding can be justified only in the case of high-temperature reactors.

Until the present time, heat-resistant concrete has not been used in reactor construction, although it has been mentioned in individual papers [17] that its application would be possible and efficient.

Considering that the maximum temperature point in concrete is at a distance of 0.35-0.40 m from the internal surface in the case where a thermal shield is not available, a layer of heat-resistant concrete 0.5-0.6 m thick would probably be sufficient. Beyond this layer, the effect of temperature and of the temperature drop, even in high-temperature reactors, would probably not affect the concrete shield strength (except in the region subjected to tensile stresses) and would not cause a considerable reduction in the moisture content. This relatively thin layer of heat-resistant concrete (even if it contains admixtures of finely ground red brick or a coarse filler of this brick) can reliably withstand temperatures of up to 700° C [12].

The somewhat lower specific weight of heat-resistant concrete in comparison with that of ordinary concrete (1.7 tons/m^3 versus 2.3 tons/m^3) will, in the worst case, necessitate a slight increase in the shield thickness (by only 13-14 cm). Such an increase in the concrete shield thickness will completely compensate the somewhat lower (in comparison with ordinary concrete) amount of chemically bound water in the heat-resistant concrete layer. Increasing the concrete shield thickness is obviously much less expensive than the use of a metallic thermal shield.

The Reactor Chamber

In using reinforced air-tight chambers which are formed by the concrete biological shields of the reactor proper as well as of steam generators (in power plants) as a protective shell, the lateral and the top concrete biological shields must be adequately designed for accidental excess internal pressures (usually not exceeding 3-3.5 atmos gauge). The requirement for air-tight

TABLE 3. Absorption of Fast Neutrons by Heated Concrete Slabs

Drying temperature, °C	Reinforced limonite concrete		Magnetite-limonite concrete		Magnetite concrete		Ordinary concrete	
	γ, g/cm^3	λ, cm	γ, g/cm^3	λ, cm	γ, g/cm^3	λ, cm	γ, g/cm^3	λ, cm
Initial	4,23	7,4	3,39	8,9	3,29	8,75	2,35	12,06
100	4,14	7,9	3,33	9,7	3,27	9,52	2,29	12,80
175	4,04	9,0	3,24	10,5	—	—	—	—
200	—	—	—	—	3,25	9,75	—	—
300	—	—	—	—	3,21	10,10	—	—
320	4,05	9,4	3,26	10,5	—	—	—	—

seals involves certain difficulties if openings, doors, etc. are present, however, this requirement can be satisfied.

If the reactor is built in a location with a mild climate, the reactor shell can be used as the housing for the entire plant, which obviously provides a saving in material. In locations with a moderate or northern climate, the use of a protective chamber calculated to withstand internal pressures and the simultaneous building of a reactor housing of the usual type can be more economical than the construction of a steel shell with heat insulation.

An example of the application of concrete shielding for these purposes is a boiling power reactor with a thermal power of 300 Mw (Fig. 5), which is under construction in the USSR. In this reactor, the reinforced concrete biological shield is used as the explosion-proof shield at the same time. In order to provide a better air tightness, the protective chamber is lined with ordinary sheet steel on the inside. All the reinforced concrete structures of the lateral and top biological shields are designed for an excess internal pressure of 3.5 atmos. A protective steel dome is mounted immediately above the reactor.

In order to increase the volume of the space to be filled with radioactive vapor in case of accident (for the purpose of reducing the vapor pressure), all the compartments of the first loop, which are adjacent to the reactor chamber are connected to it and to each other with membrane valves which operate when the pressure in any of the adjacent sections rises.

It was found that the utilization of the biological shield as a protective shield in case of accident necessitated an increase of 250-300 tons in the rein-

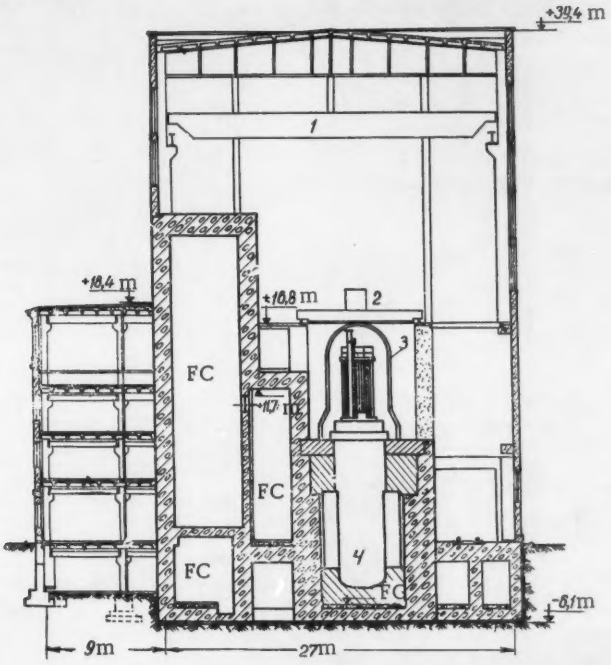

Fig. 5. Vertical cross section of the housing for the Soviet Boiling Reactor. 1) Bridge crane; 2) loading bridge; 3) reactor dome; 4) reactor; FC) chambers to be filled with radioactive vapor in case of accident.

forcement of concrete shielding structures, which amounted to ~ 50% of the armature weight in ordinary nonreinforced biological shielding and to 25-30% of the over-all amount of the armature material for all reinforced concrete housing structures, which is equal to ~ 1000 tons.

In order to determine the amount of metal to be used in the construction of a protective steel shell around the entire reactor plant, blueprints for the project of a spherical protective steel shell have been completed. Since the space which is filled with radioactive vapor in case of accident is larger than the space used for this purpose when only a protective concrete chamber is available, the theoretical pressure inside the shell was reduced to 2 atmos gauge. The diagram of such a sheet steel shell, which has a diameter of 50 m and a thickness of 35 mm, is shown in Fig. 6. The weight of sheet metal to be used in the construction of the shell is 2150 tons.

By comparing the two variants, it can be seen that, in using the biological shield structure as an accident-proof chamber, a 2.5-fold saving of metal in building construction can be achieved. It should also be taken into account that the variant with a steel shell requires a considerable amount of sheet steel (which is less readily available than structural armature steel) and that, moreover, the work in constructing the reactor housing becomes more complicated, especially if one considers the necessity of using a considerable amount of heat-insulation material for the entire steel shell even if the reactor is built in the moderate climatic belt of the USSR.

The Reinforcement of Concrete

As a rule, steel reinforcement is provided in the external zone of concrete biological shields. A considerable amount of reinforcement steel is required. For instance, in the large reactors at the English atomic power station at Hinckley Point, this amount is equal to several thousand tons.

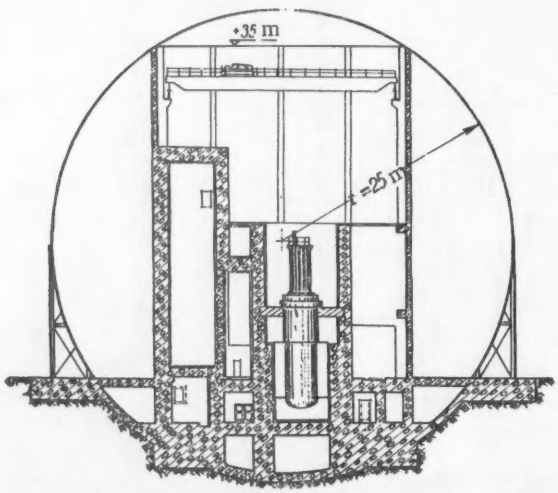

Fig. 6. Vertical cross section of the housing for the Soviet Boiling Reactor with an outside metallic protective shell (a variant of the project).

The reinforcement of concrete in shields is done in the first place because of the danger of excessive temperature stresses which would lead to the formation of capillary cracks and other concrete deformations.

In recent years, the reinforcement of concrete was based on calculations of stresses acting in concrete [7]. However, these calculations are not reliable, since sufficient experimental data on the temperature distribution throughout the thickness of a monolithic concrete shield are not available.

Reinforcement is often provided without any calculations. It was reported in [8] that, if the temperature drop throughout the concrete shield thickness does not exceed 30-50° C, special reinforcing of concrete is not necessary. For temperature drops of up to 90° C, the amount of reinforcing material must be substantially increased. In this case, according to the authors' opinion, the costs of additional concrete reinforcement and of constructing a special thermal shield should be compared in order to secure a most economical solution. For temperature drops of over 90° C, the reinforcement of concrete is impossible for constructional reasons, and, therefore, the temperature drop must be reduced by applying thermal shielding or cooling (or by using both these measures at the same time).

In [7], the following principles are recommended as guidance in calculating thermal stresses in reactor concrete shields:

1. If the cracking of nonreinforced concrete is to be prevented, the average shield temperature must not exceed the temperature of the shield cold side by more than 11° C.

2. In reinforcing the concrete shield region which is subjected to tensile stresses, the over-all allowable temperature drop (between the hot and the cold sides) can be increased to 67° C. For a nonlinear temperature distribution throughout the concrete thickness this drop must not exceed 55° C.

3. In the case of frequent temperature variations, it is recommended to limit the temperature drop to 22-28° C.

4. If the temperature drop increases to a considerable extent, a substantially heavier reinforcement must be provided. For instance, if the temperature drop increases from 70 to 100° C, the reinforcement must be increased by 0.2-1.6% (in order to avoid the formation of capillary cracks). Therefore, in certain cases, the provision of a thicker inner steel thermal shield or an intensification of artificial cooling of concrete is more economical than the use of a heavier reinforcement.

5. If pipes carrying a coolant at a temperature of 150-315° C pass through the concrete shield, an adequate cooling of the shield is sometimes impossible.

In this case, the concrete is usually enclosed in a carrying steel structure.

In the USSR, concrete and reinforced concrete shielding elements operating at a temperature of 100° C are designed according to the "Norms and Technical Requirements for the Design of Concrete and Reinforced Concrete Structures." For higher temperatures, the design is done according to the "Provisory Standards for the Design of Heat-Resistant Reinforced Concrete Structures." Nevertheless, up to now, sufficiently accurate methods of determining thermal stresses in unilateral heating of such massive concrete and reinforced concrete structures as biological shield structures ~2-3 m thick have not yet been developed.

From all the above data, the following conclusions can be drawn:

1. In connection with the fact that only a limited amount of data on the temperature distribution throughout the thickness of concrete biological shields is available, calculations of thermal stresses and of the necessary percentage of reinforcement in shields yield only provisory data. Therefore, suitable experiments and the development of methods for accurate calculations of stresses and concrete reinforcement are necessary.

2. A number of reactors which are in operation, including high-temperature reactors, are not provided with reinforced concrete or thermal shielding. However, no deformations have been observed in the shielding concrete in these reactors besides the appearance, in certain cases, of capillary cracks, which are not dangerous. Therefore, the recommendations of authors from abroad pertaining to limitations of temperature drops in concrete shielding for certain given amounts of reinforcement contain unjustifiably large safety factors, and they are not based on reliable calculations.

3. The slight reinforcement of the concrete biological shielding in the majority of reactors with low and medium temperatures can be dispensed with, and the reinforcement of the internal compressed protective zone is superfluous in all cases.

LITERATURE CITED

1. A. N. Komarovskii, Building Materials for Radiation Shields in Nuclear Reactors and Accelerators [in Russian] (Atomizdat, Moscow, 1958).
2. Description of Reactors G-2 and G-3. Report No. 1134, submitted by France to the Second International Conference on the Peaceful Uses of Atomic Energy (Geneva, 1958).
3. I. Bellier and M. Tourasse, Nuclear Energy Engr. 13, 11 (1959).
4. A. Baker, Indian Concrete J. 32, No. 12 (1958).
5. P. R. Stefenson, Introduction to Nuclear Techniques [in Russian] (Gostekhizdat, Moscow, 1956).
6. L. Ohlinger, Nucleonics 5, No. 4 (1949).
7. H. Davis, J. Structural Division 84, IX (1958).
8. B. Price, C. Horton, and K. Spinney, Radiation Protection [Russian translation] (IL, Moscow, 1959).
9. Atomic Power in England, No. 32. Collection of articles [Russian translation] (Atomizdat, Moscow, 1958).
10. K. D. Nekrasov, Heat-Resistant Concrete [in Russian] (Promstroiizdat, Moscow, 1957).
11. A. E. Desov, Heavy and Hydrated Concretes (Ts-NIPS Scientific Report) [in Russian] (Gostroiizdat, Moscow, 1956).
12. Chem. Eng. Progr. 51, 11 (1955).
13. H. Davis, Nucleonics 13, No. 6 (1955); H. Davis, Civil Eng. 26, No. 6 (1956).
14. H. Davis, F. Brawne, and H. Witter, J. Am. Concrete Inst. 27, 111 (1956).
15. D. Halliday, "Heat release in concrete reactor shield," Atomic Energy Research Establ. (Gr. Brit.) Rept. No. 1963, May (1956).
16. T. Rockwell, Nuclear Reactor Shields [in Russian] (IL, Moscow, 1958).
17. Nikolaus, Problems in Connection with Atomic Reactor Materials. Materials Used in Nuclear Engineering [in Russian] (Atomizdat, Moscow, 1957).

INTERMITTENT INCREASE OF ELECTRON CURRENT ON A PROBE DURING A DISCHARGE IN A MAGNETIC FIELD

A. V. Zharinov

Translated from Atomnaya Énergiya, Vol. 7, No. 3, pp. 215-219
September, 1959
Original article submitted February 13, 1959

An account is given of preliminary results in a study of the influence of a magnetic field on electron diffusion in a plasma. An intermittent increase was observed in the ratio of the electron current in the probe to the ion current at some critical value of the magnetic field intensity. According to the preliminary data, the critical magnetic field changes proportionally to the gas pressure. These facts evidently indicate the existence of two qualitatively different mechanisms for the transverse movement of the electrons, one of which is diffusion by collision.

One of the methods permitting the determination of the velocity with which electrons travel in the plasma across the magnetic field is the measurement of the ratio of the electron current on a probe to the ion current in regions of the discharge where it is possible to neglect the ionization. On the basis of such measurements, D. Bohm [1] formulated his hypothesis on the anomalously large electron transverse mobility. Although the mechanism of the Bohm diffusion of electrons is not clear, nevertheless, it can be assumed that it does not always take place, and that under some conditions the velocity of the ordinary electron diffusion by collision is sufficient to compensate the ionic space charge.

In order to verify this hypothesis, measurements were carried out, in the present work, of the ratio of the electron current in a probe to the ion current for different magnetic field intensities in the interval of 400-4500 oe.

Apparatus and Measuring Circuit

A diagram of the discharge apparatus is shown in Fig. 1. The discharge chamber consists of a cavity surrounded by a thick-walled copper cylinder C, whose end faces are closed by a molybdenum anode A and a diaphragm D. A heated cathode prepared by B. N. Makov was used in this work. The cathode proper consisted of a tungsten cylinder K, 5 mm in diameter, mounted on a special bracket on the cathode block B opposite an opening in the diaphragm 3 mm in diameter. The cathode was heated by the thermionic current from a tungsten filament N. In the anode, at a distance of 10 mm from its center, six holes were drilled, their diameters being 0.8, 1, 2, 3, 4, and 2 mm. At a distance of ~ 0.5 mm from the rear surface of the anode were mounted, opposite each opening, six

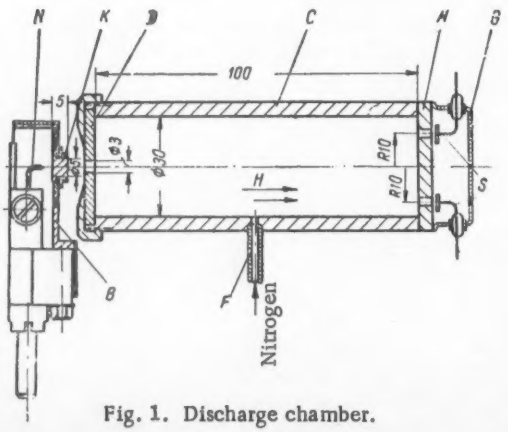

Fig. 1. Discharge chamber.

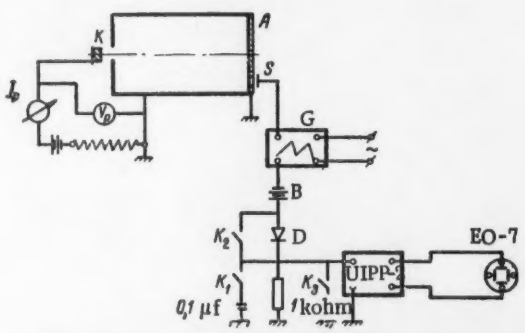

Fig. 2. Measuring circuit.

collectors S, which were used to take the probe characteristics. The collectors were fastened to the body of the shield G through glass insulators. Nitrogen was used as the working gas, and was let into the discharge cavity through tube F.

This arrangement was placed inside a metal vacuum chamber, which was set in the gap of the electromagnet and was evacuated by an oil diffusion pump which maintained during the continuous flow of the nitrogen in the discharge chamber, a vacuum inside it of $\sim 10^{-5}$ mm Hg. The pressure in the discharge chamber was approximately two orders greater.

Figure 2 shows the measuring circuit. Between the probe S and the anode A were connected in succession, a saw-tooth generator G and a measuring resistance R of 1 kohm. The dc component of the generator output voltage was compensated by a battery B, so that the potential of the probe could be changed symmetrically with respect to the anode. The signal was fed from the measuring resistance to the input of a direct-current amplifier UIPP-2, the output of which was applied directly to the plates of an ÉO-7 oscillograph.

To avoid linear distortion of the probe currents observed when the circuit operated at a high sensitivity the probe potential was not measured directly, i.e., the horizontal deflection of the oscillograph beam was obtained from a sweep generator of the oscillograph.

During all measurements the amplitude of the probe potential with respect to the anode was set at ~ 15 v. The measurements were made at a frequency of 50 cps. In the case of strong magnetic fields intensive oscillations always arose in the discharge, and the electronic part of the probe characteristic was very strongly modulated by oscillations at some tens of kilocycles per second. Under these conditions the measuring resistance was shunted by a capacitance of 0.1 μf by means of switch K_1, and thus, the characteristic was averaged over the high-frequency component of the probe current.

In those cases when the electron current exceeded the ion current by more than 20-30 times a more correct measurement of the ratio of the electron current to the ion current was obtained by measuring the latter under a greater amplification than that of the electron current. In this way, the opening of switch K_2 connected in the detector D_1 and the electron current was detected to remove the overload on the amplifier.

Switch K_3, shunting the input of the amplifier, was used to obtain the zero-current line during the photographing of the probe characteristics.

Results of the Measurements

Figure 3 presents a number of oscillographs of the probe characteristics corresponding to a discharge current of 1 amp, a discharge voltage of 180 v, and a

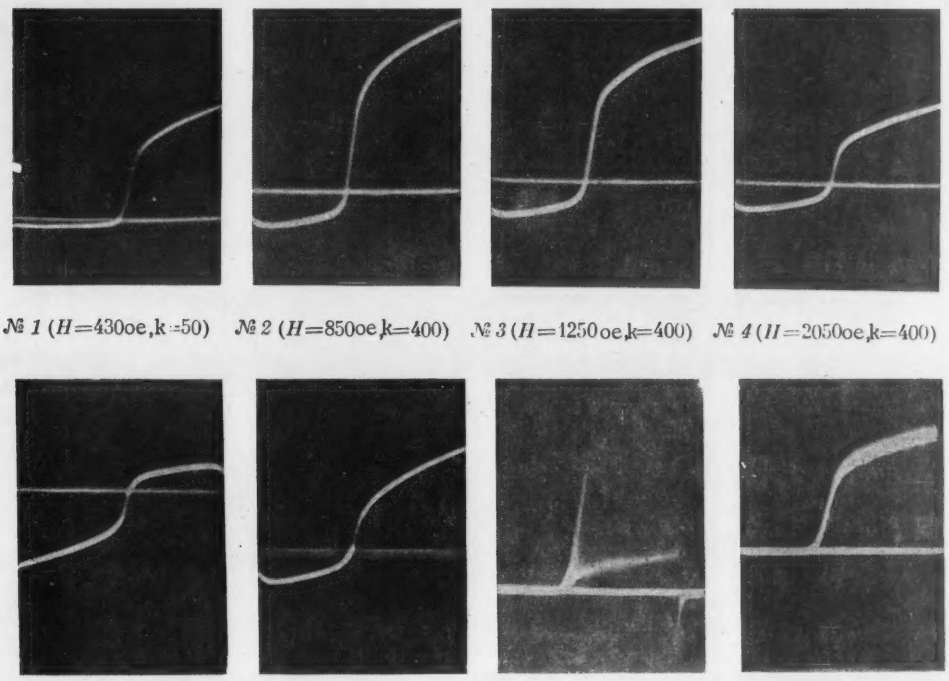

№ 1 (H=430oe, k=50) № 2 (H=850oe, k=400) № 3 (H=1250oe, k=400) № 4 (H=2050oe, k=400)

Fig. 3. Oscillograms of probe discharge characteristics for different magnetic-field intensitites H (k is the amplification factor).

pressure in the vacuum chamber of $7 \cdot 10^{-5}$ mm Hg. In this case, the pressure in the discharge chamber was $(2-3) \cdot 10^{-3}$ mm Hg. These characteristics were obtained for a probe diameter of 3 mm, the remaining probes were grounded. Oscillograms Nos. 1-7 were taken without the capacitance shunting the measuring resistance.

In examining these oscillograms, one may note the absence of oscillations both of the ion current (lower branches of the curves) and of the electron current (upper branches of the curves) for a magnetic-field intensity of < 3000 oe. However, in a magnetic field only a little stronger than 3000 oe (oscillogram No. 7) there arises a very strong oscillation in the electron current of the probe. At the same time, oscillograms Nos. 1-7 show quite distinctly that there is a steady decrease in the ratio of the electron current to the ion current as the magnetic field increases.

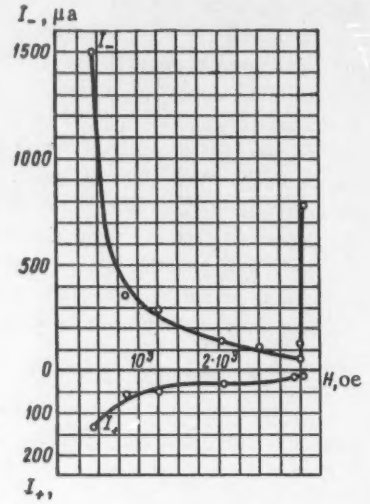

Fig. 4. Variation of electron current I_- and ion current I_+ in the probe with magnetic-field intensity. Probe diamter D_S = 3 mm; I_p = 1 amp; V_p = 180 v; p = $7 \cdot 10^{-5}$ mm Hg.

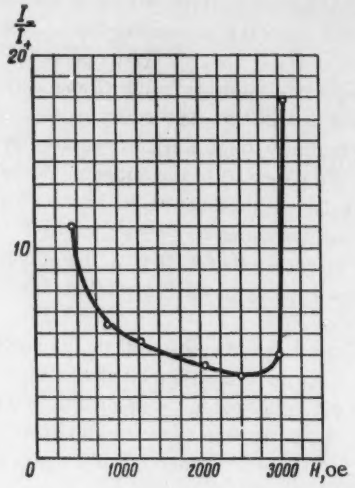

Fig. 5. Variation of ratio I_-/I_+ with magnetic-field intensity (from data of Figs. 3 and 4). D_S = 3 mm; I_p = 1 amp; V_p = 180 v; p = $7 \cdot 10^{-5}$ mm Hg.

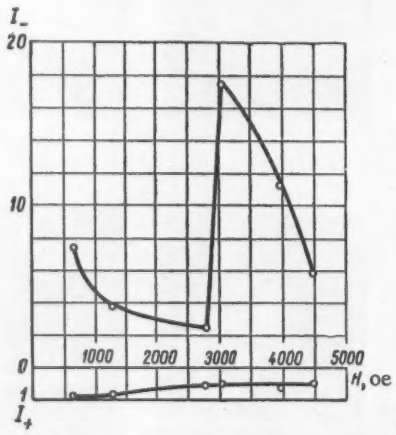

Fig. 6. Variation of electron current I_- and ion current I_+ in the probe with magnetic-field intensity. D_S = 3 mm; I_p = 0.6 amp; V_p = 210 v; p = $7 \cdot 10^{-5}$ mm Hg.

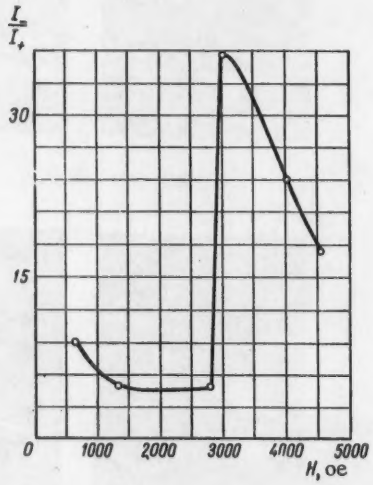

Fig. 7. Variation of ratio I_-/I_+ with magnetic-field intensity (from data of Fig. 6).

The behavior of the electron current I_- and the ion current I_+ in the probe with changes in the magnetic field is more clearly illustrated by Fig. 4, obtained on the basis of oscillograms Nos. 1-8. Of greatest interest is the intermittent increase in the electron current at a magnetic-field intensity of ~ 3050 oe, while at the instant of the jump, the ion current essentially does not change.

Figure 5 shows the variation of the ratio I_-/I_+ with the magnetic field intensity. At first, this ratio falls from 11 at 450 oe to 4 at 2500 oe. In the interval of 3000-3050 oe it rises from 5 to 17, if the electron current is measured on the lower curve of oscillogram No. 7 (without the capacitance); if the same electron current is measured at the averaged oscillogram No. 8 (with the capacitance), then the ratio I_-/I_+ in a field of 3050 oe intensity attains $\sim 10^2$.

Figures 6 and 7 show a similar variation (currents are given in arbitrary units) for the same probe, but at a discharge current of 0.6 amp, discharge voltage of 210 v, and the same pressure ($p = 7 \cdot 10^{-5}$ mm Hg). In this case the magnetic field was varied over a wider range and it is seen that the intermittent increase in the electron current follows the decrease in the field more or less smoothly.

If the pressure is decreased by half ($3.5 \cdot 10^{-5}$ mm Hg) the general character of the probe characteristics remains approximately the same. However, the jump in the electron current accompanying the appearance of the strong oscillations takes place at a magnetic field intensity of ~ 1500 oe, and not at ~ 3000 oe, as is the case at a pressure of $7 \cdot 10^{-5}$ mm Hg.

Discussion of the Results

The basic experimental results of the present work is the discovery that at some critical magnetic field there is an intermittent increase in the electron current of the probe, this being accompanied by the appearance of strong oscillations. The magnitude of the critical value of the magnetic field increases proportionally to the gas pressure, which evidently indicates the important role of the quantities $\omega_+ \tau_+$ or $\omega_- \tau_-$ characterizing the magnetization of the plasma, and, possibly, predetermining the occurrence of a new state of discharge with strong oscillations and a large transverse velocity of the electrons.

A strict quantitative analysis of the results which have been obtained is made difficult for a number of reasons. Firstly, the design of the probe used in this work cannot be regarded as satisfactory, since the edges of the probe opening in the anode are enveloped by a layer in which there is a negative potential drop at the anode, and, as a result, an indefinite collecting surface is formed for both electrons and ions. Secondly, the theory developed by Bohm [1] for the collecting of electrons by the probe in a discharge in a strong magnetic field is valid for sufficiently long discharges satisfying the condition

$$L > \frac{a}{\sqrt{\frac{D_-^p}{D_-}}}$$

(L is the discharge length, a is the radius of the probe, D_-^p is the coefficient of transverse electron diffusion in the magnetic field, D_- is the coefficient of electron diffusion without the magnetic field). In the present work, unfortunately, the opposite conditions were fulfilled. Finally, in Bohm's theory it is assumed for the kinetic energy of the ions in the plasma that $eT_+ \ll eT_-$ (T_- is the electron temperature), and therefore saturation of the electron current should have been observed at probe potentials that were positive with respect to the plasma by a value of $\sim T_+$. As may be seen from the oscillograms of Fig. 3, under the conditions of this experiment, saturation of the electron current is not observed, which evidently is a consequence of the relatively high ion energy [2].

If we ignore all these reservations and nevertheless use for estimating the ratio I_-/I_+ the formula of Bohm

$$\frac{I_-}{I_+} = \frac{8a\sqrt{D_- D_-^p}\left(1+\frac{T_+}{T_-}\right)}{0{,}4 \cdot 2\pi a^2 \sqrt{\frac{2eT_-}{M_+}}},$$

then, after substituting the values a = 0.15 cm, $\sqrt{M_+} \simeq 4$, $T_- = 1$ ev, $1 + (T_+/T_-) \simeq 1$, we obtain for H = 3000 oe the value $I_-/I_+ \simeq 3.5$, which is close to the measured ratio ~ 4. It should be noted that the experimental value of I_-/I_+ cannot be determined accurately also because of the absence of electron current saturation.

Without attaching too much importance to this estimation, but keeping in mind the fact that there is no doubt that there is an intermittent increase in the electron current, one may consider that the results obtained here, along with the results of [3], confirm the existence, to some degree of two qualitatively different mechanisms for the transverse movement of the electrons. The first mechanism, acting in the region below the critical value of the magnetic field, is evidently ordinary diffusion resulting from collisions. The second mechanism is, as before, unclear, but it may be hoped that more detailed and careful investigation of the observed critical transition in the discharge state will permit an explanation of its fundamental properties.

In conclusion, I wish to thank P. M. Morozov for his assistance and interest in this work, and also S. Sinotov, for taking part in the measurements.

LITERATURE CITED

1. A. Guthrie and R. Wakerling, The Characteristics of Electrical Discharges in Magnetic Fields (McGraw-Hill, New York, 1949).

2. A. Zharinov, Zhur. Tekh. Fiz. 27, 1803 (1957).
3. B. Lehnert, "Diffusion processes in the positive column in a longitudinal magnetic field," Report No. 146, presented by Sweden at the Second International Conference on the Peaceful Uses of Atomic Energy (Geneva, 1958).

ON THE DIFFUSION OF ELECTRONS IN A MAGNETIC FIELD

A. V. Zharinov

Translated from Atomanay Énergiya, Vol. 7, No. 3, pp. 220-224
September, 1959
Original article submitted February 13, 1959

The experimental data concerning the anomalously large mobility of electrons across a magnetic field is discussed. It is shown that the distribution of the concentration of the secondary plasma of a discharge with an incandescent cathode is practically independent of the electron transverse diffusion coefficient, and therefore cannot be used to explain the mechanism of diffusion. An estimation is made of the electron diffusion coefficient from the value of the electron current density at the anode, which confirms the presence of an anomalously large transverse mobility.

As a result of the study of experimental data on a discharge with an incandescent cathode in a strong longitudinal magnetic field, D. Bohm [1] suggested the hypothesis that under the conditions of such a discharge, a new, uninvestigated mechanism for the transverse movement of the electrons is considerably more effective than the diffusion by collision.

In particular, one of the arguments in favor of the anomalously large transverse mobility of electrons is the result of the analysis of probe characteristics. Assuming that the diffusion of electrons takes place by collision, Bohm obtained for the ratio of the electron to ion current in the probe I_-/I_+ the value 4-5, while the I_-/I_+ ratio measured under the corresponding conditions attained 20-35. Although Bohm's calculations do not lay claim to great accuracy, nevertheless, it is not very likely that they can give a reduced value of I_-/I_+, and therefore, they should not be considered.

Another experimental fact which Bohm used as evidence of the anomalously large transverse mobility of electrons is that the decrease in the concentration of the plasma with the distance from the beam of primary electrons takes place more slowly than expected. An approximate theoretical analysis of the distribution of the secondary plasma concentration (outside the primary electron beam) has been carried out in the two-dimensional case. Using conditions of quasi-neutrality treating the transverse motion of electrons and ions as a diffusion process, and neglecting the ionization in the secondary plasma, Bohm obtained the following expression for the characteristic length x_0 on which the concentration decreases e times as one moves away from the primary beam

$$x_0 = \sqrt{\frac{(T_+ + T_-)\,L}{\frac{\beta T_+}{D_+^p} + \frac{\gamma T_-}{D_-^p}}}, \qquad (1)$$

where T_+ and T_- are the temperatures of the ions and electrons in units of potential; D_+^p and D_-^p are the ion and electron transverse diffusion coefficients. The coefficients β and γ relate the ion current density at the anode j_+^a and the electron current density at the anode j_-^a to the plasma concentration n:

$$\left.\begin{aligned} j_+^a &= \beta n; \\ j_-^a &= \gamma n. \end{aligned}\right\} \qquad (2)$$

Assuming further that

$$\frac{\gamma T_-}{D_-^p} \gg \frac{\beta T_+}{D_+^p}, \qquad (3)$$

Bohm obtained, in place of (1), the expression

$$x_0 \approx \sqrt{\left(1 + \frac{T_+}{T_-}\right)\frac{D_-^p L}{\gamma}} \qquad (4)$$

Therefore, according to (4), the measurement of x_0 allows one to estimate the electron transverse mobility coefficient. Comparing the measured value of x_0 with the value calculated from (4) and assuming that ordinary diffusion takes place, Bohm discovered a lack of agreement between theory and experiment. It turned out that the electron diffusion coefficient calculated from (4) exceeds the collision diffusion coefficient by two orders of magnitude.

In his work A. Simon [2, 3] obtained an expression for x_0 substantially different from (4)

$$x_0 \approx \frac{L}{\pi}\sqrt{\frac{D_+^p}{D_{\text{AM}}}}, \qquad (5)$$

where D_{am} is the longitudinal ambipolar diffusion coefficient.

Comparing the measured value of x_0 to that calculated from (5), Simon found satisfactory agreement. It turned out, also, that as the magnetic field intensity increased, x_0 decreased proportionally to 1/H. On this basis, Simon believed that in the experiments he was considering, the diffusion of both the ions and the electrons took place in accordance with the well-known ideas, and that it was not necessary to assume the existence of an anomalously large electron transverse mobility as Bohm had done.

Simon, however, ignored the results of the above-mentioned probe measurements. Moreover, one can hardly, in general, determine the electron diffusion coefficient on the basis of a measurement of the characteristic length x_0 under conditions of a discharge of the type which Simon and Bohm had in mind.

The purpose of the present article is to show that under certain conditions the distribution of the secondary plasma concentration does not depend on the value of the electron diffusion coefficient, but is determined mainly by the picture of the ion motion. Owing to this, it may be supposed that Bohm and Simon were in error when they took the data on the plasma concentration distribution to explain the mechanism of the transverse diffusion of electrons.

ON THE DISTRIBUTION OF THE PLASMA CONCENTRATION IN A DISCHARGE WITH AN INCANDESCENT CATHODE IN A LONGITUDINAL MAGNETIC FIELD

Bohm's formula (4) corresponds the ambipolar diffusion of the plasma, to which, apparently, Simon first drew attention. It is interesting to note that Bohm did not use as his initial assumption the condition of ambipolarity of the diffusion, but condition (3) which he took as equivalent to such an assumption.

It may be stated, however, that in the conditions of the discharge being considered (Fig. 1), the diffusion

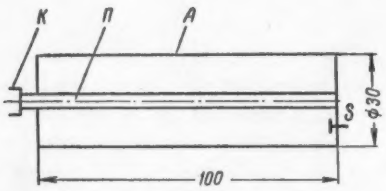

Fig. 1. Diagram of discharge chamber. K) cathode; A) anode; P) primary beam; S) probe.

cannot be ambipolar. Consequently, if there is ambipolar transverse diffusion outside the primary beam, then everywhere outside the primary beam P the resulting longitudinal current on the anode should be equal to zero, i.e, the equation

$$\varphi = T_- \ln \frac{v_-}{v_+} \qquad (6)$$

should hold, where φ is the potential of the plasma with respect to the anode; v_- and v_+ are the mean longitudinal velocities of the electrons and ions [(6) is a consequence of the equality of the currents at the anode; $j_+^a = j_-^a$]. At the same time, for the transverse diffusion to be ambipolar, the potential φ, as one moves away from the primary beam, should increase to a value of the order of T_+, which is incompatible with (6) for an equipotential anode, since the temperature of the electrons T_- in a strong magnetic field should decrease comparatively rapidly outside the primary beam, owing to the cooling of the electron gas.

For experimental evidence of the assumption one may use the results of the measurement of the currents going to the anode in the secondary plasma as obtained by the author and shown in Figs. 2 and 3. These figures show the current distribution on the anode surface, measured by means of a probe in the shape of a disk 1 mm in diameter, which was placed in the plane of the anode and moved perpendicularly to the magnetic field. The primary current had a diameter of 5 mm.

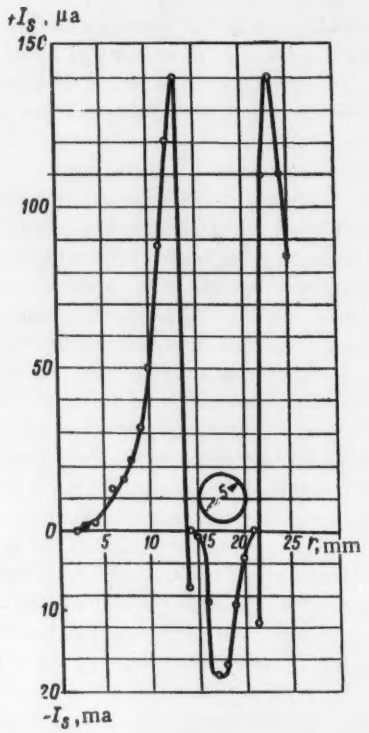

Fig. 2. Current distribution in the cross section of the discharge (I_p = 200 ma; V_p = 80 v; H = 2300 oe; p= $2 \cdot 10^{-3}$ mm Hg).

The series of curves presented corresponds to a discharge voltage V_p = 80 v, a discharge current I_p = 200 ma, a magnetic field intensity H = 2300 oe, and argon pressure inside the discharge chamber $p = 2 \cdot 10^{-3}$ mm Hg. The length of the discharge gap L was 10 cm, the diameter of the discharge tube was 30 mm.

In Fig. 2 the distance from the probe to the wall of the discharge chamber is laid off along the abscissa axis, the ion current in microamperes is laid off along the upper part of the ordinate axis, while the electron current in milliamperes is laid off along the lower part of the ordinate axis. The region occupied by the primary beam is marked by a circle. The probe was at the potential of the anode. It is seen from the figure that at a distance ~ 1 mm from the edge of the primary beam the ion current predominates. Moreover, as may be seen from the voltage vs current characteristics (taken in this experiment and shown in Fig. 3), the ion current on the probe is essentially greater than the electron current, beginning with a distance of ~ 1 mm from the edge of the primary beam. At greater distances (Fig. 3b) there is, in effect, a saturated ion current on the probe. For example, at the point r = 9 mm, back from the center of the primary beam by ~ 8-9 mm the electron current constitutes about 6% of the ion current.

Clearly, these facts convincingly indicate that the diffusion in the secondary plasma is not ambipolar and that the electrons move across the field considerably more slowly than the ions.

On the basis of these data one may consider that the electrons in the secondary plasma are, as it were, in a closed potential box, and to a first approximation, their escape from it may be neglected, i.e., it may be assumed that the electron gas is in a Boltzmann equilibrium, and therefore the electron stream in the secondary plasma is practically absent. Then, as may readily be shown, the characteristic length x_0 will be given by the formula

$$x_0 = \frac{L}{\pi} \sqrt{\frac{\overline{D_+^p}}{\overline{D_+}}}. \qquad (7)$$

According to this formula, the distribution of the concentration of the secondary plasma does not depend on the coefficient of electron diffusion, and the physi-

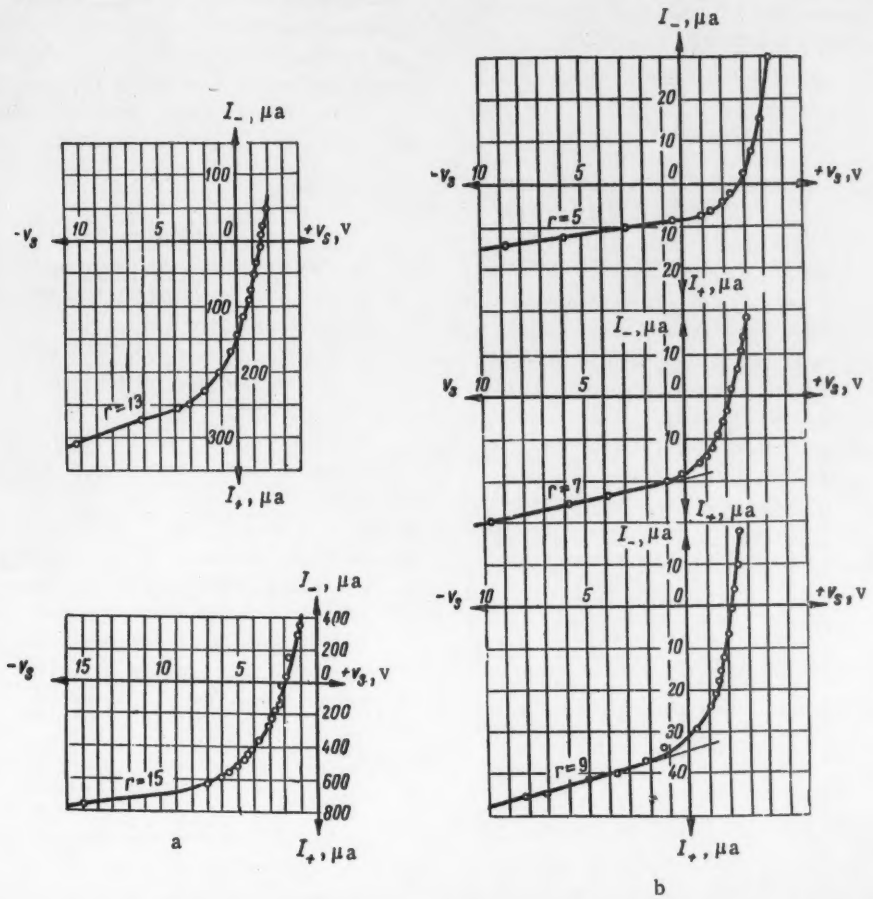

Fig. 3. Ion part of the probe characteristics taken at different points of the cross section of the discharge. a) close to the primary beam; b) at the periphery.

cal meaning of it is understandable, if one considers that, in the case of ion diffusion, the ratio of the mean square displacements across and along the magnetic field is given by

$$\frac{\overline{x_0^2}}{\left(\frac{L}{2}\right)^2} \approx \frac{D_+^p}{D_+} .$$

One may also obtain (7) within the framework of Bohm's theory if in accordance with the smallness of the electron current on the anode, even in comparison with the ion current, one assumes that the condition opposite to conditon (3)

$$\frac{\gamma T_-}{D_-^p} \ll \frac{\beta T_+}{D_+^p} \qquad (8)$$

is fulfilled.

Taking into account (8) we obtain, instead of (4),

$$x_0 = \sqrt{\left(1+\frac{T_-}{T_+}\right)\frac{D_+^p L}{\beta}} . \qquad (9)$$

In the case of longitudinal diffusion of ions the order of magnitude of the coefficient β is

$$\beta \simeq \frac{D_+}{L}\left(1+\frac{T_-}{T_+}\right) . \qquad (10)$$

It is not difficult to see that when (10) is substituted into (9), one actually obtains (7). It should be noted that Simon's formula (5) gives practically the same quantitative results as (7), but, as it seems to us, it has a less clear physical meaning and was obtained by neglecting, in the balance of streams of charged particles, terms proportional to the transverse mobility of the ions and electrons. The correctness of neglecting these terms is not quite evident.

Under conditions in which the distribution of the space charge is practically independent of the coefficient of electron diffusion, an attempt may be made to estimate directly the value of the electron current at the anode at some point r. Its order of magnitude will be

$$j_-^a \propto \frac{LD_-^p n}{r^2} . \qquad (11)$$

The ratio of the electron current to the ion current is

$$\frac{j_-^a}{j_+^a} \simeq \frac{LD_-^p}{r^2 v_+} . \qquad (12)$$

The lower probe characteristic of Fig. 3 b (r = 9 mm) was obtained at a plasma concentration of $\sim 10^{11}$ cm^{-3} and a neutral gas concentration of $\sim 7 \cdot 10^{13}$ cm^{-3}. At such a ratio of the concentrations and at $T_- \simeq$ ev, the collisions between the electrons and the ions do not have to be taken into account. Then, in a magnetic field H = 2300 oe, the electron diffusion coefficient is $D_-^p \simeq 10$ cm^2/ sec. Taking into account the fact that the argon ions move freely [4] and have a longitudinal energy $\sim T_- = 1$ ev, we obtain $v_+ \simeq 2 \cdot 10^5$ cm/sec. Inserting these data into (12) and setting L = 10 cm and r = 1 cm, we obtain

$$\frac{j_-^a}{j_+^a} \simeq 5 \cdot 10^{-4} .$$

The measured ratio of currents at the anode, as has been indicated previously, is $6 \cdot 10^{-2}$. Although this estimation is very coarse, the observed discrepancy (by two orders of magnitude) is clearly not in favor of diffusion by collision.

A more convincing proof of the existence of some mechanism of the transverse movement of electrons other than the ordinary diffusion is the intermittent increase in the ratio of the electron current on the probe to the ion current [5], and also the sharp increase in the coefficient of transverse diffusion [6].

In conclusion I wish to thank I. V. Kurchatov for his interest in this work and his constructive criticism.

LITERATURE CITED

1. A. Guthrie and R. Wakerling, The Characteristics of Electrical Discharges in Magnetic Fields (McGraw-Hill, New York, 1949).
2. A. Simon, Phys. Rev. 98, 317 (1955).
3. A. Simon, "Diffusion of arc plasmas across a magnetic field," Report No. 366, presented by the USA at the Second International Conference on the Peaceful Uses of Atomic Energy (Geneva, 1958).
4. A. V. Zharinov, Zhur. Tekh. Fiz. 27, 1803 (1957).
5. A. V. Zharinov, Atomnaya Énergiya 7, 215 (1959).*
6. B. Lehnert, "Diffusion processes in the positive column in a longitudinal magnetic field," Report No. 146, presented by Sweden at the Second International Conference on the Peaceful Uses of Atomic Energy (Geneva, 1958).

*Original Russian pagination. See C. B. translation.

INVESTIGATION OF THE ENERGY CHARACTERISTICS OF THE EXTERNAL PROTON BEAM IN THE SIX-METER SYNCHROCYCLOTRON

I. M. Vasilevskii and Yu. D. Prokoshkin

Translated from Atomnaya Énergiya, Vol. 7, No. 3, pp. 225-230
September, 1959
Original article submitted December 7, 1958

The energy spectrum and the average energy of the external proton beam of the six-meter synchrocyclotron of the Joint Institute for Nuclear Studies have been investigated under various operating conditions. The spectrum is described by a Gaussian curve with a dispersion of (2.8±0.3) Mev. The mean energy has been determined to within an accuracy of 0.1%.

Introduction

The increase in the beam intensity of the proton beam extracted from the synchrocyclotron chamber at the Joint Institute for Nuclear Studies [1] has made it possible to carry out a number of experiments in which particle interaction cross sections can be measured with an accuracy of several percent. However, the realization of this kind of accuracy is possible only if one can measure cross sections and energy of the proton beam at the same time. This situation is a result of the rapid increase in these cross sections as the energy is increased, especially in regions close to the threshold of the reactions being investigated. For example, the cross section for the formation of mesons in nucleon collisions at proton energies of 650 Mev varies at the rate of 0.7%/Mev, at 350 Mev this quantity varies at the rate of 3%/Mev. In view of this rapid increase in cross section at low proton energies one must know not only the mean energy but also the energy spectrum of the beam. It is especially desirable to know the latter in cases in which the energy of the proton beam is reduced by an absorber, a process which results in a considerable increase in the energy spread of the beam.

In the present work we have investigated the energy spectrum of the proton beam at several values of the proton energy in the range 150-670 Mev. In addition, we have measured the mean energy of the protons for various operating conditions of the machine.

Proton Energy Spectrum

In measuring the proton spectrum use is made of a magnet with pole pieces 100 cm in diameter which provides a field of 16 koe in the gap. The magnet is located in the path of the external proton beam (Fig. 1) and can deflect the latter through angles up to 20°. In front of the magnet there are several brass collimators which are essentially vertical slits; these collimators define a plane proton beam 0.1-0.7 cm in width and 2 cm in height. At the output of the

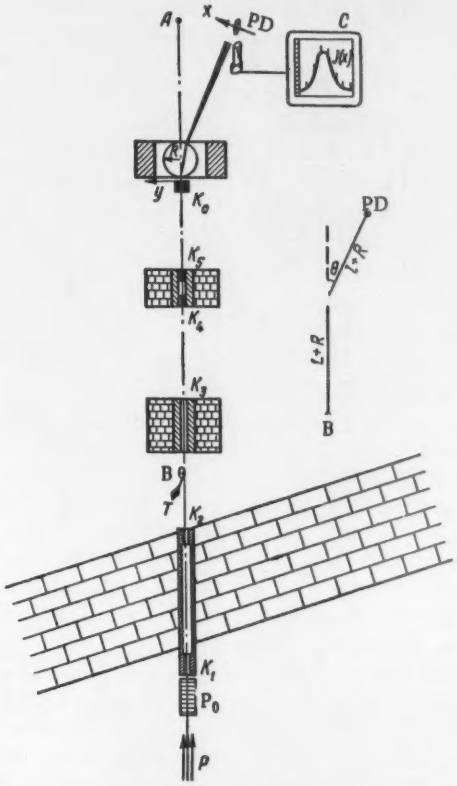

Fig. 1. Diagram of the experiment: P) proton beam; P_0) polyethylene absorber; K_0-K_5) collimators; PD) proton detector; C) automatic recording potentiometer; B) unit for stretching wire.

spectrometer the protons are recorded by a detector which consists of a thin (0.1-0.2 cm) plastic scintillator and an FÉU-19M photomultiplier which is located behind it. The pulses from the multiplier are integrated by an RC network and the current ($10^{-9} - 10^{-7}$ amp) is measured by an automatic recording potentiometer (EPPV-51). By means of a synchronous motor the detector can be moved perpendicularly to the proton beam. Under these conditions the strip of the recording potentiometer registers the change in current density J with variation of the x coordinate (Fig. 1). The recording potentiometer also records coordinate markers so that the value of x can be determined with an accuracy of 0.02 cm. A typical J (x) curve is shown in Fig. 2. Only one detector such as that described above is used in the apparatus; this detector records the variation in the intensity of the proton beam with time. The time required for the measurement of a J (x) curve is 5 min. In the course of this time period the change in the magnetic field produced by the deflection magnet is kept to less than 0.05%.

As is apparent from Fig. 2, the function J (x) is described by a Gaussian curve. The dispersion of this curve σ is determined by several factors (each of which is characterized by a particular component of the dispersion σ_i): the energy spread in the beam σ_E, scattering of protons from the beam in air σ_s, the widths of the collimator and the scintillator σ_x, etc. The magnitudes of these dispersion factors vary in different ways as the distance l is increased (cf. Fig. 1) so that the ratio σ_E/σ passes through a broad maximum in the region $3 < l/R < 10$. The quantity l/R has been made equal to eight, providing a spectrometer resolution of $dE/Edx \approx 1\%$ cm. In this case the ratio σ_E/σ_s is 0.5. The quantity σ_s is reduced by placing in the path of the beam a thin-walled polyethylene tube filled with helium which makes it possible to reduce the scattering by a large factor.

The proton energy spectrum is found by comparing the J (x) curves measured with the magnetic field switched on [$J_H(x)$] and with the field switched off [$J_0(x)$]. In order to measure the $J_0(x)$ curve the detector is placed in the path of the undeflected beam at point A (cf. Fig. 1). Under these conditions the square of the dispersion σ_E^2 is determined by the difference $\sigma_H^2 - (k\sigma_0)^2$, where σ_H and σ_0 are the dispersion in the functions $J_H(x)$ and $J_0(x)$, respectively; the factor k characterizes the focusing effect of the magnetic field and is given approximately by $1 - \theta^2/2$ (θ is the angle through which the beam is deflected in the spectrometer). For the values of the angle chosen $\theta \simeq 16°$ this factor is close to unity: k = 0.96. In experiments carried out without helium the ratio σ_E/σ_0 is 0.5. The mean energy spread of the beam in this case is determined with an accuracy of approximately 0.6 Mev but the relative shape of the energy spectrum cannot be ascertained. The use of helium makes it possible to increase the ratio σ_E/σ_0 by a factor of 2.5 so that it then becomes possible to determine both the dispersion σ_E, and the shape of the spectrum fairly accurately. The function F (x) which describes the spectrum can be found by solving the integral equation.

$$J_H(x) = \int_0^\infty J_0(k[x-\xi])\,F(\xi)\,d\xi. \qquad (1)$$

The energy spectrum of the extracted proton beam is found to be symmetric. It is described by a Gaussian curve:

$$\Phi(E) \simeq \exp\{-(E-\overline{E})^2/2\Delta_E^2\}. \qquad (2)$$

At a proton energy $\overline{E}$ = 665 Mev the magnitude of Δ_E is found to be 3.0 ± 0.6 Mev (measured without helium) and 2.7 ± 0.3 Mev (measured with helium). The mean weighted value is

$$\Delta_E = (2{,}8 \pm 0{,}3) \text{ Mev.}$$

The spectrometer is calibrated (i.e., the quantities $\overline{E}$ and $d\overline{E}/dx$ are determined) by means of current-carrying wires (cf. below).

The dispersion found in the present work Δ_E differs from the estimate $\Delta_E \simeq 4$ Mev given in [2] based on an ionization-chamber method [3]. The reason for this discrepancy lies in the fact that Δ_E quoted in [3] is too high since the authors have not taken account of proton scattering.

The method described here has been used to measure proton spectra at lower energies in which case the beam is stopped by passage through a polyethylene absorber (cf. Fig. 1). As the proton energy is reduced the energy spread of the beam increases because of the increased ionization losses and "straggling," due to fluctuations in the ionization losses. Hence the relative dispersion Δ_E/E increases rapidly as the protons are

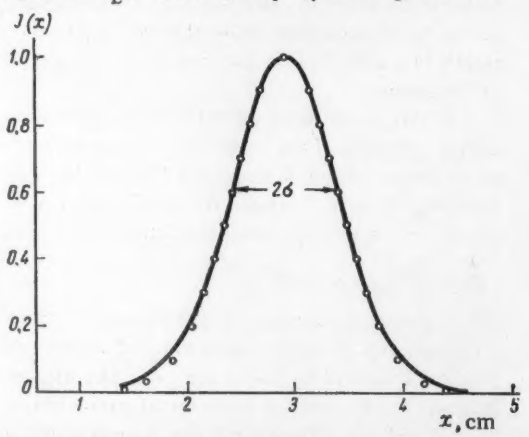

Fig. 2. The measured function J (x). The circles indicate values for a Gaussian function with standard deviation σ.

slowed down and this facilitates the measurement procedure considerably. For example, at $\bar{E}$ = 185 Mev helium need not be used and wide collimators (0.7 cm) can be substituted since even under these conditions $\sigma_E/\sigma_0 = 2.5$. The functions $J_H(x)$ and $J_0(x)$, measured at low proton energies are found to be described by Gaussian curves. It follows that at low proton energies the proton spectrum $\Phi(E)$ is also given by an expression of the Guassian form as in (2).

The measured dispersion Δ_E is shown in Fig. 3. The results of the experiment are in agreement with the theoretical dependence plotted taking account of the increase in ionization losses and straggling [4].

Mean Proton Energy

The most widely used technique for determining the mean energy of an external beam is the measurement of proton range by means of an ionization chamber [3]. However, as noted [3] this method always leads to a systematic uncertainty (2-3 Mev and E ≃ 650 Mev) because of the fact that the proton scattering is not considered in the analysis of the Bragg curve. A proper calculation, which takes scattering into account, avoids this error; however, in this case, the ionization chamber technique does not provide an accuracy much better than 5 Mev at E ≃ 650 Mev, because the ionization potential which appears in the range-energy relation is not known with the required accuracy.

By measuring the emission angle of the Cerenkov radiation [2, 3] it is possible to determine the proton velocity directly. This method is most exact at low proton energies; as the proton energy increases the accuracy decreases (at E≃650 Mev the accuracy is 2 Mev). The optical system which is used to measure the Cerenkov angle is complicated and this requirement tends to limit the possibilities of practical application of this technique.

In order to measure the mean proton energy with an accuracy better than 1 Mev we have used the current-carrying wire technique [5] (a diagram of the measurement system is shown in Fig. 1). A thin flexible wire filament is fastened at one end at the center of the detector (in front of the scintillator) and passes through the magnet and collimators, reproducing the path of the proton beam. At point B there is a device by means of which the wire is stretched by a weight T. A current i is passed through the wire. If T, i, and the mean momentum of protons in the beam P satisfy the relation

$$P = cgT/i, \qquad (3)$$

where c is the velocity of light and g is the acceleration of gravity, * the projections of the wire and the beam on the horizontal plane coincide. If the detector is located in such a way that the scintillator is placed at the maximum of the J(x) curve, and the wire passes through the center of the collimator slit of collimator K_0, and the current i is measured at this position of the wire, we can find P.

Equation (3) applies if the wire is absolutely flexible and weightless. The elastic properties of the wire, however, give rise to a moment which opposes the electromagnetic forces. As a consequence, the value of the momentum computed from (3) differs (for a copper wire) from the true value by an amount $5 \cdot 10^3 Pd^4/T$ (d is the diameter of the wire in centimeters). In addition to this correction it is necessary to take account of the sagging of the wire due to its own weight, which is given by the quantity $d^2 l_0^2/T$ (l_0 is the length of the wire). The wire actually passes below the beam trajectory and this effect is important if the magnetic field is not uniform. The appropriate correction can be determined experimentally by moving the wire in the vertical direction. In the present case this correction is less than 0.05%. From the correction for the sagging of the wire under the effect of its own weight it follows that the length of the wire l_0 must be made as small as possible. However, a reduction in the length of the wire leads to a reduction in the accuracy of the measurement since

$$\Delta y/\Delta P \approx L(l_0 - L - R)\sin\theta/Pl_0 \qquad (4)$$

(cf. Fig. 1). The minimum length l_0 is determined by the accuracy Δy_{min}, with which the wire can be located at the center of the slit of collimator K_0. In the present case L = 9 m, l_0 = 16 m, and Δy_{min} = = 0.03 cm. The wire is located at the center of the slit automatically by means of a contact device. The error $\Delta P/\Delta P$, given by (4) is 0.03%. As the diameter of the wire is reduced the size of the corrections are

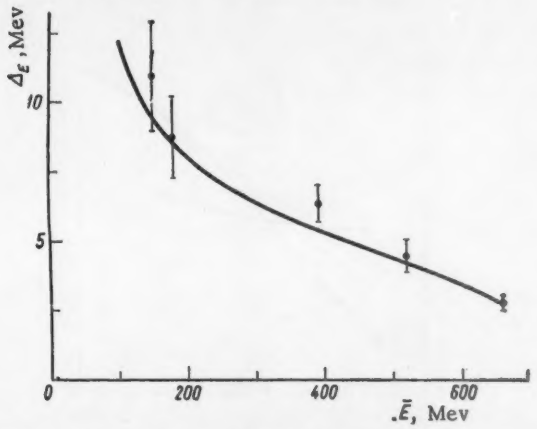

Fig. 3. The beam dispersion Δ_E at various proton energies E. The curve shows the theoretical dependence of dispersion on energy.

* The value of cg at the latitude of Dubna is 2.9426 if T is measured in g, i in amp, and P in Mev/c.

also rapidly reduced. Thus, with measurements with T = 100 g and d = 0.01 cm the correction for the elasticity of the wire is 0.4% (for P = 1300 Mev/c), while with d = 0.013 cm the correction is 1%. This correction is reduced by a factor of 2 or 3 if the wire is heated before the measurement by passing a high current through it.

In the present work the measurements are carried out with d = 0.01 cm, T = 100 g. The current $\underline{i}$ varies from 0.2 to 1.0 amp. The quantities T and i are measured with an accuracy better than 0.05% so that it is possible to determine the mean beam energy $\overline{E}$ with an error smaller than 1 Mev:

$$\overline{E} = (667.1 \pm 0.7) \text{ Mev}$$

(at the output of the accelerator chamber). The mass of the proton is taken as 938.21 Mev.

The accuracy indicated above can be realized in a limited range of proton energy (E > 250 Mev). At smaller energies it is necessary to use a small weight, a high current, and a thick wire; all of these factors reduce the accuracy of the measurements.

Beam Energy for Various Proton Acceleration Conditions

The mean energy of the beam depends on the strength of the magnetic field in the accelerator, the nature of the radial oscillations, and the conditions under which the beam is extracted; thus this energy depends on a large number of parameters which characterize the operation of the accelerator. For this reason the energy of the beam is not a fixed quantity, but varies over wide limits because of uncontrolled changes in the number of the accelerator parameters.

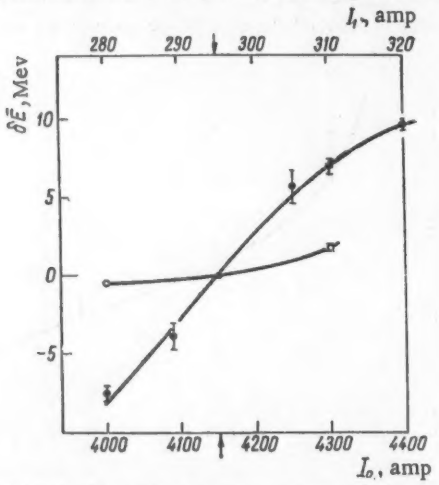

Fig. 4. Variation in mean energy of the proton beam with variation in the magnet current I_0 ($\overline{\bullet}$) and the current I_1 in the winding ($\overline{\circ}$), which corrects the position of the median plane of the magnetic field. The arrows indicate the values of I_0 and I_1 which obtain under ordinary operating conditions.

These variations in the magnitude of E amount to several million electron volts:

Date of the Measurements	$\overline{E}$, Mev
7/5/57	671.0±1.5
8/3/57	667.8±1.0
8/20/57	667.1±0.7
5/3/58	658.8±1.0
6/5/58	669.3±1.0
7/29/58	666.3±1.0
8/20/58	665.3±1.0
10/12/58	663.2±1.0

The value of $\overline{E}$ can be varied over certain limits by choosing an appropriate mode of operation. The necessity for control of the beam energy arises in a number of experiments in which one requires that the energy of the proton beam remain fixed. As has been shown by measurements, the energy $\overline{E}$ is sensitive to the strength of the magnetic field in the accelerator (Fig. 4). The control of $\overline{E}$ over a small range can be achieved also by varying the conditions of beam extraction (Fig. 5). By proper choice of these variables it is possible to increase the beam energy to the value

$$\overline{E}_{\max} = 683 \text{ Mev.}$$

Under these conditions the intensity of the extracted proton beam is reduced by three orders of magnitude. Variations in the mode of acceleration and conditions of extraction are accompanied by small changes in the dispersion Δ_E. Thus, when the current I_0 is increased from 4100 to 4250 amp the dispersion Δ_E is reduced by 0.5±0.3 Mev, while a change in the position (r) of the regenerator in the device by means of which the beam is extracted [1] causes the dispersion Δ_E to vary as follows:

for $r = 281.35$ cm $\Delta_E = 3.7 \pm 0{,}5$ Mev;
for $r = 280.35$ cm $\Delta_E = 2.8 \pm 0{,}3$ Mev;
for $r = 278.85$ cm $\Delta_E = 1.8 \pm 0{,}5$ Mev.

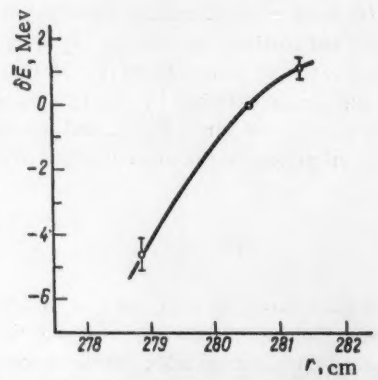

Fig. 5. Variation in the mean energy of the proton beam with variation of the position of the regenerator (r).

As we have indicated earlier, measurements of the beam energy are especially important if an absorber is used to reduce proton energy (this method is used in many experiments). It is necessary to determine the energy of the degraded beam (this is inconvenient since the thickness of the absorber usually varies several times in the course of the experiment) or to determine the energy of the undegraded beam; in the latter case the energy spread relation for the absorber is used to determine the energy of a stop beam. This relation has been measured by us for polyethylene $(CH_2)_n$ (it is also applicable for paraffin) in the range 150-665 Mev (Fig. 6). We may note that the usual range-energy relation can not be used for determining the energy of the protons instead of the indicated relation because it leads to large errors, especially for low energies of the degraded beam. Thus, if the range-energy relation is known with an accuracy of 2 Mev at $\bar{E}$ = 650 Mev (0.4%), when the beam energy is reduced to 100 Mev the uncertainty in the energy determination increases up to 6 Mev (6%), i.e., an increase of a factor of 15.

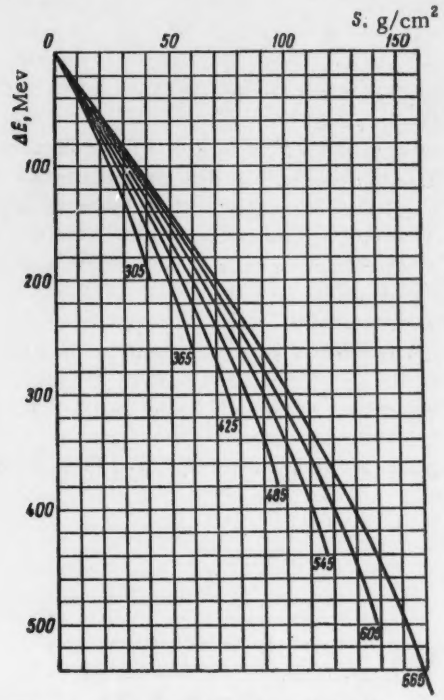

Fig. 6. Energy spread $\Delta_E = E - E'$ in a polyethylene absorber of thickness S. $\bar{E}$ and $\bar{E}'$ are the mean energies of the proton beam before and after the absorber. The numbers on the curves indicate the corresponding values of E.

In conclusion we wish to thank T'ang Hsiao-wei and A. A. Tyapkin for discussion of the results of the present work.

Note added in proof. The method described here has been used to measure the mean energy of the external beam in operation of the synchrocyclotron for accelerating heavy particles: deuterons and α-particles. It is found that for deuterons extracted from the acceleration chamber E = (405.3 ± 0.5) Mev while for α-particles E = (811.3 ± 1.0) Mev (for mass values of m_d = 1875.5 and m_α = 3727.2Mev, respectively). The energy spectra of the beams are characterized by the following dispersions: for deuterons Δ_E=(1.7 ±0.5) Mev and for α-particles Δ_E = (3.5 ± 1.5) Mev.

LITERATURE CITED

1. V. P. Dmitrievskii, V. I. Danilov, et al., Pribory i Tekh. Éksp. No. 1, 11 (1957).
2. V. P. Zrelov and G. D. Stoletov. Zhur. Éksp. i Teor. Fiz. 36, 658 (1959).
3. R. Mather, Phys. Rev. 84, 181 (1951); R. Mather and E. Segrè, Ibid, p. 191.
4. J. Lindhard and M. Sharff, Dan. Mat. Phys. Medd. 27, 15 (1953).
5. J. Thomson, Phil. Mag. 6, 561 (1907); M. S. Kozodaev and A. A. Tyapkin, Pribory i Tekh. Éksp. 1, 21 (1956).

PHASE DIAGRAM OF THE ZIRCONIUM-RHENIUM SYSTEM

E. M. Savitskii, M. A. Tylkina, and I. A. Tsyganova

Translated from Atomnaya Énergiya, Vol. 7, No. 3, pp. 231-235,
September, 1959
Original article submitted April 16, 1959

The phase diagram of the zirconium – rhenium system was constructed by x-ray and microscopic methods and by measurements of melting points, hardness and microhardness of the phases.

The region of solid solutions of rhenium in α-zirconium at 800° C is ~0.5 weight %, and at the temperature of the eutectoid transition it increases to 2-3 weight %. At 1600° C, 14.68 weight % of rhenium dissolves in β-zirconium and at the eutectoid transition point at 550-600° C, 8 weight % of rhenium. The β-phase is stabilized in alloys containing more than 4 weight % of rhenium. An eutectic is formed at 1600° C and 25 weight % of rhenium. The presence of a metastable ω-phase in melts rich in zirconium was established.

The solubility of zirconium in rhenium at 2500° C is less than 2 weight %.

Three chemical compounds are formed in the system by peritectic reactions:

1) At 2500° C, Zr_5Re_{24} of the α-Mn type with a body-centered cubic lattice (a = 9.6-9.7 kX) and a microhardness of 1000 kg/mm²;

2) at 2450° C, $ZrRe_2$ with a hexagonal, close-packed lattice (a = 5.21-5.25 A; c= 8.5-8.56 A; c/a = 1.63) and a microhardness of 1200 kg/mm²;

3) at 1900° C, Zr_2Re of the σ-phase type with a tetragonal lattice (a = 10.12 A; c = 5.42 A; c/a = 0.535) and a microhardness of 700-800 kg/mm².

Zirconium and rhenium are transition metals with an incomplete d-shell. The table gives some comparative data characterizing these metals. There is hardly any literature data on the zirconium-rhenium system. Only the chemical compound $ZrRe_2$ (Laves phase) is known and this has a lattice of the $MgZn_2$ type with the parameters a=5.251 kX, c=8.576 kX, c/a=1.633 [1]. In [2] the authors of this article confirmed that the compound $ZrRe_2$ is formed and established the formation of the compound Zr_2Re, melting at 1900° C.

As starting materials we used iodide zirconium and rhenium powder with 99.8 weight % purity, which were introduced into the charge in the form of briquets, first sintered at 1400° C in vacuum.

The melts (25 samples of 30 g each) were prepared by arc melting with unconsumed tungsten electrode on a water-cooled copper bottom in a helium atmosphere at 200 mm Hg. The melts were fused two to three times for a uniform distribution of the components. The compositions of the alloys, determined from the charge and by chemical analysis, differed insignificantly.

The microstructural analysis was carried out on sections, prepared in the usual way. An aqueous solution of hydrofluoric and nitric acids in various proportions, depending on the composition of the alloy, was used for etching. As the rhenium content of the alloy increased, the nitric acid content of the solution was increased. X-ray patterns of powders or cylindrical samples, 0.6-0.8 mm in diameter, were obtained in a Debye camera with unfiltered chromium radiation.* In addition, we measured the Vickers hardness of forged and heat treated alloys and the microhardness on a PMT-3 apparatus for various phase components.

The zirconium corner of the phase diagram was investigated on forged samples. The alloys were forged into bars with a 7 × 7 mm cross section at 800-1000° C. Phase analysis of these alloys was carried out with samples as cast and also tempered after forging. Isothermal annealing with quenching in water was done in evacuated quartz ampoules at 1050 and 950° C for 30 minutes, at 850, 800, and 700° C for 6 minutes, at 500° C for 860 hours, and at 400° C for 2 months.

The sections of the diagram from 45 to 100 weight % of rhenium were examined by means of cast samples as they shattered on forging. Phase analysis was carried out on cast alloys and alloys annealed to 1000° C for

* The x-ray investigations of the zirconium – rhenium system were carried out by P. I. Kripyakevich and E. I. Gladyshevskii at Leningrad State University.

Comparative Data for Zirconium and Rhenium

Characteristics	Zirconium	Rhenium
Atomic volume	14.2	8.9
Atomic radius, A:		
α-zirconium	1.59	1.37
β-zirconium	1.61	
Lattice parameters, A	α-hexagonal, close-packed (a = 3.223, c = 5.123, c/a = 1.59); β-cubic, body-centered (a = 3.12)	α-hexagonal, close-packed (a = 2.755, c = 4.449, c/a = 1.614)
Polymorphic transition point, °C	862° ± 5	—
Melting point, °C	1860	3160
Specific gravity, g/cm³	6.4	21.02
Difference between atomic radius and that of rhenium, %:		
α-zirconium	+16	—
β-zirconium	+17	

560 hr with subsequent quenching in water. The phase composition of cast alloys is arbitrarily plotted on the diagram on the isotherm at ~1500° C. It can be considered that the structure of cast alloys, rapidly cooled on the copper bottom of the arc furnace, corresponds approximately to alloys quenched from high temperature.

This solidus curve was determined in vacuum on samples 8 × 5 × 5 mm in an apparatus for measuring the melting point of refractory metals [2]. The melting point was determined with an optical pyrometer ("drop method") as the point when a hole drilled in the sample filled with metal. The pyrometer was calibrated with the aid of pure metals under the same conditions. The melting points were determined as the average of two to three measurements.

The phase diagram (Fig. 1) was constructed from the data of x-ray and metallographic analysis, melting point determinations, and hardness measurements.

The compounds Zr_2Re, $ZrRe_2$, and Zr_5Re_{24}, which were formed by peritectic reactions, were detected in the system. Zirconium gives limited α- and β-solid solutions with rhenium. A eutectic is formed between β-zirconium and Zr_2Re. Eutectoid decomposition of the β-solid solution occurs in the solid state with the formation of an α-solid solution and the compound Zr_2Re.

The region of solid solutions in β-zirconium extends to 15 weight % of rhenium at 1600° C, but is reduced to 8 weight % at the eutectoid transition point. The β-phase is stabilized with a rhenium content of more than 4 weight %. The polymorphic transition point of zirconium falls from 862 to 550 600° C with an increase in the rhenium content. Eutectoid decomposition of the β-solid solution occurs at 550° C by the reaction β-solid solution ⇌ α-solid solution + Zr_2Re.

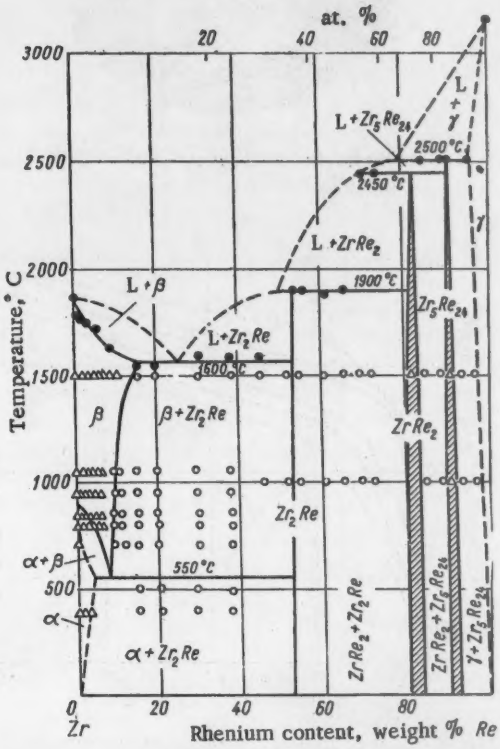

Fig. 1. Phase diagram of the zirconium – rhenium system: Δ) single-phase structure; O) two-phase structure; ●) solidus.

The solubility of rhenium in α-zirconium is low: 0.5 weight % at 700-800° C. The solubility increases somewhat with a fall in temperature and is less than 3 weight % at 400° C. At 1600° C and ~25 weight % of rhenium there is the eutectic transition liquid ⇌ β-solid solution + Zr_2Re.

After quenching from 850-700° C, the alloy with 0.79 weight % of rhenium (Fig. 2) has a two-phase structure (α + β).

X-ray investigation of zirconium-rich alloys, quenched from 1000° C, made it possible to detect the presence of a metastable ω-phase with a rhenium content of ~5.6 at. %. This phase has a complex, noncubic lattice. Analogous phases have been found in systems of titanium with a number of elements and are formed during the aging of titanium-rich alloys [3].

Fig. 2. Alloy with 0.79 weight % of rhenium, x 200.

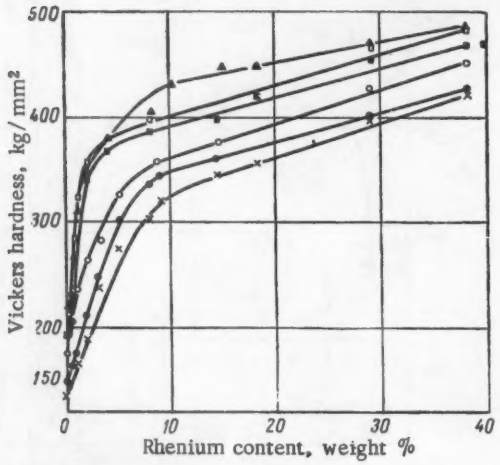

Fig. 3. Change in hardness of zirconium-rhenium alloys during heat-treatment; x) annealing at 500° C, 860 hr; ●) quenching from 700° C; O) quenching from 800° C; ■) quenching from 850° C; Δ) quenching from 950° C; ▲) quenching from 1050° C.

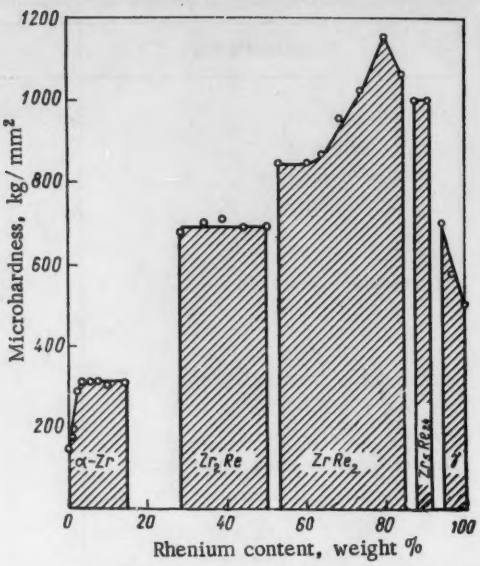

Fig. 4. Microhardness of phases in the zirconium-rhenium system.

Fig. 5. Alloy with 98 weight % of rhenium, x 340.

Alloying of zirconium with rhenium leads to a considerable increase in hardness (Fig. 3). Thus, for samples annealed at 500° C for 860 hr, the hardness of pure zirconium (136 kg/mm²) increased to 350 kg/mm² for an alloy with 14.68 weight % of rhenium and to 420 kg/mm² for an alloy with 38.4 weight % of rhenium. A similar change in hardness occurred with various quenching conditions, when the numerical values of the hardness increased correspondingly with a rise in quenching temperature. In addition, the microhardness of separate phases was determined (Fig. 4).

The solubility of zirconium in rhenium at the melting point was less than 2 weight %. An alloy with 98 weight % of rhenium already had two phases (Fig. 5). and consisted of a γ-solid solution of zirconium in

rhenium + Zr_5Re_{24}. A hypothetical line for the solubility of zirconium is plotted on the diagram.

The compound Zr_5Re_{24} with a rhenium content of 90-92 weight % is formed by the peritectic reaction: liquid + γ-solid solution of Zr in Re $\rightleftharpoons$ Zr_5Re_{24} at 2500° C and crystallizes in the form of dendrites with somewhat expanded faces. The lines of this phase on x-ray patterns indicated a cubic lattice (a=9.60 – –9.70 kX) [4].

The lattice constant of the Zr_5Re_{24} is close to the constant of χ-phases, i.e., compounds of the α-Mn type or a superlattice related to it of the Ti_5Re_{24} type, observed in systems of transition metals with rhenium (for example, for $Nb_{37}Re_{63}$ a= 9.67 kX [5], and for Ti_5Re_{24} a = 9.59 kX [6, 7]).

Accurate determination of the lattice constant of the compound showed that for the alloy with 80.6 at.% of rhenium a = 9.693 kX and for the alloy with 82 at.% of rhenium a = 9.626 kX. Consequently the compound has a variable composition.

Fig. 6. Alloy with 83 weight % of rhenium, x 200.

The microhardness of the Zr_5Re_{24} phase was ~1000 kg/mm^2. More detailed data on this compound was published in [4]. The compound $ZrRe_2$ (80 weight % of rhenium) is formed at 2450° C by the peritectic reaction: liquid + Zr_5Re_{24} $\rightleftharpoons$ $ZrRe_2$. The microhardness of the compound was 1200 kg/mm^2.

Between the compounds ZrRe and Zr_5Re_{24} lies a two-phase region (Fig. 6).

Fig. 7. Alloy with 55 weight % of rhenium, x 200.

The compound Zr_2Re, analogous to σ-phases, is formed with a rhenium content of 50 weight % at 1900° C by the peritectic reaction: liquid + $ZrRe_2$ $\rightleftharpoons$ $\rightleftharpoons$ Zr_2Re. The lattice is tetragonal with the parameters: a = 10.12 A; c = 5.42 A; c/a = 0.535. The microhardness is 700-800 kg/mm^2 and the region of homogeneity of the compound is very narrow (see Fig. 4). Similar phases are encountered in many systems with rhenium, for example, rhenium – molybdenum [8].

Alloys with 55-83 weight % of rhenium have a two-phase structure, Zr_2Re + $ZrRe_2$ (Fig. 7).

LITERATURE CITED

1. H. Wallbaum, Naturwiss. 30, 149 (1942).
2. E. M. Savitskii and M. A. Tylkina, Zhur. Neorg. Khim. 3, 820 (1958).
3. A. Austin and J. Doig, J. Metals 9, 27 (1957).
4. P. I. Kripyakevich, M. A. Tylkina, and E. M. Savitskii. Nauchnye Doklady Vysshei Shkoly, Razdel "Metallurgiya" No. 3, 171 (1959).
5. P. Greenfield and P. Back, J. Metals 8, 265 (1956).
6. W. Trzebiatowski and J. Niemiec, Roczniki chem. 29, 277 (1955).
7. E. M. Savitskii, M. A. Tylkina, and Yu. A. Zot'ev, Zhur. Neorg. Khim. 4, 702 (1959).
8. E. M. Savitskii, M. A. Tylkina, and K. B. Pavarova, Zhur. Neorg. Khim. 4, 424 (1959).

EXTRACTION PROPERTIES OF DIISOAMYL METHYLPHOSPHINITE

V. B. Shevchenko, I. G. Slepchenko, V. S. Shmidt, and E. A. Nenarokomov

Translated from Atomnaya Énergiya, Vol. 7, No. 3, pp. 236-243, September, 1959
Original article submitted December 11, 1958

The properties of one of the new, efficient extractants for uranium, diisoamyl methylphosphinate (DAMP), are described. It was shown that uranyl nitrate is extracted from nitric acid solutions by this extractant with considerably higher distribution coefficients than tributyl phosphate (TBP). The extraction of uranyl nitrate and HNO_3 with DAMP solutions in hydrogenated kerosene was studied. It was shown that uranyl nitrate is extracted in the form of the complex $[UO_2(NO_3)_2(DAMP)_2]$, whose stability constant equals 2540 ± 200, and HNO_3 is extracted in the form of the compound HNO_3 DAMP, whose stability constant is 0.30 ± 0.03.

In recent years extractants with both high selectivity and considerable extracting capacity have been investigated [1, 2]. One of these extractants is TBP, which has been described in detail in the literature [1-14]. The coefficients of $UO_2(NO_3)_2$ distribution between nitric acid solutions and TBP are higher than for the diethyl and dibutyl esters, methyl isobutyl ketone, and other extractants which were previously used for the extraction of uranyl nitrate [15-19].

In the present work we give the results of studying the extraction properties of DAMP

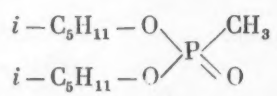

and solutions of it in hydrogenated kerosene.

The physical properties of DAMP are as follows: specific gravity 0.95 g/cc, boiling point at 7 mm Hg 130° C, viscosity 4.48 cp, flash point 130° C, and refractive index $n^{20}=1.4284$. The kerosene used as a diluent was a mixture of saturated hydrocarbons with a boiling point of 170-240° C and a specific gravity of 0.76 g/cc. Solutions of DAMP in kerosene were prepared by mixing appropriate volumes of these substances.*

For experiments with weighable amounts, the uranyl nitrate was purified by extraction with 20% TBP and subsequent reextraction with water. The isotope U^{233} was used in experiments with microamounts of uranium. The U^{233} preparation contained an appreciable amount of Th^{232}, and therefore the thorium was first separated from uranium by extraction of the latter from 6 N HCl with a 20% solution of TBP. It is known that thorium and protactinium are not extracted under these conditions. The reextract containing U^{233} was repeatedly evaporated, almost to dryness with excess HNO_3, and the final residue diluted to 5 ml with water. This gave a solution with a specific activity of $\sim 2 \cdot 10^6$ dis/ml · min. This solution was used as a stock solution of U^{233} and ~0.01 of its volume was introduced into an aqueous phase of the required composition.

Equal volumes of the phases were used for extraction. In work with weighable amounts of uranium the volume of each phase equaled 10 ml with microamounts of 2.0 ml.

The phases were mixed with a mechanical shaker for 30 min; the settling time was also 30 min. In work with weighable amounts of uranium, the distribution coefficients were determined as the ratio of the analytical concentrations of uranium in the organic and aqueous phases, and in work with microamounts of uranium, as the ratio of the α-activities of equal volumes of the organic and aqueous phases. Here the α-activity of the organic phase was calculated from the difference in the activity of the aqueous phase before and after extraction. In order to avoid a change in the phase volumes during the extraction of uranium in work with microamounts of uranium, before introduction of the U^{233}, the aqueous and organic solutions were equilibrated in a different separating funnel, from which the required volumes of solutions were withdrawn. The α-activity was measured on an α-scintillation counter. The experiments were at 19 ± 1° C.

The HNO_3 distribution coefficients were determined by titration of the aqueous phase and the aqueous

* The DAMP content of the extractant is given in percent by volume in every case.

reextract from the organic phase with 0.1 N NaOH solution.

Extraction of Nitric Acid

Curves of the equilibrium distribution of HNO_3 between aqueous solutions and solutions of DAMP in kerosene are given in Fig. 1. The relations between the HNO_3 distribution coefficients and the HNO_3 concentrations in the aqueous phase at various DAMP concentrations in the extractant are given in Fig. 2.

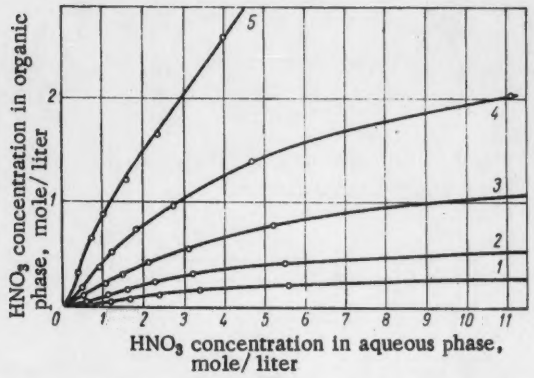
HNO3 concentration in organic phase, mole/liter
HNO3 concentration in aqueous phase, mole/liter
0 1 2 3 4 5 6 7 8 9 10 11
1 2
1 2 3 4 5

Fig. 1. Distribution of HNO_3 between aqueous solutions and extractant. Concentration of DAMP (vol. %): 1) 5; 2) 10; 3) 20; 4) 40; 5) 100.

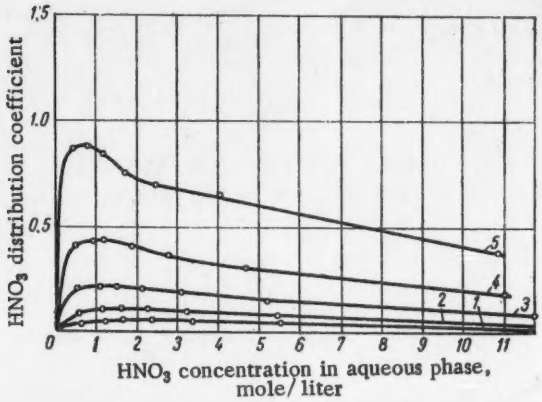

Fig. 2. Distribution coefficients of HNO_3 between the aqueous phase and the extractant. Concentration of DAMP (vol. %): 1) 5; 2) 10; 3) 20; 4) 40; 5) 100.

Figures 1 and 2 show that the distribution coefficient α_{HNO_3} increases with an increase in the DAMP concentration in the extractant. Here, as for TBP [11], with an increase in the acidity from 0 to 0.7 – –1.0 N there was an increase in α_{HNO_3}, connected with suppression of HNO_3 dissociation; with a further increase in acidity there was a fall in α_{HNO_3}, apparently caused by saturation of the extractant.

It can be conjectured that the extraction of HNO_3 by DAMP solutions, as with TBP [3, 5], is connected with the formation of a readily extractable complex by the reaction

$$H^+ + NO_3^- + \text{DAMP} \rightleftarrows HNO_3 \cdot \text{DAMP}. \quad (1)$$

Calculation of the equilibrium constant of this reaction

$$K = \frac{[HNO_3 \cdot \text{DAMP}]}{[H^+][NO_3^-][\text{DAMP}]}, \quad (2)$$

based on experimental data on the equilibrium distribution of HNO_3 (Tables 1 and 2), showed that the value of K remained constant at HNO_3 concentrations in the aqueous phase of up to 3 mole/liter and equaled 0.30 ± 0.03.

The experimental values of α_{HNO_3} and those calculated by means of this value of the constant are given in Tables 1 and 2. The calculation procedure in principle was the same as that described for the extraction of HNO_3 by tributyl phosphate [3]. The value of α_{HNO_3} was calculated by the formula

$$\alpha_{HNO_3} = K[H^+][D] = K N_x (D_0 - N_y), \quad (3)$$

TABLE 1. Distribution Coefficients of HNO_3 between Aqueous Solutions and a 20% Solution of DAMP in Kerosene (D_0 = 0.80 M; K = 0.30).

Equilibrium concentration of HNO_3, mole/liter		α_{exp}	α_{calc}
in aqueous phase	in organic phase		
1,05	0,22	0,21	0,17
1,46	0,31	0,21	0,21
2,12	0,43	0,20	0,22
3,05	0,57	0,19	0,18

TABLE 2. Distribution Coefficients of HNO_3 between Aqueous Solutions and a 10% Solution of DAMP in Kerosene (D_0 = 40.0 M; K = 0.30).

Equilibrium concentration of HNO_3, mole/liter		α_{exp}	α_{calc}
in aqueous phase	in organic phase		
1,13	0,116	0,10	0,10
1,57	0,167	0,11	0,11
1,24	0,236	0,11	0,11
3,21	0,318	0,10	0,08

where D_0 is the DAMP concentration in the extractant before extraction, D is the unbound DAMP concentration in the extractant after extraction, N_x is the equilibrium concentration of HNO_3 in the aqueous phase, and N_y that in the organic phase.

As the data in Tables 1 and 2 show, the calculated and experimental values of the HNO_3 distribution coefficients are quite close, indicating the accuracy of the hypothesis on the mechanism of HNO_3 extraction by DAMP solutions (1).

It is interesting to note that the equilibrium constant of the reaction $H^+ + NO_3^- + DAMP \rightleftharpoons HNO_3 \cdot DAMP$ derived for the extraction of DAMP differs comparatively little from the corresponding value for the extraction of HNO_3 by tributyl phosphate (0.22 ± 0.02), given in [3, 5]. This indicates that the difference in the stability of the compounds $HNO_3 \cdot DAMP$ and $HNO_3 \cdot TBP$ is comparatively small.

In Fig. 3, curve 1 shows the equilibrium distribution of HNO_3 between an aqueous solution and a 20% solution of DAMP containing 60 g/liter of uranium. As can be seen, when the DAMP solution was saturated with uranium, the HNO_3 distribution coefficient fell.

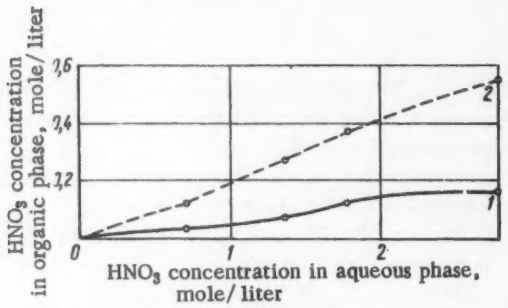

Fig. 3. Distribution of HNO_3 between an aqueous solution and a 20% solution of DAMP: 1) the organic phase contained 60 g/liter of uranium, 2) the organic phase contained no uranium.

Extraction of Uranyl Nitrate

Experiments with weighable amounts of $UO_2(NO_3)_2$. Curves of the equilibrium distribution of $UO_2(NO_3)_2$ between 0.05 N HNO_3 and solutions of DAMP in kerosene are presented in Fig. 4. The relations between the uranium distribution coefficients and the $UO_2(NO_3)_2$ concentrations in the aqueous phase for different DAMP concentrations in the extractant are given in Fig. 5. The same figures also show data for TBP [11] for comparison. Figures 4 and 5 show that when DAMP solutions are used as the extractant, the distribution coefficients of uranium between the aqueous and organic phases considerably exceed the corresponding values for TBP solutions of the same concentration. This

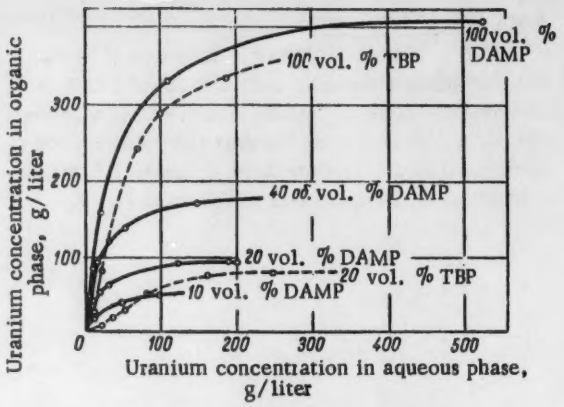

Fig. 4. Distribution of $UO_2(NO_3)_2$ between 0.05 N HNO_3 solution and extractant.

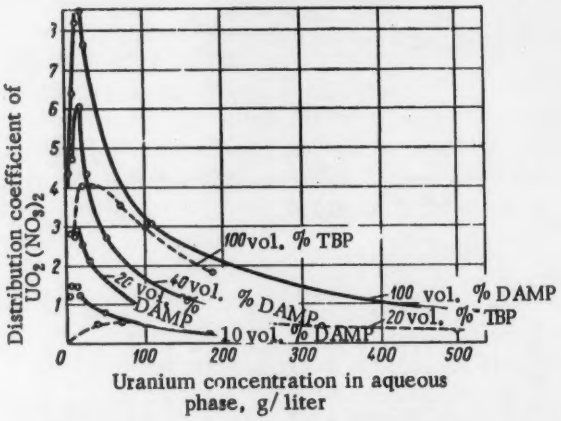

Fig. 5. Distribution coefficients of $UO_2(NO_3)_2$ between 0.05 N HNO_3 solution and extractant.

TABLE 3. Composition of DAMP Solutions, Saturated with Uranyl Nitrate.

DAMP content of extractant		Amount of uranium dissolved in extractant sample at saturation (the initial volume of the extractant sample was 1 liter)*		Ratio DAMP [U] in saturated organic solution
vol. %	mole/liter	g	mole	
10	0,40	48,6	0,202	1,98
20	0,80	94,0	0,395	2,03
40	1,6	186,2	0,790	2,03
100	4,0	473,8	1,99	2,01

* Due to the increase in volume of DAMP when $UO_2(NO_3)_2$ was dissolved in it, the volume of the organic solution containing the given amount of uranium exceeded 1 liter.

TABLE 4. Distribution Coefficients of $UO_2(NO_3)_2$ between 0.05 N HNO_3 and a 20% Solution of DAMP in Kerosene (D_0 = 0.80 M; K_U = 2540).

Equilibrium conc. of uranium				α_{exp}	α_{calc}
in aqueous phase		in organic phase			
g/ liter	mole/ liter	g/ liter	mole/ liter		
24,0	0,100	53,0	0,224	2,20	2,07
29,0	0,123	62,0	0,260	2,14	1,96
50,0	0,210	76,0	0,320	1,52	1,63
75,0	0,315	83,0	0,353	1,11	1,24
121,0	0,508	89,0	0,375	0,74	1,07

difference is especially marked for low uranium concentrations in the aqueous phase. With high uranium concentrations in the aqueous phase, saturation of the organic phase with uranium occurred. As Fig. 4 shows, the uranium content of the organic phase remained practically constant at uranium concentrations in the aqueous phase of ≥ 150 g/liter.

Data characterizing the composition of the organic phase at saturation are presented in Table 3.

The constancy of the ratio [DAMP] : [U] in the organic phase at different dilutions, saturated with uranium, shows that uranyl nitrate is apparently extracted in the form of the complex $UO_2(NO_3)_2$ 2DAMP, formed by the reaction:

$$UO_2^{2+} + 2NO_3^- + 2\ \text{DAMP} \rightleftarrows \rightleftarrows UO_2(NO_3)_2\,2\ \text{DAMP}. \quad (4)$$

Calculation of the equilibrium constant of this reaction from experimental data

$$K_U = \frac{[UO_2(NO_3)_2\,2\ \text{DAMP}]}{[UO_2^{2+}]\,[NO_3^-]^2\,[\text{DAMP}]^2\gamma^3} \quad (5)$$

for a 20% solution of DAMP in kerosene shows that the value of K_U remains constant with changes in the uranium concentration in the aqueous phase over a wide range and equals 2540 ± 200. Table 4 gives experimental values of the distribution coefficients of $UO_2(NO_3)_2$ and values calculated from the value of K_U. The calculation was carried out by means of the formula given for extraction equilibria with TBP [12] with the DAMP concentrations substituted in the formula instead of the TBP concentrations:

$$\alpha_U = K_U (2x)^2 D^2 \gamma^3, \quad (6)$$

where K_U = 2540, x is the equilibrium concentration of uranium in the aqueous phase, D is the equilibrium concentration of free DAMP in the organic phase (D = = $D_0 - 2y$, where D_0 is the initial concentration of DAMP in the extractant and y is the equilibrium concentration of uranium in the organic phase), and γ are the activity coefficients of uranyl nitrate, whose values are taken from [20].

Formula (6) was deduced from (5) on the basis of the extraction mechanism expressed by (4). Here it was assumed that the whole of the uranium in the organic phase was in the form $UO_2(NO_3)_2$ 2DAMP, and in the aqueous phase as UO_2^{2+}.

The satisfactory agreement of the calculated and experimental values of α indicates the accuracy of the hypothesis made on the mechanism of uranyl nitrate extraction by DAMP solutions.

As can be seen from the data presented, the stability constant of the complex $UO_2(NO_3)_2$ with DAMP is extremely high and is approximately 39 times greater than the corresponding constant for TBP (~66) [12]. Such a high value of K_U indicates that NO_3^- ions and DAMP molecules are apparently in the internal coordination sphere of the complex formed; the composition of the latter is probably expressed by the formula $[UO_2(NO_3)_2(DAMP)_2]$.

A rise in the HNO_3 content of the aqueous phase over the concentration range studied produced an appreciable increase in the distribution coefficient of uranium. Curves of the equilibrium distribution of $UO_2(NO_3)_2$ between aqueous solutions of various acidities and 20 and 40% solutions of DAMP are shown in Figs. 6 and 7. As has been shown [13], with simultaneous

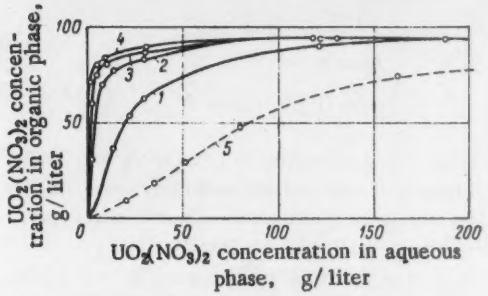

Fig. 6. Dependence of the $UO_2(NO_3)_2$ distribution between an aqueous solution and extractant containing 20% of DAMP on the HNO_3 concentration in the aqueous phase: 1) 0.5 N HNO_3; 2) 1.0N HNO_3; 3) 2.0 N HNO_3; 4) 3.0 N HNO_3; 5) distribution of $UO_2(NO_3)_2$ between 0.05 N HNO_3 and 20% TBP [12].

extraction of $UO_2(NO_3)_2$ and HNO_3 by tributyl phosphate, the uranium content of the organic phase may be calculated from the formula

$$y = \frac{1}{2}\left[T_0 - \frac{\sqrt{1+8FT_0}-1}{4F}\right], \quad (7)$$

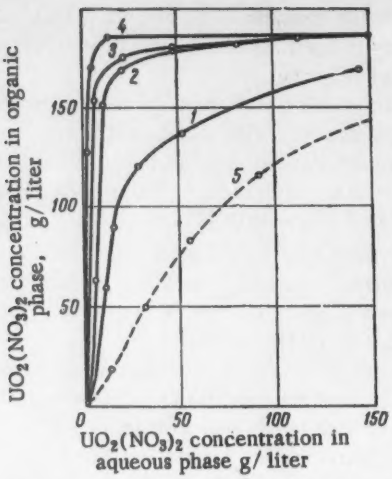

Fig. 7. Dependence of the $UO_2(NO_3)_2$ distribution between an aqueous solution and extractant containing 40% of DAMP on the HNO_3 concentration in the aqueous phase: 1) 0.05 N HNO_3; 2) 1.0 N HNO_3; 3) 2.0 N HNO_3; 4) 3.0 N HNO_3; 5) distribution of $UO_2(NO_3)_2$ between 0.05 N HNO_3 and 40% TBP [12].

where T_0 is the TBP concentration in the extractant before extractions;

$$F = f_U/(1+f_H)^2; \tag{8}$$

$$f_U = K_U\gamma^3(2x+N_x)^2; \tag{9}$$

$$f_H = 0{,}2N_x(2x+N_x).$$

Since the mechanisms of $UO_2(NO_3)_2$ and HNO_3 extraction by DAMP and TBP solutions are analogous, the formulas presented should evidently also apply to extraction equilibria with DAMP.

Replacing the coefficient 0.2 in (9) by 0.3 (the equilibrium constant of HNO_3 extraction) and substituting the value $K_U = 2540$ in (8), we calculated the values of γ and α_U. The experimental and calculated values of α_U for extraction of $UO_2(NO_3)_2$ from 1.0 N HNO_3 with a 20% solution of DAMP are given in Table 5.

Table 5 shows that at uranium concentrations in the aqueous phase of 0.10 – 0.16 mole/liter, the calculated values of α_U agree quite well with the experimental values. This also confirms the accuracy of the hypothesis on the extraction mechanism (4) and the accuracy of the value of K_U used (2540). However, calculations for uranium concentrations less than 0.1 M could not be carried out as there are no appropriate data on the activity coefficients of uranyl nitrate. For $UO_2(NO_3)_2$ concentrations in the aqueous phase greater than 0.16 M, the organic phase was almost saturated with uranium and calculation by (7) gave a large error.

TABLE 5. Distribution Coefficients of $UO_2(NO_3)_2$ between 1.0 N HNO_3 and a 20% Solution of DAMP in Kerosene ($D_0 = 0.80$ M; $K_U = 2540$).

Equilibrium conc. of uranium				α_{exp}	α_{calc}
in aqueous phase		in organic phase			
g/liter	mole/liter	g/liter	mole/liter		
23,8	0,100	82,0	0,344	3,44	3,47
30,1	0,126	83,2	0,355	2,82	2,81
37,6	0,158	85,8	0,361	2,14	2,14

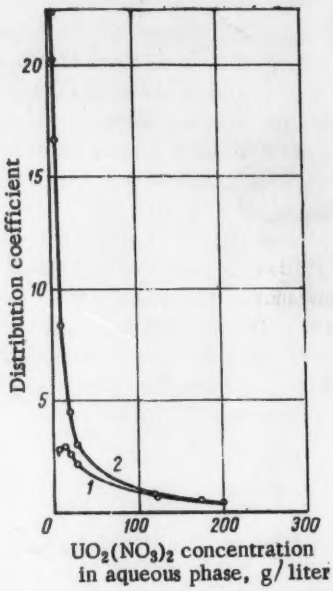

Fig. 8. Dependence of the coefficient of $UO_2(NO_3)_2$ distribution between nitric acid solution and 20% DAMP solution on the uranium content of the aqueous phase. Acidity of aqueous phase: 1) 0.05 N HNO_3; 2) 2.0 N HNO_3.

Figure 8 shows the dependence of the coefficients of $UO_2(NO_3)_2$ distribution between 0.05 and 2.0 N aqueous HNO_3 solutions and a 20% DAMP solution on the uranium content of the aqueous phase. The figure shows that with 2.0 N HNO_3 the distribution coefficients are particularly great at low uranium concentrations in the aqueous phase (up to a value of ~5 g/liter). This shows the efficiency of using DAMP in cases where it is necessary to completely extract $UO_2(NO_3)_2$ from the aqueous phase.

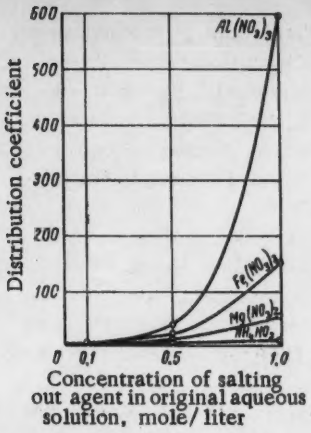

Fig. 9. Dependence of the coefficient of $UO_2(NO_3)_2$ distribution between aqueous solutions and 20% DAMP solution on the content of salting-out agent in the original aqueous solution.

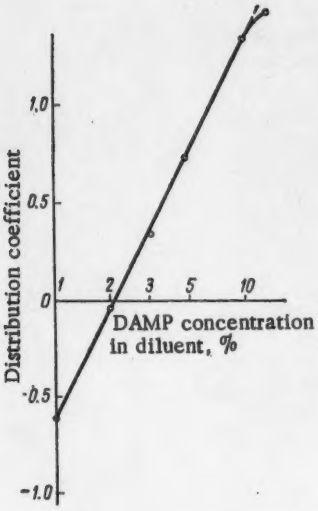

Fig. 10. Dependence of the distribution coefficient of microamounts of $UO_2(NO_3)_2$ on the DAMP concentration in the extractant (in logarithmic coordinates).

The introduction of salting-out agents into the solution considerably increased the uranium distribution coefficients (Fig. 9). Aluminum, iron, and magnesium nitrates were particularly efficient salting-out agents.

Experiments with microamounts of $UO_2(NO_3)_2$. As an additional check on the accuracy of the $UO_2(NO_3)_2$ extraction mechanism proposed, we measured the relation between the distribution coefficient of microamounts of $UO_2(NO_3)_2$ and the DAMP concentration in the extractant (Fig. 10). The relation $\lg \alpha = f\{\lg [D]\}$ was expressed by a straight line with a slope equal to 2, which would be expected for extraction of a complex containing two molecules of extractant. A linear relation was observed only for DAMP concentrations $\leq 10\%$. With a further rise in the DAMP concentration, the line deviated toward the abscissa axis.

The data presented show that DAMP is a stronger extractant for uranium than TBP.

The relations between the distribution coefficients and the composition of the aqueous and organic solutions studied indicate that the compound extracted is the complex $UO_2(NO_3)_2(DAMP)_2$.

SUMMARY

1. A study was made of the dependence of the coefficients of HNO_3 and uranyl nitrate distribution between nitric acid solutions and kerosene solutions of DAMP on the DAMP content of the extractant and on the $UO_2(NO_3)_2$ and HNO_3 contents of the aqueous phase. It was shown that under identical conditions DAMP extracts considerably more uranium than TBP, especially with low uranium concentrations in the aqueous phase.

2. The rules of HNO_3 extraction by DAMP solutions may be explained on the basis of the following extraction mechanism:

$$H^+ + NO_3^- + \text{DAMP} \rightleftarrows HNO_3 \cdot \text{DAMP}$$

where $HNO_3 \cdot$ DAMP is the compound extracted completely into the organic phase.

3. The rules of uranium extraction from nitric acid solutions by DAMP solutions may be explained satisfactorily if it is assumed that extraction is determined by the reaction:

$$UO_2^{2+} + 2NO_3^- + 2\,\text{DAMP} \rightleftarrows [UO_2(NO_3)_2(\text{DAMP})_2],$$

where $[UO_2(NO_3)_2(DAMP)_2]$ is the compound extracted completely into the organic phase.

4. We determined the equilibrium constants of the reactions

$$H^+ + NO_3^- + \text{DAMP} \rightleftarrows HNO_3 \cdot \text{DAMP}$$

and

$$UO_2^{2+} + 2NO_3^- + 2\,\text{DAMP} \rightleftarrows [UO_2(NO_3)_2(\text{DAMP})_2].$$

The constant for the reaction of HNO_3 with 10 and 20% solutions of DAMP equals 0.30 ± 0.03.

The equilibrium constant of the reaction of $UO_2(NO_3)_2$ with 20% DAMP equals 2549 ± 200.

LITERATURE CITED

1. A. V. Nikolaev, Khim. Nauka i Prom. 1, 548 (1957).
2. McKay, Material of the International Conference on the Peaceful Uses of Atomic Energy (Geneva, 1955) [in Russian] (Goskhimizdat, Moscow, 1958) Vol. 7, p. 388.
3. V. V. Fomin and E. P. Maiorova, Zhur. Neorg. Khim. 1, 1703 (1956).
4. V. B. Shevchenko, A. S. Solovkin, and I. V. Shilin, Zhur. Neorg. Khim. 3, 225 (1958).
5. A. S. Solovkin, Zhur. Neorg. Khim. 2, 611 (1957).
6. V. D. Nikol'skii and V. S. Shmidt, Zhur. Neorg. Khim. 2, 2746 (1957).
7. N. S. Povitskii, I. V. Shilin, and A. S. Solovkin, Zhur. Neorg. Khim. 3, 222 (1958).
8. A. V. Nikolaev, A. A. Sorokina, and A. S. Maslennikova, Zhur. Neorg. Khim. 3, 160 (1958).
9. V. D. Nikolskii and V. S. Shmidt, Zhur. Neorg. Khim. 3, 2467 (1958).
10. V. V. Fomin, R. E. Kartushova, and T. I. Rudenko, Zhur. Neorg. Khim. 3, 2117 (1958).
11. S. M. Karpacheva, L. P. Khorkhorina, and A. M. Rozen, Zhur. Neorg. Khim. 2, 1441 (1957).
12. A. M. Rozen and L. P. Khorkhorina, Zhur. Neorg. Khim. 2, 1956 (1957).
13. A. M. Rozen, Atomnaya Énergiya 2, 445 (1957). †
14. A. Levitt and E. Freund, J. Am. Chem. Soc. 78, 1547 (1956).
15. V. M. Vdovenko, M. P. Kovaleva, and T. V. Koval'skaya, Zhur. Neorg. Khim. 2, 1677 (1957).
16. F. Culler, Material of the International Conference on the Peaceful Use of Atomic Energy (Geneva, 1955) [in Russian] (Geskhinzdat, Leningrad, 1958) Vol. 9, p. 179.
17. S. M. Karpacheva, L. P. Khorkhorina, and G. D. Agashkina, Zhur. Neorg. Khim. 2, 966 (1957).
18. F. Bruce, Material of the International Conference on the Peaceful Uses of Atomic Energy (Geneva, 1955) [in Russian] (Geskhinizdat, Moscow, 1958) Vol. 7, p. 127.
19. D. Peppard, J. Inorg. and Nucl. Chem. 4, 325 (1957).
20. I. Robinson, J. Chem. Soc. 1840 (1951).

† Original Russian pagination. See C. B. translation.

SOME PRINCIPLES FOR THE DESIGN AND USE OF POWERFUL IRRADIATORS

A. V. Bibergal', M. M. Korotkov, and T. G. Ratner

Translated from Atomnaya Énergiya, Vol. 7, No. 3, pp. 244-251
September, 1959
Original article submitted March 4, 1959.

This paper describes an experimental investigation of the accumulation factor in the region of small distances, of γ radiation from Co^{60} and Cs^{137} point-sources. The possibility of using literature data for a homogenous infinite medium for practical calculations (under conditions of barrier geometry for a relatively small thickness of absorbing layers) is demonstrated. The possibility of equalizing the dosage field of a cylindrical irradiator by means of additional filters has been proven by experiment. Moreover, the authors propose to replace Co^{60} specimens with Cs^{137} specimens in irradiating objects with a thickness of up to 40 cm and a density ≤ 1.

One of the important possibilities for the use of radioactive isotopes is their application in γ devices for the irradiation of different specimens for experimental and industrial purposes in the field of biology, agriculture, and radiation chemistry.

In the majority of cases, the irradiation of comparatively large-size specimens with a density close to unity is required. In this, it is most convenient to use long-lived isotopes which emit high-energy γ radiation. Co^{60} and Cs^{137} are such isotopes.

Gamma apparatuses with Co^{60} and, especially with Cs^{137} can be mobile, and they do not require a frequent replacement as sources. An important advantage of these isotopes, especially in the case they are used for scientific research experiments, is the fact that their γ radiation is relatively monochromatic.

The basic characteristics of irradiators are:

1) the radiation dose rate P (r/min) at the center of the irradiator operating volume and the required degree of its regulation;

2) the magnitude of the irradiator operating volume V (cm^3);

3) the maximum allowable degree of nonuniformity of the dosage field in the operating volume ($\delta = (P_{max}/P_{min})\ 100\%$);

4) efficiency of the γ device (kg/hr);

5) the over-all activity Q (g-equiv Ra or C) of isotope sources.

Irradiation characteristics are interdependent, and they are determined by the irradiator shape, the irradiation method, and the object parameters.

Depending on the purpose for which the device is used, certain characteristics are of greater or lesser importance. Thus, for instance, in radiobiological experiments on animals and plants, the uniformity of the dosage field in the operating volume and the possibility of changing the dosage rate in a wide range are especially important, but the irradiator efficiency and the amount of the isotope used are of no special importance. Conversely, the following characteristics determining the device efficiency are of special importance in industrial devices: the required amount of the isotope and the output; the dosage field uniformity is of lesser importance, and, in the majority of cases, the dosage rate does not have to be changed at all [1 and 2].

In irradiator design, the integral dose which a specimen of a given size and density is to receive over the entire period of irradiation in the device and the magnitudes of the first four characteristics are usually determined. The amount Q of the radioactive substance in the irradiator must be determined. The assigned requirements are satisfied by selecting the irradiator shape, its parameters, and the irradiation method. However, because of the large number of different factors affecting the quantity Q, usually several variants of the device are designed. Therefore, the design method is of great importance in practice. Until now, no papers devoted to general problems in the design of powerful γ devices for radiation treatment have been published. Only papers devoted to the development and calculation of individual devices [3, 4 and 5] and to calculations of the dosage field of extended sources of different shapes [6, 7, 8, 9, 10, and 11] are available. The majority of the theoretical solutions available in the latter papers are not suitable for practical calculations, where a number of specific requirements, which cannot be easily foreseen in general theoretical derivations, have to be taken into account.

The purpose of the present paper is the following:

1) experimental verification of the admissibility of certain approximate calculations by comparing the

calculations with measurements performed under actual operating conditions on a γ device which is in use;

2) determination of the most suitable irradiation method in using extended sources;

3) determination of the fields of application of Co^{60} and Cs^{137} for irradiation.

Experimental Verification of Some Approximate Calculation Methods

If a dosage field where an absorber is present is to be calculated, the multiple-scattered radiation in the given medium should be taken into account. The Fano theory [12] for the dose rate from a point-source in a homogenous medium gives the following expression:

$$P = P_0 B_0 e^{-\mu_0 F},$$

where μ_0 is the linear attenuation coefficient of a narrow beam in a given medium, F is the distance from the source to the measurement point, B_0 is the accumulation factor, which takes into account the contribution of scattered radiation, and P_0 is the dose rate in air, provided by the source at the measurement point. The accumulation factor B_0 can be represented as the sum of two exponentials [9] of the following form

$$B_0 = A_1 e^{-\alpha_1 \mu_0 F} + A_2 e^{-\alpha_2 \mu_0 F}.$$

For γ radiation of Co^{60} and Cs^{137} in a medium equivalent to water with respect to its absorption-scattering capacity, the expression determining the dose rate provided by a point-source assumes the following form:

$$P = \frac{K_\gamma Q}{60 \cdot F^2}(8{,}9e^{-0{,}057F} - 7{,}9e^{-0{,}067F})\ \text{r/min} \quad (\text{for } Co^{60}), \tag{1}$$

$$P = \frac{K_\gamma Q}{60 \cdot F^2}(19{,}5e^{-0{,}0753F} - 18{,}5e^{-0{,}086F})\ \text{r/min} \quad (\text{for } Cs^{137}), \tag{2}$$

where Q is the point-source activity. The values of the coefficients in the expression for the accumulation factor are taken from [9].

For a linear source, for a point at the distance F from the middle of the source, we similarly obtain

$$P = \frac{2K_\gamma q}{60F}\left[8{,}9\int_0^{\operatorname{arctg}\frac{L}{F}} e^{-0{,}057F\cdot\sec\varphi}\,d\varphi - 7{,}9\int_0^{\operatorname{arctg}\frac{L}{F}} e^{-0{,}067F\cdot\sec\varphi}\,d\varphi\right]\text{r/min} \quad (\text{for } Co^{60}), \tag{3}$$

$$P = \frac{2K_\gamma q}{60F}\left[19{,}5\int_0^{\operatorname{arctg}\frac{L}{F}} e^{-0{,}0753F\cdot\sec\varphi}\,d\varphi - 18{,}5\int_0^{\operatorname{arctg}\frac{L}{F}} e^{-0{,}086F\cdot\sec\varphi}\,d\varphi\right]\text{r/min} \quad (\text{for } Cs^{137}), \tag{4}$$

where L is the half-length of the linear source, K_γ is the γ constant, and q is the linear specific activity (g-equiv /cm or C/cm).

If the absorbing medium fills only a part of the gap F, the degree of accuracy provided by the approximate expressions (1)-(4) should be checked.

Moreover, on the basis of an experimental check [13] which was performed with a Co^{60} point-source in water, it has been found that the Fano theory yields a somewhat higher value for the accumulation factor in the region of small distances, where 100 cm > F > 45 cm. Similar investigation for γ radiation of Cs^{137} in water has not been performed. In the above paper [13], the region near the source where F < 45 cm, which is of special interest in the design of irradiators, has not been investigated. Therefore, it was first necessary to determine the dependence of the accumulation factor on the distance F in water. This has been performed for a Co^{60} specimen with an activity of 952 mg-equiv Ra. A comparison of the obtained results with data from [13] and calculation data is given in Fig. 1. For Co^{60} radiation in the F < 45 cm interval, in which we are interested, a good agreement between theoretical data from [9] and experimental results was observed. For the Cs^{137} radiation, it appeared that the theoretical values of the accumulation factor B_0, which were calculated for coefficients from [9], are somewhat larger than the experimental values. These data must be obviously checked again for a larger interval of F values.

The comparison of experimental and theoretical data for linear and a cylindrical irradiator with Co^{60} radiation is shown in Figs. 2 and 3. Figure 2 provides

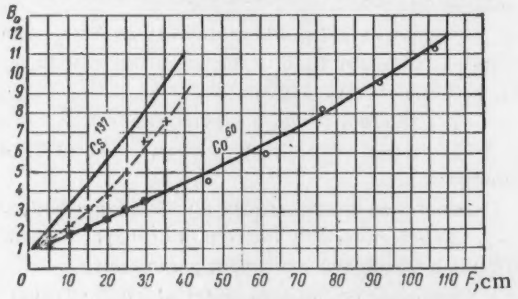

Fig. 1. Accumulation factor B_0 for water and γ radiation of Co^{60} and Cs^{137} point-sources. -x-) Cs^{137}; •) Co^{60}; O) data from [13]; —) calculation with respect to data from [9].

data for linear sources which are 40 and 80 cm long. It is obvious from the figure that an entirely satisfactory agreement between theoretical and experimental data can be observed when (3) is used for calculations. Figure 3 shows experimental data obtained in determining the dose rate at the center of a cylindrical irradiator consisting of eight rods, each having a length of 40 cm, which were arranged along the cylinder generatrices. The rods could be shifted simultaneously, whereby the irradiator diameter would be changed [3]. The irradiator was placed in water (in a well 3.5 m deep and 1.5 m in diameter). A chamber, made of 2-mm thick iron with a diameter and height of 30 cm, which was filled with water, was also placed in the irradiator. The measurements were performed at the irradiator center without the chamber (directly at the center in water) and at the chamber center. Considering that the irradiator diameter was changed from 40 to 100 cm and that the radiation scattered by the well walls thus passed through a distance in water of not less than 1 m before reaching the measurement point, the medium extent could be considered as infinite.

The measurement results obtained for the irradiator center were divided by 8 for a comparison with the results obtained in measuing the dose rate from a single rod.

The good agreement between theoretical and experimental data for the central point of the irradiator in a homogenous medium is still not a sufficient indication that (3) and (4) are valid for all cases which can be encountered in practice. Actually, in the case where the dosage field is calculated for air, the absorbing layer of water inside the chamber occupies only a portion of the distance from the source to the measurement point, and the radiation from different sections of linear sources will pass through different thicknesses of water and air layers. In the case where the cylindrical irradiator is in air and the chamber is filled with the object to be irradiated (in our case, water), the radiation passes through an absorbing layer which cannot be considered as infinite. Thus, the amount of multiple-scattered radiation is smaller than in the first case.

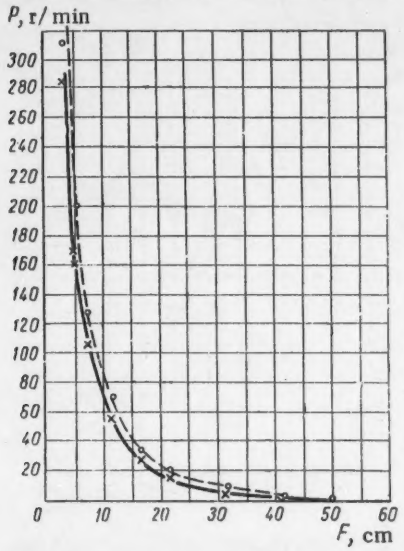

Fig. 2. Dependence of the radiation dose rate of Co^{60} linear sources in water on distance (F, cm) for q = 2.2 g-equiv Ra/cm: 2L = 40 cm (— by calculation, × by experiment); 2L =80 cm (--- by calculation, O by experiment).

Thus, we have four nonequivalent cases with respect to radiation scattering and absorption conditions which can be encountered in practice. Conventionally, we shall call them the water – water, water – air, air – water, and air – air cases.

Expressions (3) and (4) for the water – air and air – water cases yield the same results in the case where R = 1/2F, where R is the radiation path in water.

The dependence of the dose rate on the irradiator diameter was investigated for all four cases. Measurements by the ionization and the chemical methods were performed at two points inside the chamber (d = = 30 cm; l = 30 cm): at the chamber center and at

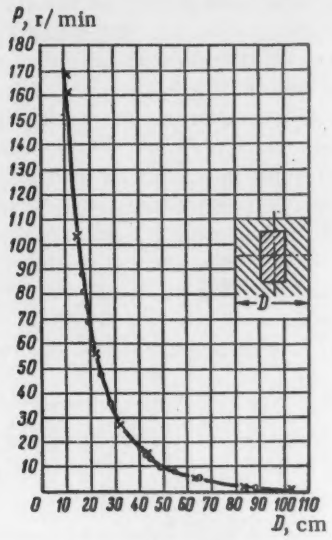

Fig. 3. Comparison of dose rate measurements for radiation from a linear source and for radiation at the center of a cylindrical Co^{60} irradiator in water with calculation data. ×) Linear source: 2L = 40 cm; o) measurements without a chamber ($1/8P_0$ at the irradiator center); O)measurements in the chamber ($1/8\ P_0$ at the irradiator center); —) theoretical data.

the distance of 12 cm from the center. This made it possible to determine the manner in which the dosage field changes with an increase in the irradiator diameter for various cases of irradiation. For the air – air case, the measurements were performed only for the central point (C = 0), which was due to the fact that in measurements inside a well 1.5 m in diameter a considerable amount of radiation scattered by the well walls cannot be avoided.

In order to establish whether theoretical and experimental data agree under conditions where the presence of a considerable amount of scattered radiation was eliminated, the dose rate from a single linear source (2L = 40 cm, q = 2.05 g-equiv Ra/cm) was measured in air outside the well. The measurement results are shown in Fig. 4. The measurements in air at the irradiator center (Fig. 5) showed that the amount of radiation scattered by the well walls was approximately equal to 7-10%. Therefore, in further experiments for the air – air case, we used calculation data for the dose rate at the points C = 0 and C = 12 cm.

The measurement results for the water – air, water – water, and air – water cases are shown in Figs. 6, 7, and 8, respectively. It is obvious from these figures that, for practical purposes, an entirely satisfactory agreement between calculation and experimental data was obtained. However, for the air – water case, a deviation of 10-12% was observed (due to a smaller amount of scattered radiation than was the case for the water – air combination). For practical purposes, the indicated discrepancy is not very important.

In the majority of cases, (3) and (4) for a linear source provide the possibility of designing all irradiator shapes which are important in practice (cylinder, plane, two planes, and a system of linear sources), since all these irradiators are usually composed from a larger or smaller number of rods filled with radioactive preparations. Therefore, calculations with respect to individual rods, especially in those cases where they are not numerous, provide more accurate results than calculations where equations for a continuous plane and a hollow cylinder are used.

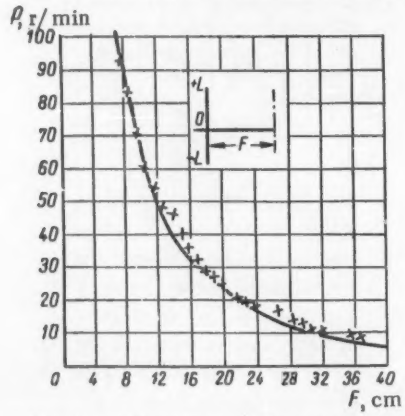

Fig. 4. Dependence of the dose rate in radiation from a Co^{60} linear source in air on distance for 2L = 40 cm and q = 2.05 g-equiv Ra/cm. —) by calculation; x) by experiment.

Determination of the Most Suitable Method for the Irradiation of Objects

The aim in designing powerful γ devices for radiation treatment is, in the first place, the determination of the amount of radioactive substances necessary for creating a dosage field of an assigned magnitude and

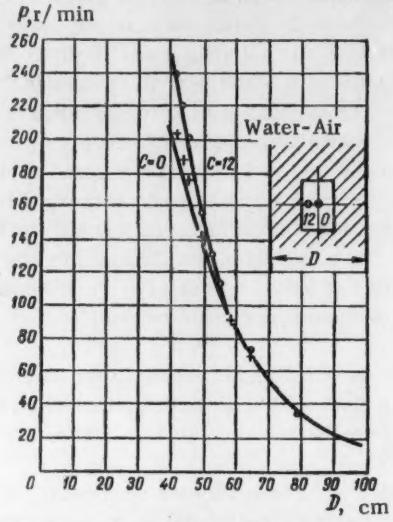

Fig. 5. Dependence of the radiation dose rate inside a Co^{60} cylindrical irradiator in air on the irradiator diameter. —) By calculation; +) by experiment (C= 0).

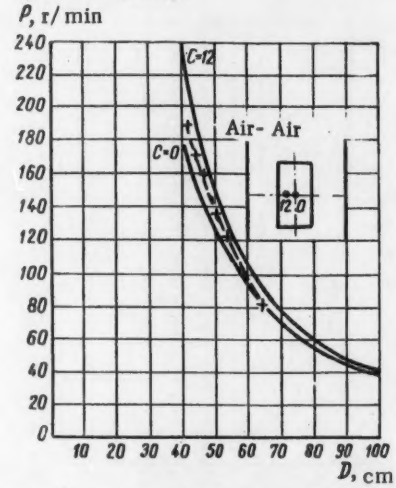

Fig. 6. Dependence of the radiation dose rate in air inside the chamber for objects (d = 30 cm) on the diamter of a Co^{60} irradiator which is immersed in water. —) By calculation, +) by experiment (for C= 0); —) by calculation, O) by experiment (for C=12).

uniformity in a given volume. Therefore, it is extremely important to determine which irradiation method secures the greatest efficiency of isotopes. For this, it is necessary to compare the dependence of the degree of the dosage field nonuniformity on irradiator parameters for different cases with the dose rate obtained at the irradiator center. In this manner, it is possible to determine the cases where the amount of isotopes can be reduced if the assigned irradiation nonuniformity and the dose rate are attained.

Figure 9 shows the dependence of the degree of the dosage field nonuniformity on the diameter of a cylindrical irradiator for different cases. Therefore, experimental data (see Fig. 8, the dash-dot line) are used in calculating the nonuniformity percentage for the air – water case, and calculation data are used for the air – air case.

As was mentioned above, the degree of nonuniformity was defined as the ratio of the dose rate at the point C = 12 cm to the dose rate at the point C = 0 For a certain given degree of the dose field nonuniformity, different irradiator diameters will be required for different irradiation cases, whereby different absolute magnitudes of the dose rate at the irradiator center will be secured. Naturally, irradiation methods where, for a given dose field uniformity, the maximum dose rate is secured are the most suitable. If we accept a degree of nonuniformity which is often encountered in practice (P_{12}/P_0) 100 = 110%), then, for different cases, we obtain:

Air – Air. . . D = 71.5 cm and P_0 = 66 r/min (by calculation);

Water – air. . . D = 48.5 cm and P_0 = 142 r/min (by calculation and experiment);

Air – water. . . D > 100 cm and P_0 < 31 r/min (by calculation; P_0 < 28 by experiment);

Water-Water. . . D = 71.5 cm and P_0 = 34 r/min (by calculation and experiment).

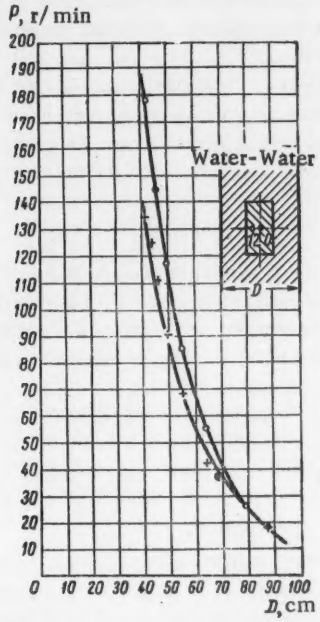

Fig. 7. Dependence of the radiation dose rate in water inside the chamber for objects (d = 30 cm) on the diameter of a Co^{60} irradiator which is immersed in water. —) By calculation, +) by experiment (for C=0); —) by calculation, o) by experiment (for C=12).

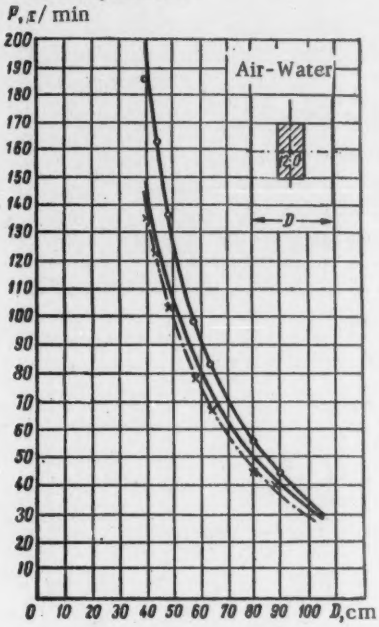

Fig. 8. Dependence of the radiation dose rate in water inside the chamber for objects (d=30 cm) on the diameter of a Co^{60} irradiator which is in air. —) By calculation, -x.-x.-) by experiment (for C=0); —) by calculation, O) by experiment (for C = 12).

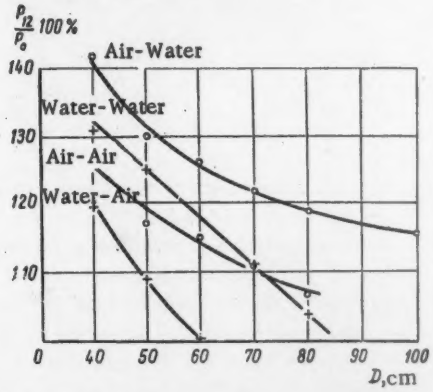

Fig. 9. Dependence of the dosage field nonuniformity in a cylindrical irradiator on its diameter.

Thus, the dose field uniformity increases when an additional water layer outside as well as inside the object is present. For the same assigned dose field nonuniformity, this makes it possible to reduce the irradiator diameter, and, consequently, to secure either a larger dose rate or to save the radioactive substance. For a given device, in the cases where the objects slightly distort the dose field in air (as can be seen from a comparison of the water – air and air – air cases), a double saving of radioactive substances can be secured. The authors of [4] obtained similar results in designing an irradiator consisting of two flat surfaces; they noted the usefulness of applying either additional flat filters or of increasing the thickness of flat isotope sources.

Thus, the radiation treatment of objects requiring a high degree of irradiation uniformity should be performed in the presence of specially designed additional filters. This irradiation method would be especially suitable for objects of small sizes and densities i.e., for objects which cause slight distortions of the dose field in air.

Applicability Ranges of Co^{60} and Cs^{137} Isotopes for Irradiation

An important problem in irradiation practice is the right choice of the isotope to be used as a γ-radiation source. As was indicated above, Co^{60} and Cs^{137} are the most promising isotopes at the present time, however, no quantitative comparisons between these isotopes have been made.

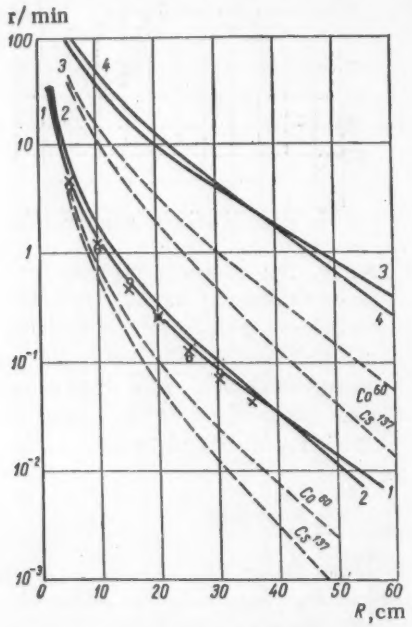

Fig. 10. Attenuation of broad (full lines) and of narrow (dotted lines) beams of γ-rays from point and linear sources in water. 1) Co^{60} point-source, broad beam, Q = 1 g-equiv Ra, •) by experiment; 2) Cs^{137} point source, broad beam, Q = 1 g-equiv Ra; x by experiment; 3) Co^{60} linear source; broad beam; Q = 100 g-equiv Ra, 2L = 100 cm; 4) Cs^{137} linear source: broad beam, Q = 100 g-equiv Ra, 2L = 100 cm; – – –) narrow beams.

Figure 10 provides a comparison of the dose rate dependences on distance for point and linear Co^{60} and Cs^{137} sources for broad and narrow beams. The dose rate was calculated according to (1) - (4) for a homogenous medium (water), where the activity of point-sources was assumed to be equal to Q = 1 g-equiv Ra, and the linear specific activity of linear sources was assumed to be q = 1 g-equiv Ra/cm.

It is obvious from the figure that for distances of less than 40 cm, the dose rate values for Cs^{137} which were obtained by calculation are somewhat larger than the dose rates obtained with Co^{60} sources. The experimental dose rate values in this interval are equal. From a comparison of the dose rate dependences on distance for Co^{60} and Cs^{137} sources, we can draw the conclusion that the application of Cs^{137} preparations (with an equivalent radiation yield) for objects with a thickness of up to ~ 40 cm is more suitable than the application of Co^{60} preparations, which is important in practice.

In practice, it is most often necessary to irradiate objects of a thickness less than 40 cm and of a density equal to 1 or less. Therefore, for a great majority of γ devices, it is more convenient to use Cs^{137} preparations because of the longer half-life of Cs^{137} and a smaller required shield thickness, especially if heavy material is used.

The use of Co^{60} is rational only in the case where it is necessary to irradiate large-size objects of great density or if very high dose rates, which depend on the magnitude of the specific activity of preparations, are to be secured.

SUMMARY

1. In the design of irradiators of γ devices, for all cases encountered in practice, the consideration of multiple scattering by means of the accumulation factor, expressed by the sum of two exponentials, secures a sufficient accuracy.

2. The most suitable method of irradiating objects which require the presence of a uniform dose field is the use of additional filters which equalize the dose fields of extended sources. These filters must be calculated for each individual case.

3. For the irradiation of objects with a thickness of less than 40 cm and a density not exceeding 1, the use of Cs^{137} preparations as γ-radiation sources is much more efficient than the use of Co^{60} preparations.

LITERATURE CITED

1. A. V. Bibergal', V. L. Karpov, and V. I. Sinitsyn, "High-intensity cobalt sources of irradiation treatment," Report No. 2234, submitted to the Second International Conference on the Peaceful Uses of Atomic Energy (Geneva, 1958).

2. A. V. Bibergal', U. Ya. Margulis, and V. G. Khrushchev, "Principles and techniques in using radioactive substances as powerful gamma-sources in radiobiology and medicine." Transactions of the All-Union Scientific Research Conference on the Application of Radioactive and Stable Isotopes in National Economy and Science [in Russian] (Izd. AN SSSR, Moscow, 1958).
3. A. V. Bibergal', M. M. Korotkov, and O. G. Arakelov, Biofizika No. 1, 118-121 (1958).
4. B. Manowitz, O. Kyhl, D. Richman, and L. Galanter, "Development of high-power irradiators," Report No. 1069, submitted by the USA to the Second International Conference on the Peaceful Uses of Atomic Energy (Geneva, 1958).
5. A. Kh. Breger, V. A. Belynskii, and S. D. Prokudin, Atomnaya Énergiya 4, 131 (1956).*
6. G. V. Gorshkov, Gamma Radiation of Radioactive Bodies [in Russian] (Leningrad State Univ. Press, Leningrad, 1956).
7. E. E. Kovalev, V. I. Popov, L. N. Smirennyi, Atomnaya Énergiya 2, 2, 181 (1957). *
8. E. E. Kovalev, Atomnaya Énergiya 2, 6, 538 (1959).*
9. Rockwell, Reactor Shielding Design Manual (Van Nostrand, Princeton, N. J., 1956). Chapts. 9, 10.
10. B. Price, C. Horton and K. Spinney, "Radiation shielding," International Series of Monographs on Nuclear Energy Div. X, Vol. 2 (Pergamon Press, London – New York – Paris, 1957).
11. N. M. Palladieva, Investigation of the Distribution of Gamma-Radiation from Co^{60} Sources of Different Geometric Shapes [in Russian] (All-Union Scientific Research Roentgen-Radiological Institute Press, Leningrad, 1957).
12. H. Fano, Nucleonics 11, 8 (1953); Nucleonics 11, 55 (1953).
13. G. White, Phys. Rev. 80 154 (1950).

*Original Russian pagination. See C. B. translation.

GENERAL RELATION FOR CRITICAL THERMAL LOADING

I. I. Novikov

Translated from Atomnaya Énergiya, Vol. 7, No. 3, pp. 252-253
September, 1959
Original article submitted July 10, 1959

Analysis of similar conditions involved in heat-transfer processes in various liquids shows that for complete equivalence of the heat-transfer processes it is necessary that these liquids: a) be thermodynamically alike (i.e., satisfy the identically applied conditions); b) be under corresponding conditions; and c) have equal values for the equivalent criteria which characterize the conditions existing at the liquid-solid boundary.

The requirement of thermodynamic equivalence is especially important in those cases where on the one hand, the condition parameters vary within wide limits, and on the other hand, a molecular mechanism for the effect appears more likely, undistorted by complex external conditions acting on the liquid. This applies to the boiling of a liquid, and particularly to the crisis arising during the changes involved in the boiling process.

It is not hard to show that the basic characteristic of the boiling crisis – the critical heat flow level (or the critical thermal loading) – must, in the case of a liquid boiling in a large volume, be expressible as a function of the following type:

$$q_c = \frac{g^{1/2} R^{1/2} p_c \; T_c^{1/2}}{\mu^{1/2}} f\left(\frac{p}{p_c}, \; \frac{V_c^{1/3}}{a}\right),$$

where R is the gas constant; μ is the molecular weight of the substance; p_c, V_c, and T_c are the critical parameters of the substance; a is the average radius of curvature of the heating surface irregularities; p/p_c is the applied pressure; f is a certain function which is identical for a group of thermodynamically equivalent substances.

The indicated relationship for q_c is obtained as follows. For thermodynamically equivalent substances, the ratio of the quantity of heat received in a given process by one mole of liquid to the absolute temperature of the liquid turns out to be a universal function of the applied parameters and of the physical characteristics of the process. The average size of vapor bubbles formed during boiling of the liquid appears to be such a characteristic; it is determined by the magnitude of the heating surface irregularities, so it follows that a factor $V_c^{1/3}/a$ is introduced into the process equation.

The expression for q_c can be shown in the form of a product of a dimensional factor times a dimensionless function of the reduced parameters (in this case it will be: either p/p_c or T/T_c) and the term $V_c^{1/3}/a$. The dimensional factor must consist of basic physical parameters of the given substance; namely, the critical parameters p_c, V_c, and T_c, which are the most important thermodynamic characteristics of the substance, expressing themselves in the general qualitative form as the effect of molecular forces and the molecular masses (i.e., the relation μ/g). Furthermore, the gas constant R may enter into the dimensional factor. Combining the quantities p_c, T_c, μ/g, and R in such a way as to obtain the dimensions of the thermal flux, we obtain the above expression for q_c.

It follows from this expression that for thermodynamically equivalent substances, boiling under identical conditions, and having equal (or close) values of V_c, the quantity $(q_c \; \mu^{1/2}) / (p_c \; T_c^{1/2})$ must be the same for equal values of p/p_c.

This result is in good agreement with experiment. The figure shows the dependence of the quantity $(q_c \; \mu^{1/2})/(p_c \; T_c^{1/2})$ on p/p_c for benzene and pentane.* Benzene and pentane have equal values of the critical coefficient $(R \; T_c)/(p_c \; V_c) = 3.76$, i.e., they are thermodynamically equivalent; their critical volumes V_c (256 and 310 cc/mole) are very close. As can be seen in the figure, the points for benzene and pentane lie on the same curve.

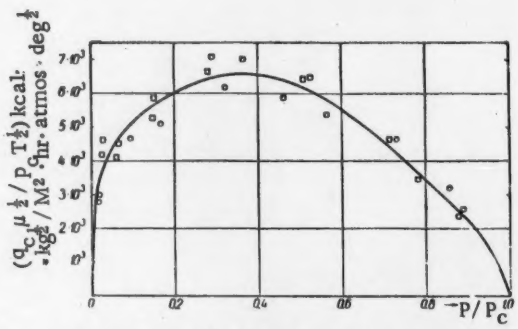

Curve showing equality of the values of $q_c \; \mu^{1/2} / p_c T_c^{1/2}$ with identical p/p_c values for the thermodynamically equivalent substances: O) benzene; □) pentane.

* The values for q_c were taken from the work of M. Cichelli and C. Bonilla, Trans. Am. Inst. Chem. Eng. 41, 745 (1946).

INFLUENCE OF AN INTERNAL HEAT SOURCE ON THE HEAT-TRANSFER COEFFICIENT

S. S. Kutateladze, N. I. Ivashchenko, and T. V. Zablotskaya

Translated from Atomnaya Énergiya, Vol. 7, No. 3, pp. 253-254
September, 1959
Original article submitted December 12, 1958

An internal heat source appears in a liquid flow carrying a radioactive suspension, in the flow of a radioactive solution, when electric current passes through a stream of liquid metal and in similar cases. Let us consider the influence of this source on the heat-transfer coefficient when a liquid flows in a cylindrical tube with a length sufficient for neglecting the inlet section effect.

We shall use the following notation:

t is the temperature;
R is the present radius;
R_0 is the tube radius;
x is the coordinate in the tube axis direction;
λ is the thermal conductivity coefficient;
a is the temperature conductivity coefficient;
w is the flow velocity;
q_v is the internal heat source density;
$v = (t_{tw} - t)/(t_{tw} - \bar{t})$ is the dimensionless temperature;
$Pe = 2W R_0 / a$ is the Peclet number;
$\bar{w}$ is the mean-discharge flow velocity;
$Nu = 2\alpha R_0 / \lambda$ is the Nusselt number;
$\bar{t}$ is the average flow temperature with respect to enthalpy in a given tube cross section;
t_{tw} is the tube wall temperature;
$\omega = w/\bar{w}$ is the dimensionless velocity;
$z = q_v R_0 / 2 q_{tw}$ is the relative heat source density;
$\xi = R/R_0$ is the relative radius;
α is the heat-transfer coefficient;
α_0 is the heat-transfer coefficient for $q_v = 0$;
q_{tw} is the heat flow through the tube walls;
$X = x/R_0$ is the relative axial distance.

After writing the heat propagation equation [1]

$$\frac{\partial}{\partial R}\left[\left(1+\frac{\lambda_T}{\lambda}\right) R \frac{\partial t}{\partial R}\right] + \frac{q_v R}{\lambda} = \frac{wR}{a}\frac{\partial t}{\partial x}, \quad (1)$$

we integrate this equation within the limits from 0 to R, assuming that $q_v = \text{const}$. After transformation into the dimensionless form, we obtain

$$v = -\frac{Pe}{2}\int_{\xi}^{1}\left[\frac{\int_0^{\xi}\omega\xi\frac{\partial v}{\partial x}d\xi}{\left(1+\frac{\lambda_T}{\lambda}\right)\xi}\right]d\xi - \frac{q_v R_0^2}{2\lambda(t_{tw}-\bar{t})}\int_0^{1}\frac{\xi d\xi}{1+\frac{\lambda_T}{\lambda}}. \quad (2)$$

As a first approximation, let us introduce in this expression, which is the average value with respect to the cross section, the value $\partial v / \partial X$.

By determining the mean-discharge temperature, we obtain

$$\bar{v} = 1 = 2\int_0^1 \omega\xi v d\xi. \quad (3)$$

By determining the heat-transfer coefficient from the usual equation

$$\alpha = \frac{q_{tw}}{t_{tw} - \bar{t}}, \quad (4)$$

we find that

$$\frac{1}{Nu} = 2\int_0^1 \omega\xi\left\{\int_{\xi}^{1}\left[\frac{\int_0^{\xi}\omega\xi d\xi}{\left(1+\frac{\lambda_T}{\lambda}\right)\xi}\right]d\xi\right\}d\xi + $$
$$+ Z\left(2\int_0^1 \omega\xi\left\{\int_{\xi}^{1}\left[\frac{\int_0^{\xi}\omega\xi d\xi}{\left(1+\frac{\lambda_T}{\lambda}\right)\xi}\right]d\xi\right\}d\xi - \right.$$
$$\left. - \int_0^1 \omega\xi\left(\int_{\xi}^{1}\frac{\xi d\xi}{1+\frac{\lambda_T}{\lambda}}\right)d\xi\right). \quad (5)$$

Thus, the degree of influence of an internal heat source is proportional to the difference

$$\Delta = \frac{2}{\xi}\int_0^{\xi}\omega\xi d\xi - \xi. \quad (6)$$

For $\omega = 1$, the difference (6) is equal to zero, i.e., in a flow with maximum turbulence the heat-transfer coefficient does not depend on the internal source density. For laminar flow, i.e., for a parabolic velocity distribution,

$$\frac{\alpha}{\alpha_0} = \frac{1}{1+0{,}272\,Z}. \quad (7)$$

For turbulent flow with the velocity distributed according to the 1/7 law and for Pr = 0,

$$\frac{\alpha}{\alpha_0}=\frac{1}{1+0{,}0834\ Z}. \qquad (8)$$

For $q_v = 0$, (5) becomes the Lyon integral ratio [2].

The figure shows the results of calculations where the above equations are used. It is obvious that the influence of an internal source on the heat-transfer coefficient is slight and that it becomes manifest for $\omega \neq 1$. Actually, if heat is supplied through the walls to a flow where heat is generated (Z > O), the layers with a lower velocity are heated more intensively. In this case, the temperature difference t_{tw} -t is greater than in thecase where $q_v = 0$. Consequently, the heat-transfer coefficient decreases with an increase in the source density. When a heat sink (Z < O) is present in the flow, the heat-transfer coefficient increases with an increase in the internal source density.

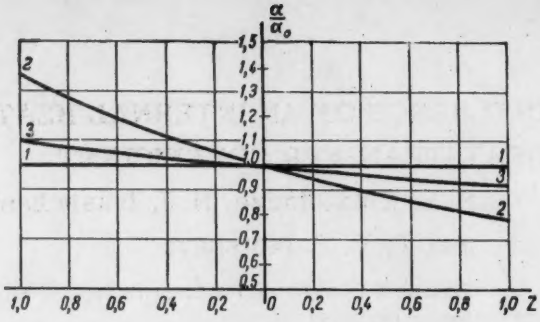

Influence of the internal heat source density on steady heat transfer in tubes. 1) Flow with maximum turbulence (ω=1); 2) laminar flow; 3) turbulent flow where the velocities are distributed according to the 1/7 law.

LITERATURE CITED

1. S. S. Kutateladze, Principles of the Heat-Transfer Theory [in Russian] (Mashgiz, Moscow, 1957).
2. R. Lyon, Chem. Eng. Progr. 47, 11 (1951).

HEAT TRANSFER IN TRANSVERSE FLOW OF MOLTEN SODIUM AROUND A SINGLE CYLINDER

A. A. Andreevskii

Translated from Atomnaya Énergiya, Vol. 7, No. 3, pp. 254-256
September, 1959
Original article submitted November 25, 1958.

The heat transfer in tubes in the transverse flow of liquid metals has been meagerly investigated. Some information on this problem can be found in [1-3]. After the present work was completed, [4 and 5] were published in which some experimental data on heat transfer in the flow of mercury around a group of tubes arranged in checkerboard order were given.

The device for investigating the heat transfer to sodium, which has been used in this work, consists of a closed heated circuit with forced liquid metal circulation. Due to the fact that the circuit was air-tight, it was possible to evacuate it and to fill it with an inert gas under a pressure of 0.1-0.2 atmos. Also, a bypass with a grid filter (10,000 meshes/cm^2) was provided in the circuit for the trapping of oxides.*

The working section of the device consisted of a rectangular box with an inlet step diffuser and an outlet convergent nozzle. The hydraulic characteristics of the working section inlet were investigated in special experiments which were performed with water. An electrocalorimeter, the frame of which consisted of a hollow Steel 20 cylinder with an outside diameter of 22 mm and a working length of 200 mm, was installed in the middle portion of the working section. A steel tube, which was insulated from the calorimeter by mica, served as the heater. In order to secure a uniform heat flow along the calorimeter circumference, special attention was paid to securing a uniform thickness of the mica insulation. The thermal load of the calorimeter surface under operating conditions was $7\text{-}9 \times 10^4$ kcal/m^2·hr, which guaranteed a reliable measurement of the basic quantity to be found – the temperature drop from the wall to the liquid. Six grooves (every 60°) were cut on the internal surface of the calorimeter frame for the placement of chromel-alumel thermocouples. The thermocouple hot-junctions were clamped under metallic blocks made of the same steel as the calorimeter frame. The thermocouple tips were located in the cross-sectional plane passing through the middle of the calorimeter, which permitted the simultaneous measurement of the heat transfer at six points along the calorimeter circumference.

An evaluation of errors showed that the maximum total measurement error arising in determining the heat-transfer coefficient did not exceed ±10%.

The presence of oxygen ($< 1.0 \times 10^{-2}$ %), iron ($< 5.6 \times 10^{-4}$%), and nickel ($< 4.1 \times 10^{-5}$%) in molten sodium was detected by chemical analysis.

The experiments were performed for sodium temperatures from 220 to 250° C, and the velocity interval from 0.1 to 0.4 m/sec, which corresponded to an interval of Reynolds numbers from 4000 to 20,000 and an interval of Peclet numbers from 25 to 125.† The obtained Nu=f (Pe) relation is shown in Fig. 1. This relation was obtained for $\varphi = 120°$ on the basis of readings of thermocouples Nos. 4 and 6, which were mutually symmetrical with respect to the flow axis.

A comparison of experimental data obtained for different angles, shows that the relations between the local heat transfer and the velocities at the front and the back cylinder regions are different.‡

In the back cylinder region (from $\varphi = 120$ to 180°), the relation between heat transfer and velocity is described by a logarithmic straight line with a slope close to 0.35. On the front cylinder surface ($\varphi = 0$ and 60°), the dependence of heat transfer on velocity has a more complex character. For Peclet numbers > 50, the experimental points are grouped around a curve with an exponent close to 0.5. In the interval of Peclet numbers from 40 to 50 (Pe ≃ 8000), the heat-transfer curve has a bend, and for Pe > 50, the heat-transfer coefficient depends only slightly on velocity. The causes of such a change in the character of heat transfer are not known at the present time. However, it can be assumed that the heat-transfer coefficient at the cylinder front zone is more sensitive to changes in flow conditions than the heat-transfer coefficient at the back zone.

---

* For more details, see [1 and 6].

† In calculating the Pe and Re numbers, the upstream flow velocity was taken for the determining velocity, and the cylinder diameter was taken for the determining dimension.

‡ For $\varphi = 60°$ as well as for $\varphi = 0°$, the line averaging the experimental points has a bend in the region of Peclet numbers from 40 to 50. The dependence of the heat transfer on velocity for $\varphi = 180°$ is similar to the lower line in Fig. 1.

The heat-transfer distribution around the cylinder perimeter is shown in Fig. 2. The points which were used in plotting the heat-transfer curves were obtained for the corresponding angle φ and Pe number (with respect to the averaging lines of initial Nu = f (Pe) curves for φ = const). It is obvious from the figure that the heat-transfer coefficient reaches its maximum value at the leading cylinder generatrix ($\varphi = 0°$). The heat-transfer minimum is observed in the trailing zone ($\varphi = 180°$).

In Fig. 3, the heat-transfer curves for sodium (Pr $\simeq$ 0.007) and air (Pr $\simeq$ 0.7) flow around a single cylinder are compared. The heat-transfer distribution curves for transverse flow of liquid metal around a bunch of tubes arranged in checkerboard order have a similar character [1, 3, and 4].

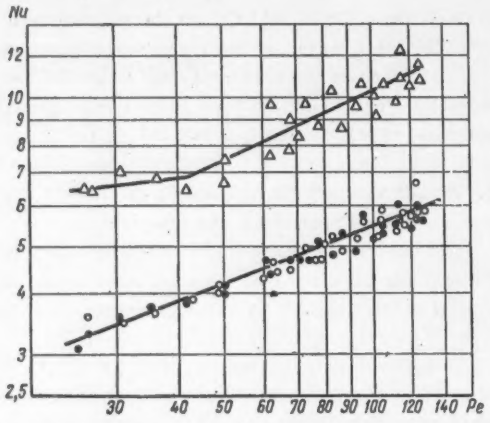

Fig. 1. Dependence of the local heat transfer on sodium velocity. Δ) Thermocouple No. 5 ($\varphi = 0°$); •) thermocouple No. 6 ($\varphi = 120°$); O) thermocouple No. 4 ($\varphi = 120°$).

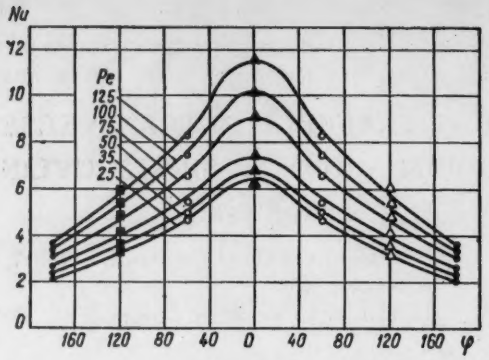

Fig. 2. Heat-transfer distribution along the perimeter of a single cylinder. Measurement points with thermocouples: O) No. 1; •) No. 3; Δ) No. 4; ▲) No. 5; ■) No. 6.

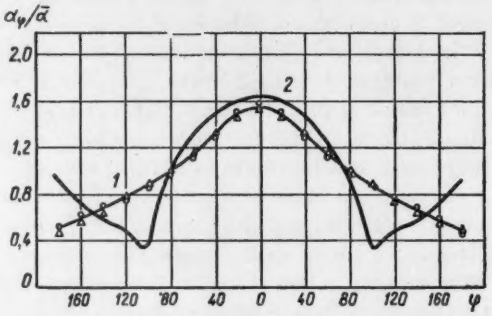

Fig. 3. Variation of the relative heat-transfer coefficient along the perimeter of a single cylinder. 1) Sodium (O-Pe = 0.25, Re = 4,000; Δ-Pe = 125, Re = 20,000); 2) air (Re = 16,000).

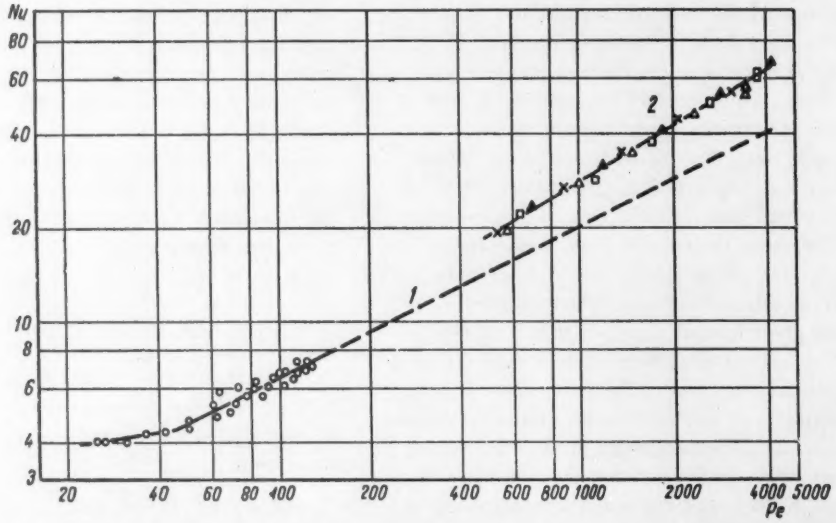

Fig. 4. Average heat transfer in transverse flow of liquid metal around a single cylinder and around a bunch of tubes arranged in checkerboard order. 1) Single cylinder in sodium flow (Pr = 0.007); 2) bunch of tubes (data from [5]): ▲) Pr = 0.0215; □) Pr = 0.0185; Δ) Pr = 0.0160; x) Pr = 0.0138.

The absence of a heat-transfer maximum in the trailing zone of a single cylinder and of tubes arranged in a bunch in transverse flow of liquid metal can be explained by a weaker hydrodynamic influence of the flow on heat transfer due to the high thermal conductivity of media with small Prandtl numbers.

The dependence of the average heat transfer of a single cylinder on liquid metal velocity is given in Fig. 4. in Nu vs. Pe coordinates. The obtained experimental data for the $50 \leq Pe \leq 125$ interval is well described by the dependence.

For the sake of comparison, Fig. 4. shows also the experimental data for mercury, which was obtained by Rickard, Dwyer and Dropkin.

It can be stated that a qualitative agreement exists between the results obtained in the present paper and the data from [5]. Actually, it is obvious from Fig. 4 that, in flow of liquid metal around a bunch of tubes as well as in the case where media with $Pr \simeq 1$ flow around tubes, a higher (by 20-40%) heat-transfer intesity is observed. The dependence of the heat-transfer coefficient on liquid metal flow velocity is stronger for a bunch of tubes (the exponent is ~ 0.6-0.65). In view of the fact that the results of the present investigation are confirmed by data from [5], the author considers that for the $50 \leq Pe \leq 5000$ interval, the heat transfer in flow of sodium and mercury around a single cylinder can be calculated according to the proposed equation until new data becomes available.

LITERATURE CITED

1. S. S. Kutateladze, V. M. Borishanskii, I. I. Novikov, and O. S. Fedynskii, Liquid-Metal Coolants [in Russian] (Atomizdat, Moscow, 1958) p. 114.
2. Nuclear Reactor Techniques [Russian translation] (IL, 1957) Vol. II, p. 218.
3. McLean, Lectures in Reactor Construction Techniques [Russian translation] (Sudpromgiz, Moscow, 1957).
4. R. Hoe, D. Dropkin and O. Dwyer. Trans. ASME 79, 899 (1957).
5. C. Richard, O. Dwyer, and D. Dropkin, Trans. ASME 80, 646 (1958).

GAMMA-RAY SPECTRUM OF THE IRT REACTOR

L. V. Groshev and A. M. Demidov

Translated from Atomnaya Énergiya, Vol. 7, No. 3, pp. 257-258
September, 1959
Original article submitted May 4, 1959

The spectrum of gammas emitted from the active zone of the IRT reactor, described in [1], via one of the horizontal channels of the reactor has been measured by means of a Compton electron magnetic spectrometer. The gamma spectrometer used in an earlier experiment [2] was employed in the measurements.

Results of the measurements may be seen in Fig. 1. The instrumental spectrum is presented there. It was obtained by subtracting from the measured coincidence spectrum (pair electrons for the given γ spectrum yield a very small contribution to the coincidence spectrum) the contribution from electrons of pairs dislodged with Compton-recoil electrons by γ rays from the radiator section of the spectrometer. Figure 2 gives the corrected gamma-ray spectrum. The value of $\nu(E\gamma)E\gamma$, where $\nu(E\gamma)$ is the number of γ quanta per unit energy interval, is plotted on the ordinate. The area of the spectral interval $[\nu(E\gamma)E\gamma]\cdot\Delta E\gamma$ is proportional to the energy carried off by γ rays having energies ranging from $E\gamma$ to $E\gamma + \Delta E\gamma$. In making the transition from the instrumental spectrum to the corrected spectrum, the spectral sensitivity of the instrument was taken into account, as well as γ-ray absorption in the passage of gamma quanta from the reactor core to the radiator of the spectrometer. In particular, traversal by γ rays of 8 meters of air and 9 cm of paraffin mixed with boron carbide was taken into account.

The general outline of the experiment is represented in the upper right-hand corner of Fig. 2. It is clear from the diagram that the γ rays emerging from the reactor core traverse ~ 10 cm of graphite, which surrounds the core. No correction was applied for possible absorption of γ rays by graphite in that layer. Absorption of γ rays in that layer brings about a sharp reduction in the γ spectrum at energies < 0.7 Mev.

The IRT reactor burns enriched uranium; the moderator is ordinary water, and the basic structural material is aluminum. γ lines due to neutron capture in aluminum ($E\gamma$ = 7.72 Mev, etc.), carbon ($E\gamma$ = 4.95 Mev), hydrogen ($E\gamma$ = 2.23 Mev) and γ lines of energies 1.78 Mev, associated with β decay of Al^{28}, may therefore be delineated with certainty in the γ spectrum of the reactor. At energies in the neighborhood of

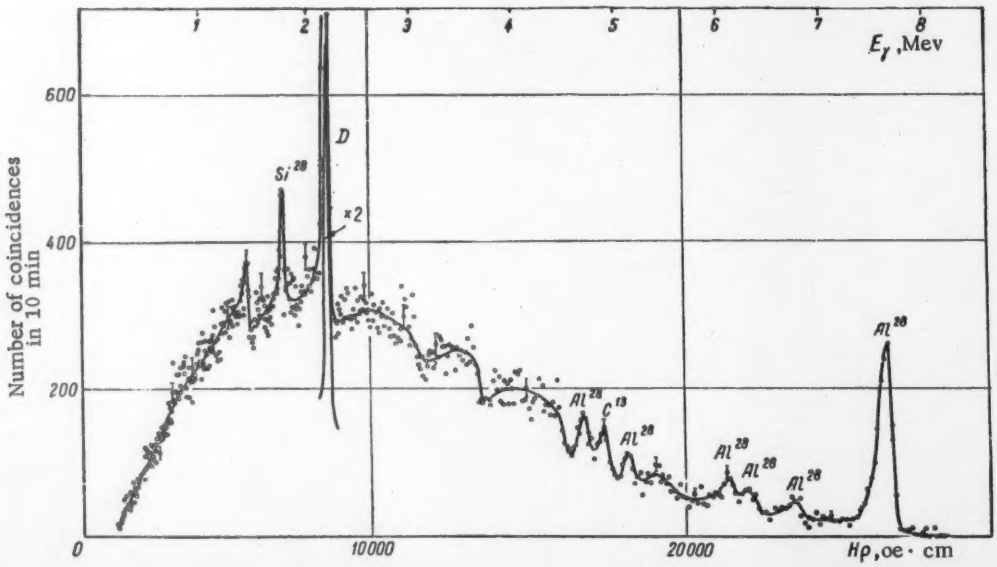

Fig. 1. Instrumental γ-ray spectrum for γ rays emitted from the core of the IRT reactor.

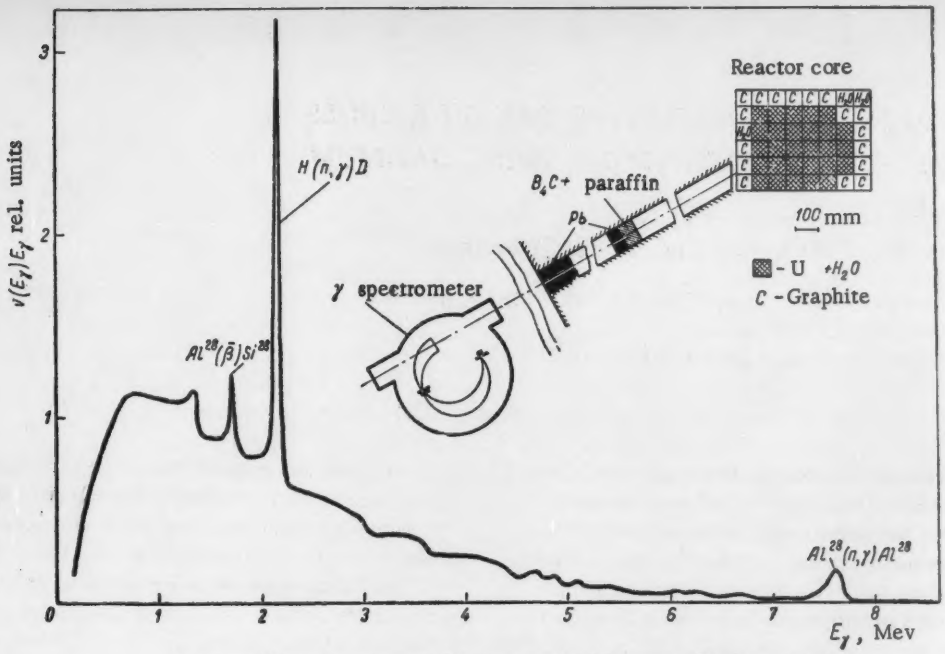

Fig. 2. Adjusted spectrum of γ rays emitted by core of IRT reactor.

1.4 Mev, a diffuse peak of uncertain origin appears. It might possibly be caused by γ rays emitted by radioactive elements which are fission products of uranium. The major portion of the unresolved part of the γ spectrum must be determined by γ rays originating in the reaction (n, γ) involving U^{238} and U^{235} (the binding energy of the last neutron in U^{239} and U^{236} is 4.63 Mev and 6.41 Mev, respectively), and by γ rays produced by fission.

Note the substantial difference in the γ-ray spectra of the RFT reactor [3] and the IRT reactor. Since the basic structural material used in the RFT reactor is stainless steel, the contrast between the γ-ray spectrum of this reactor and that of the IRT reactor is due to the strongly developed high-energy portion of the spectrum, due to neutron capture events in the iron, nickel and chromium present.

In the table below, we present relative values of $\int \nu(E\gamma)\, E\gamma\, dE\gamma$ found from Fig. 2, for various intervals in the spectrum. These values are cited separately for γ lines of energies 2.23, 1.78, and 7.72 Mev, while the value for the first γ line is taken equal to 100.

E_γ, Mev	0,2—0,5	0,5—1,0	1,0—2,0	1,78	2—3	2,23	3—4	4—5	5—6	6—7,5	7,72
$\int \nu(E_\gamma) E_\gamma dE_\gamma$, rel. units	130	300	530	12	360	100	200	105	37	25	22

In conclusion we should like to take this opportunity to express our gratitude to the staff which made possible the operation of the IRT reactor during the measurements.

LITERATURE CITED

1. V. V. Goncharov, E. N. Babulevich, Yu. G. Nikolaev and Yu. F. Chernilin, Report No. 2185, Presented at the Second International Conference on the Peaceful Uses of Atomic Energy, (Geneva, 1958).
2. L. V. Groshev, B. I. Gavrilov, and A. M. Demidov, Atomnaya Énergiya 6, 281 (1959)*
3. L. V. Groshev, B. P. Ad'yasevich, and A. M. Demidov, Report No. 651, Geneva Conference, (1955).

*Original Russian pagination. See C. B. translation.

MEASUREMENT OF RADIATIVE CAPTURE CROSS SECTIONS OF FAST NEUTRONS, USING GALLIUM ISOTOPES

Yu. Ya. Stavisskii and V. A. Tolstikov

Translated from Atomnaya Énergiya, Vol. 7, No. 3, p. 259
September, 1959
Original article submitted March 26, 1959

The variation in the radiative capture cross sections for neutrons reacting with gallium isotopes was measured by comparison with the variation observed in the cross section of the nuclide I^{127}, used as a reference standard. Samples of the test isotope and of the standard were irradiated simultaneously while exposed to the same fast neutron flux. The β activity induced in the samples was measured by end-window counters. After a drop in activity, the samples were irradiated in a uniform flux of thermal neutrons, and the induced activity was measured using the same counters.

If the time of irradiation, fluorescent lifetime, and measurement interval are kept constant for each sample during irradiation by fast and thermal neutrons, the capture cross section may be determined from the relation

$$\sigma_x(n,\gamma)=K\frac{\sigma_x^{th}}{\sigma_{st}^{th}}\sigma_{st}^{f}=\frac{\frac{A_x^f}{A_{st}^f}\sigma_x^{th}}{\frac{A_x^{th}}{A_{st}^{th}}\sigma_{st}^{th}}\sigma_{st}^{f},$$

where (A_x^{th}/A_{st}^{f}), (A_x^{th}/A_{st}^{th}) are the activity ratios of the test and of the standard samples exposed to thermal and fast neutron fluxes; σ_{st}^{f}, σ_{st}^{th} are the capture cross sections of fast and thermal neutrons of the standard; σ_x^{th} is the capture cross section of thermal neutrons of the nuclide under investigation.

A fast neutron source was provided by the reaction T (p, n)He^3, which was brought about using a Van de Graaf accelerator. Over the 200-1,400 kev energy range, the energy spread of the neutrons amounted to ± 30 kev, while it amounted to ± 50 kev over the 1,400-2,000 kev range. Irradiation by thermal neutrons took place in the thermal channel of the fast neutron experimental reactor. In order to eliminate resonance and fast neutron effects, recourse was had to the cadmium-difference measurement technique.

In the calculations, the capture cross sections for thermal neutrons by nuclides I^{127}, Ga^{69} and Ga^{71} were taken to be 5.6 ± 0.3, 1.4 ± 0.3 and 4.0 ± 0.7 barns, respectively [1]. The capture cross sections for fast neutrons by I^{127} were taken from [2]. The mean standard deviation of the experimentally measured values of K did not exceed 3-4%. The results of the measurements are plotted on the accompanying diagram. The radiative capture cross section for Ga^{69} reveals a smooth energy dependence, while that of Ga^{71} manifests a sharp drop in the region ~ 550 kev. It is evident that

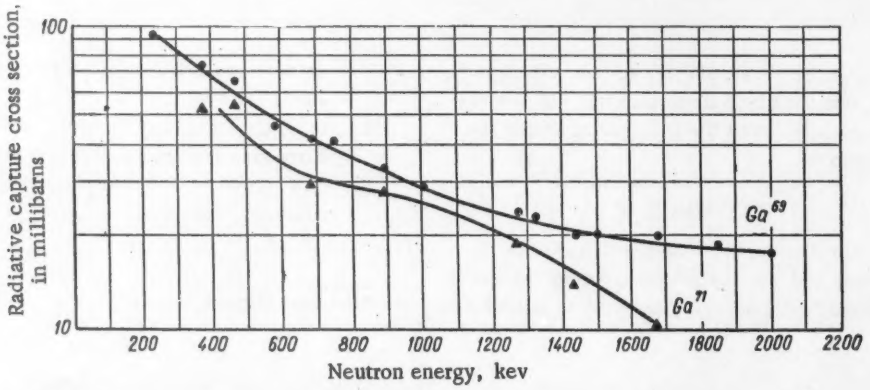

Variation in the radiative capture cross sections of fast neutrons reacting with gallium nuclides, as a function of neutron energy.

this effect is due to the presence of inelastic scattering of neutrons from Ga^{71} at energy levels ranging from 510 to 610 kev [3]. The competition introduced by the inelastic scattering leads to a fall-off in the radiative capture cross section graph.

The authors would like to express their gratitude to A. I. Baryshnikov, V. I. Zotova, and V. G. Nedopekin, for their kind assistance in the execution of this research effort.

LITERATURE CITED

1. D. Hughes and R. Schwartz, Neutron Cross Sections (McGraw-Hill, New York, 1958).
2. H. Martin and R. Tascheck, Phys. Rev. 89, 1302 (1953).
3. B. S. Dzhelepov and L. K. Peker, Decay Schemes of Radioactive Nuclei [in Russian] (Izd. AN SSSR, Moscow, 1958) p. 166.

CASCADE γ TRANSITIONS IN Cl^{36} ACCOMPANYING THERMAL NEUTRON CAPTURE

V. P. Burmistrov

Translated from Atomnaya Énergiya, Vol. 7, No. 3, pp. 260-262
September, 1959
Original article submitted November 1, 1958

This study of γ emission arising in the capture of the thermal neutrons by chlorides was performed on a beam from the reactor of the First Atomic Power Station [1]. The chloride specimen consisted of chemically pure $PbCl_2$ powder. Scintillation counters were placed at right angles to each other and to the thermal neutron beam. A layer of boron carbide, 3 mg/cm^2 thick, was placed between the crystals and the target, to absorb any thermal neutrons scattered by the target. NAI(Tl) crystals (Ø 30, h = 20 mm, and Ø 40, h = 50 mm) were combined with an RCA - 5819 type photomultiplier tube. The pulses of the channel to be analyzed were directed to a 100-channel pulse analyzer, described in [2], and the pulses of the control channel were fed to a differential discriminator. The pulses of both channels were fed in parallel to a fast coincidence circuit having a resolving time $\tau = 0.8 \cdot 10^{-7}$ sec. The value of the resolving time was secured by the absence of true coincidence losses.

The required amplitude interval is delineated by the discriminator circuit in which the slow coincidence circuit ($\tau = 10^{-6}$ sec) is to be found, and in the presence of a pulse originating in the fast coincidence circuit, the pulse of the control channel gates the analyzer input. The pulse-height spectrum recorded by the pulse analyzer must therefore contain peaks corresponding to the γ photons emitted simultaneously with the γ photons recorded in the control channel.

In order to break the complex spectra down into their components, graphs were plotted of the shape of lines from γ sources with monochromatic energies in the range 0.128-2.76 Mev, for a crystal 30 mm in diameter and 20 mm in height. The absolute efficiency (ratio of area under the total absorption peak to absolute number of γ quanta from the source) as a function of the energy of the γ quanta in the energy interval 0.08-2.76 Mev was determined for the same crystal. The absolute activity of the sources was determined by the γ-γ coincidence method in an energetic analysis of coincident γ photons.

The spectrum of random coincidences was computed on the basis of the formula

$$N_{ran}(E) = 2\tau N_1 N_2(E),$$

where τ is the resolving time of the fast coincidence circuit, N_1 is the speed of light in the control channel, being a constant magnitude for the measurement in question, and $N_2(E)$ is the speed of light in the channel being analyzed, this speed being taken from the coincidence-less spectrum. Preliminary measurements showed that the random-coincidence spectrum calculated on the basis of the above formula is in close agreement with the spectrum measured while introducing into one of the channels, a large delay, sufficient to eliminate true coincidences.

The background of random coincidences remained below the 5% level in the measured coincidences in all regions of the spectrum (with the exception of the region of energies lying below 511 kev).

In addition to random coincidences, spurious coincidences were also taken into account, these being due to the following causal phenomena: 1) Compton scattering of γ photons from one crystal into another; 2) impingement on a crystal in the test channel of annihilation γ radiation accompanying the formation of an electron-positron pair in the crystal in the control channel; 3) the contribution to the pulse spectrum of pulses singled out by the window of the differential discriminator of the Compton distribution attributable to γ rays of greater hardness.

For each fixed amplitude interval selected in the control channel, the coincidence spectrum from the test channel was investigated by several different approaches, by measurement of the gain factor of the corresponding amplifier. The coincidence spectra so obtained were corrected for random coincidences and were then plotted on a common graph, after reduction to constant conditions. Points indicated by similar markings on the accompanying graphs represent measurements carried out with gain factor fixed. The time of measurement (5-40 hr) was chosen such that the number of true coincidences in the peaks would not be less than 100 pulses per channel. Where gain instability in any channel was found to exceed 1%, that measurement was rejected.

The diagram shows the spectra of γ photons emitted simultaneously with hard gammas. Diagram a depicts

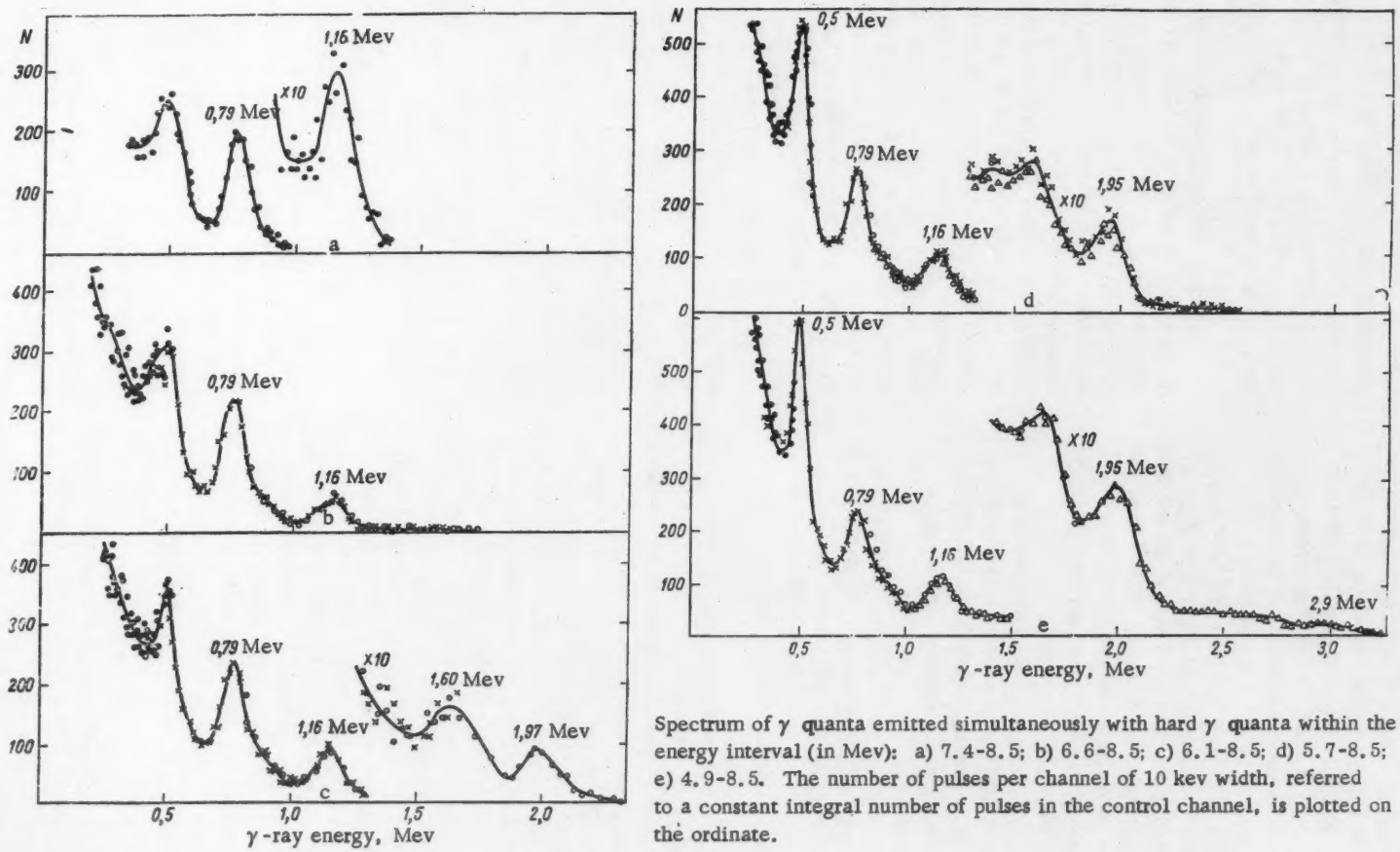

Spectrum of γ quanta emitted simultaneously with hard γ quanta within the energy interval (in Mev): a) 7.4-8.5; b) 6.6-8.5; c) 6.1-8.5; d) 5.7-8.5; e) 4.9-8.5. The number of pulses per channel of 10 kev width, referred to a constant integral number of pulses in the control channel, is plotted on the ordinate.

a spectrum of gamma photons emitted simultaneously with γ photons in the energy interval 7.4-8.5 Mev. The control channel was then used to select out γ photons having energies of 8.58 and 7.79 Mev. Furthermore, due to the statistical dispersion, pulses stemming from the photopeak of γ rays having an energy of 7.42 Mev can fall into the control channel. A peak corresponding to the energy 0.79 Mev stands out sharply in the spectrum, and a weaker peak at 1.16 Mev is also visible. This implies cascades of γ rays, 7.79-0.79 and 7.42-1.16 Mev. As we see from diagram (a), the γ line of energy 735 kev, reported in [3], does not appear in the spectrum. The shape of the photopeak at energy 790 kev shows that if there were γ rays present with energy 735 kev, the intensity of these latter photons does not comprise 10% of the intensity of the 790 kev line.

At energy ~ 0.5 Mev, a peak appears which is an instrumental artifact resulting from a pair effect in the crystal of the control channel when the crystal in the test channel was impinged upon by one of the annihilation quanta.

If γ rays with energies of 0.79 and 1.16 Mev are emitted in a cascade by γ rays with energies of 7.79 and 7.42 Mev, respectively, the ratio of their intensities in the coincidence spectrum must be equal to the ratio of the intensities of hard γ photons in the control channel.

Using as point of departure the ratio reported in [4] for the intensities of the γ lines emitted by Cl^{36}_{17} the ratio of the γ-line intensities in the control channel (taking line shapes into account) in the energy interval 6.6-8.5 Mev (see diagram b), $I_{7.79}/I_{7.74} = 2.5$. From the spectrum shown in diagram b, we find that $I_{0.79}/I_{1.16} = 2.6 \pm 1$. The numerical agreement confirms the assumption made in [4] to the effect that cascades 7.79-0.79 Mev and 7.42-1.16 Mev take place and proceed with no branching off through the 0.79 and 1.16 Mev levels, respectively. The spectrum over the energy interval 6.1-8.5 Mev (see diagram c) shows a photopeak appearing in the control channel, and the beginning of a Compton peak due to γ lines of 6.96 Mev energy, with a gentle shoulder corresponding to the 1.60 Mev γ line showing up in the spectrum of the test channel in the region of 1.60 Mev, the 1.60 γ line presumably [3-5] being found in the cascade with the γ quantum of energy 6.99 Mev. In this region of energies, the control channel also embraces a portion of the spectrum of pulses belonging to the γ line of energy 6.64 Mev; a γ line of energy 1.95 Mev appears correspondingly in the test channel spectrum which serves to confirm the 6.64-1.95 Mev cascade.

It was found from the coincidence spectrum of the channel that $I_{1.6}/I_{1.95} = 0.18 \pm 0.07$, while the ratio of intensities of hard lines, [4], with energies 6.99 Mev and 6.64 Mev found to accompany them in the cascade (with the contribution to the control window taken into account), must be $I_{6.99}/I_{6.64} = 0.13 \pm 0.02$. The numerical agreement in intensities confirms the presence of the 6.99-1.60 and 6.64-1.95 Mev cascades.

When the threshold of the control channel is set at the position corresponding to energy 5.7 Mev (see diagram d), pulses corresponding to an energy of 6.11 Mev also enter the channel. As is evident, this brings about a sharp increase in the peak in the energy region of 0.5 Mev, which may be due solely to the appearance of true coincidences of γ quanta with energies of 6.11 and 0.5 Mev.

Assuming that the contribution of the instrumental spurious peak at energy 0.51 Mev did not change, we find that half of the area included in this photopeak is due to the appearance of γ quanta having energies of 0.5 Mev. This fits well with the existence of the complex cascade 6.11-0.51-0.790-1.16 Mev [4]. Earlier, as the width of the control channel was increased, the appearance of a new γ line in the test channel took place because of a decrease in the total intensity of the γ lines, which were already present in the spectrum. In the case in point, the transition from the energy region of 6.1-8.5 Mev (see diagram c) to the region of energies 5.7-8.5 Mev (see diagram d) does not result in a decrease of the total intensity of the γ lines having energies 0.79, 1.16, 1.60 and 1.95 Mev. This being so, a decrease, due to the appearance of a new γ line of energy 0.51 Mev, in the total intensity of the γ lines alluded to above is offset by the appearance, as suggested in [4], of γ lines coinciding with it, and having energies of 0.79 and 1.16 Mev.

In the transition to the next lower level at 4.9 Mev (see diagram e), pulses belonging to energies of 5.72 and 5.50 Mev also arrive in the control channel. The contribution attributable to γ rays of energy 5.50 Mev may be neglected. In that case, a γ line of energy 2.9 ± 0.1 Mev will appear in the test channel spectrum. Its appearance is associated with the appearance of the 5.72 Mev γ line. These γ lines are obviously found in the cascade.

The measurements reported here, as well as the investigations of coincidence spectra with γ lines at 0.79, 1.16, and 1.95 Mev, permit us to draw the following conclusions:

1. There exist cascades corresponding to 7.79-0.79 and 7.42-1.16 Mev. Their intensities are interrelated as 7.8 : 14, and the intensities of the cascades 6.99-1.60 Mev and 6.64-1.95 Mev are in turn related as 1.9 : 14.4, in agreement with the supposition advanced in [4].

2. Cascades corresponding to 5.72-2.88 and 6.11-0.51-0.79-1.16 Mev take place. The last-mentioned cascade is confirmed by the fact of coincidences of γ quanta corresponding to 0.79-6.11 and 1.16-6.11 Mev. This last cascade actually passes through the 1.95 Mev level, which is borne out by the coincidence of γ quanta having energies 1.95 and 6.1 Mev. The coincidences of γ quanta having ener-

gies 1.16 and 6.64 Mev would indicate that, starting with the 1.95 Mev, a transition is possible not only to the ground state, but that even a transition through the 0.79 Mev level or through the 1.16 Mev level is possible.

The cascading transitions obtained show complete agreement with the scheme of γ transitions compiled in [4].

In conclusion, the author would like to take this opportunity to express his gratitude to Doctor of Physical and Mathematical Sciences A. K. Krasin for his kind and unflagging interest, valuable comments, and cooperation in carrying out the research, and to V. P. Radchenko for assistance kindly rendered in performing the necessary measurements.

LITERATURE CITED

1. D. I. Blokhintsev, N. A. Dollezhal' and A. K. Krasin, Atomnaya Énergiya No. 1, 10 (1956).*
2. L. A. Matalin, A. M. Shimanskii and S. I. Chubarov, Pribory i Tekh. Éksp. No. 1, 64 (1957).
3. A. Recksiedler and B. Hamermesh, Phys. Rev. 96, 109 (1954).
4. L. V. Groshev, A. M. Demidov, V. N. Lutsenko, and V. I. Pelekhov, Atlas of γ-Ray Spectra for Thermal Neutron Radiative Capture [in Russian] (Atomizdat, Moscow, 1958).
5. P. Endt and C. Braams, Rev. Mod. Phys. 29, 683 (1957).

*Original Russian pagination. See C. B. translation.

A LARGE ALPHA SPECTROMETER*

S. M. Baranov, A. G. Zelenkov, G. Ya. Shchepkin
V. V. Beruchko and A. F. Malov

Translated from Atomnaya Énergiya, Vol. 7, No. 3, pp. 262-264
September, 1959
Original article submitted May 8, 1959

The fundamental method used in the direct study of the fine structure of α decay still remains the measurement of the spectra of α particles by means of magnetic spectrometers. The most promising spectrometers are those incorporating spatial focusing in an inhomogeneous axisymmetric magnetic field [1-3]. Two existing α spectrometers of that type are known: one which focuses α particles at an angle of $\pi\sqrt{2}$ [4], and one which focuses alphas at an angle of 180°, using the fringe effect [5]. The first variant was selected by the authors in elaborating the design of our own α spectrometer.

The principal drawback in the instruments referred to is the rather small aperture (product of solid angle by source area). With a view toward improving this feature while retaining the high resolution of the spectrometer, the radius of the instrument's central orbit was relatively enlarged (ρ_0 = 155 cm).

Figure 1 shows a photograph of the α spectrometer so described. Its principal details are the magnet with field coils and the vacuum chamber of nonmagnetic stainless steel. The magnet enclosure is devised in the form of a double mushroom-shaped assembly consisting of three parts: the core, the cylindrical shell, and two "hats". The width of the pole pieces is ~ 70 cm, and the pole gap is 35 cm. The magnet parts are made to relatively high tolerances (0.2 mm). Specially machined cover plates dimensioned to analytically computed specifications are fitted to the pole pieces. The total weight of the facility runs to ~ 90 tons. The chamber volume is ~ 1000 liters. The chamber is pumped out by a high-vacuum VA-54 assembly and a forevacuum pump of the VN-2 type. The extent of evacuation of the vacuum chamber reaches several units of 10^{-6} mm Hg.

Sources of α-radioactive isotopes are placed in a special device, making it possible to perform alternate exposures of four targets without jeopardizing the vacuum. The maximum size of usable alpha sources is 100 × 10 mm.

*Submitted at the Ninth All-Union Congress on Nuclear Spectroscopy (Khar'kov, January, 1959).

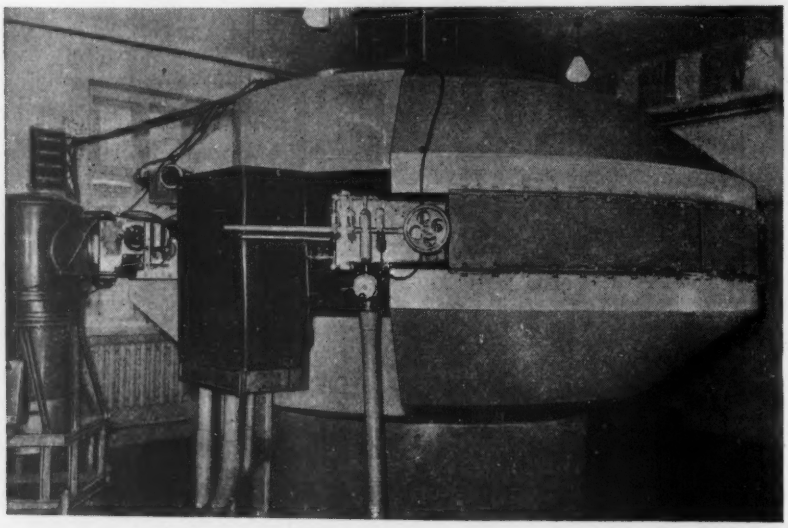

Fig. 1. General view of the alpha spectrometer.

Alphas emitted are recorded by a proportional counter or by thick-layered phtographic plates. A set of plates 500 mm long and 90 mm thick may be exposed simultaneously. The plates are placed in a special receptacle which may be used to permit the successive exposure of four sets of plates. Replacing of one set of plates by another and closing the receptacle is accomplished without affecting the vacuum.

The magnet winding is fed via a selenium rectifier hooked up to a three-phase bridge circuit. The voltage across the rectifier is supplied from a synchronous motor-generator operating on alternating current at a 35 kva power rating, and passes through a DN-35 saturation choke coil. The current is 700-1300 amp over the operational range of the instrument, which corresponds to a magnetic field intensity of 2.0-3.5 koe.

The basic circuit arrangement found in [6] is employed to stabilize the magnetic field. A 5LO-38 type CRT placed between two fixed "reference" magnets is utilized as a component,sensing variations in magnetic field intensity. This system is located in the scattered magnetic field of the spectrometer.

In the case of spectrographic measurements, the peak deviation of the magnetic field from a given value H_0 did not exceed $2 \cdot 10^{-4}$ in 8 hr of continuous operation of the instrument. Measurement of the value of the magnetic field intensity is based on the phenomenon of proton paramagnetic resonance. The measuring device enables determinations to be made of the value of the magnetic field over the effective operational range, to an accuracy of $\leq 1 \cdot 10^{-5}$.

Much attention has been devoted to obtaining the required field distribution in the magnet pole gap, and to a study of its topography. In particular, measurements were performed on the azimuthal symmetry of the magnetic field distribution, and the position of the median surface was also ascertained. An analysis of the measurements showed that azimuthal distortions and deviations of the median surface from the midplane within the effective volume remained within permissible limits. To remove the fringe effect, we used special magnetic shims which functioned as magnetic potential dividers [7]. These were a set of iron strips between which slabs of cardboard were sandwiched. The arrangement of these strips along the vertical was arrived at by experimental trial and error. Assemblies containing sets of the strips were positioned over the entire length along the inner and outer boundaries of the pole gap. The use of the shims enabled us to secure a somewhat improved field distribution over the entire volume.

Determination of the topography made it possible to select the proper geometry of the diaphragms collimating the beam of α particles, and to ascertain the maximum solid angle of the instrument ($8 \cdot 10^{-4} \times 4\pi$).

Investigations of the ion optical properties of the instrument enabled us to find the position of the focal plane, and to carry out a calibration of the spectrograph with respect to energies. The energy range of the α particles recorded simultaneously in the photographic plates proved to be equal to $\Delta E/E = 10\%$. The half-width $\Delta H\rho/H\rho$ of the line in that range did not exceed several hundredths of a percent. The dispersion of the instrument was close to predicted values, being $\Delta E/\Delta x = 2.3 \cdot 10^{-4}$ per mm, which corresponds to 1.2 kev/mm for an α particle emitted by Po^{210}.

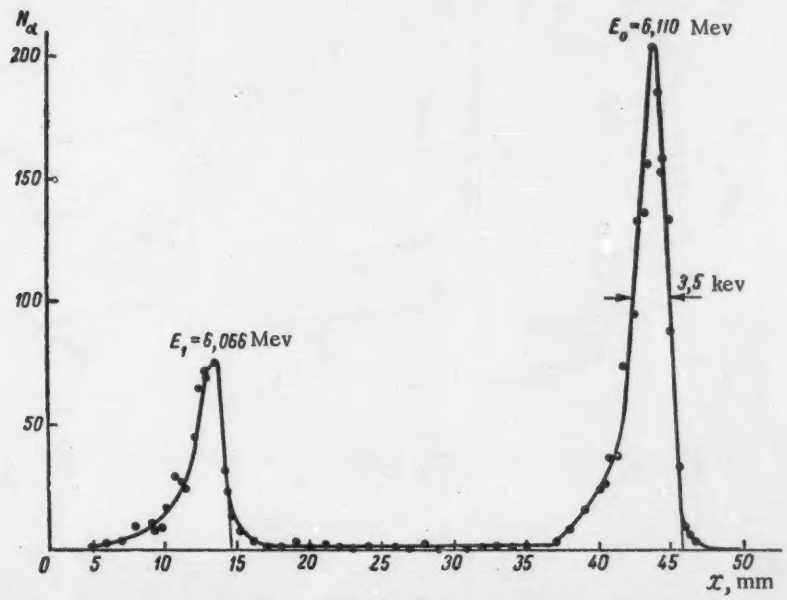

Fig. 2. Fundamental groups of α particles of Cm^{242}.

The relative variation in the transmission of the instrument along the focal plane was also measured; it turned out that it had a peak value (100%) for particles moving along the central orbit, and then fell of smoothly toward the edges of the focal plane, reaching a minimum value (80%).

The instrumental resolving power is illustrated in Fig. 2, on which we see plotted the results of measurements of the fundamental groups of α particles of Cm^{242}. The half-width of the line is 3.5 kev ($\Delta H\rho/H\rho = 0.028\%$). The instrument is capable of handling samples weighing up to 100 μg, for the study of groups of α particles having partial periods extending to $2 \cdot 10^{10}$ years, with a comparatively high resolving power.

A more fully detailed article decoted to this large alpha spectrometer will be printed in the Bulletin of the Academy of Sciences of the USSR.†

LITERATURE CITED

1. N. Svartholm and K. Siegbahn, Arkiv mat. astron. fysik. 33A, 21 (1946).
2. N. Svartholm, Arkiv mat. astron. fysik. 33A, 24 (1946).
3. K. Siegbahn and N. Svartholm, Nature 157, 872 (1946).
4. L. L. Gol'din, G. I. Novikova and E. F. Tret'yakov; Session of the Academy of Sciences of the USSR on the Peaceful Uses of Atomic Energy (Panel of the Division of Physical and Mathematical Sciences) [in Russian] (Academy of Sciences Press, Moscow, 1955) p. 266.
5. D. Judd and S. Bludmann, Nuclear Instr. 1, 46 (1957).
6. V. V. Zhukov and N. N. Semashko, Pribory i Tekh. Éksp. 2, 41 (1958).
7. F. Hinman and F. Crane, Rev. Sci. Instr. 23, 438 (1952).

† [Ivest. Akad. Nauk SSSR, 23, 12, 1402 (1959)]

FINDING THE OPTIMUM GEOMETRY OF A SHIELDING BARRIER

L. P. Kimel'

Translated from Atomnaya Énergiya, Vol. 7, No. 3, pp. 265-266
September, 1959
Original article submitted January 24, 1959

One of the most important problems in nuclear power engineering is the reduction of weight going into shielding. The design of a minimum-weight shielding depends on many factors [1]. Without proceeding into an analysis of all of these factors, let us merely indicate that the geometry of the radiation shielding barrier plays a role not to be underestimated in achieving optimum weight design. The tolerable radiation levels may be different at different points in space, and the shielding thickness may, in consequence of that, be a variable quantity, but one such that will assure the maintenance of a specified level of radiation at that particular point in space.

The solution of the problem of the optimum radiation shielding geometry in the general form for radiation sources which are complex in composition and shape involves formidable mathematical difficulties. For isotropic sources of simple geometry (e.g. linear, disk, cylindrical-surface or spherical-surface geometries), the solution of the variational problem may be used to derive an equation describing the optimum-weight shielding geometry.

Consider the problem of determining the geometry of a radiation shield of optimum weight for a linear source extending 2L in length and having an activity M (mg-equiv Ra) uniformly distributed along the length of the source (Fig. 1).

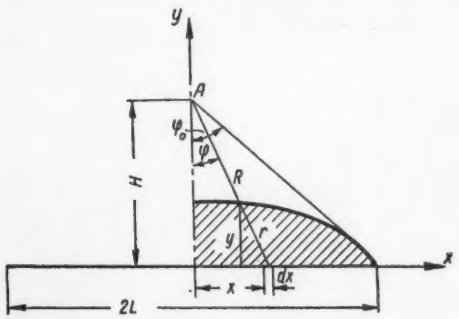

Fig. 1. Geometric representation for design purposes.

The dose rate at point A, without taking multiple scattering within the shield itself into account, is determined from the equation

$$P=2\int_0^L \frac{MK}{2LR^2}\,e^{-\mu r}dx=\int_0^{\varphi_0}\frac{MK}{LH}\,e^{-\mu y\sec\varphi}\,d\varphi, \quad (1)$$

where μ is the linear attenuation coefficient in the shielding material (for a narrow beam); M/2L is the specific activity of the source; K is a proportionality factor; φ_0 is arctan L/H.

The weight of the shielding barrier is

$$G=\rho V=\rho St=\int_0^L 2\rho t y\,dx=\int_0^{\varphi_0}2\rho t y H\sec^2\varphi\,d\varphi, \quad (2)$$

where ρ is the density of the shielding material, and t is the transverse dimension of the barrier.

It is imperative to find the geometry of a shielding barrier, i.e., y = f(x) or r = f(φ) under the condition where the dose rate at point A is of some specified value. The geometry must be such that the weight of the radiation shielding will be at a minimum. This is a variational problem having a conditional extremum [2].

We now find the minimum of the functional

$$G=\int_0^{\varphi_0}2\rho t y H\sec^2\varphi\,d\varphi$$

for the isoperimetric condition

$$\int_0^{\varphi_0}\frac{MK}{LH}\,e^{-\mu y\sec\varphi}\,d\varphi=P_0, \quad (3)$$

where P_0 is some specified value of the dose rate at point A.

The solution of such problems will be aided by setting up the auxiliary functional

$$G^{**}=\int_0^{\varphi_0}\left(2\rho t y H\sec^2\varphi+\lambda\frac{MK}{LH}\,e^{-\mu y\sec\varphi}\right)d\varphi,$$

where λ is the Lagrangian constant multiplier. The functional G^{**} is studied on the minimum by means of the usual methods of the variational calculus, i.e., by the solution of Euler's equation

$$Fy - \frac{d}{dx} Fy' = 0,$$

where F stands for the integrand.

In our case, the function is not dependent on $\underline{y}$, and, accordingly,

$$Fy = O,$$

i.e.,

$$2\rho t H \sec^2 \varphi - \frac{\lambda MK}{LH} \mu \sec \varphi e^{-\mu y \sec \varphi} = 0. \qquad (4)$$

From (4), we may determine $\underline{y}$:

$$y = \frac{1}{\mu \sec \varphi} \ln \frac{\lambda MK\mu}{2\rho t L H^2 \sec \varphi}. \qquad (5)$$

To determine λ, we substitute (5) into (3):

$$P_0 = \int_0^{\varphi_0} \frac{MK}{LH} e^{\ln 2\rho t L H^2 + \ln \sec \varphi - \ln \lambda MK\mu} d\varphi,$$

so that

$$\lambda = \frac{2\rho t H}{\mu P_0} \ln \frac{1+\sin \varphi_0}{\cos \varphi_0}.$$

Finally, we have

$$\left.\begin{aligned} y &= \frac{\cos \varphi}{\mu} \ln \left[\frac{MK \cos \varphi}{LHP_0} \ln \frac{1+\sin \varphi_0}{\cos \varphi_0} \right]; \\ r &= \frac{1}{\mu} \ln \left[\frac{MK \cos \varphi}{LHP_0} \ln \frac{1+\sin \varphi_0}{\cos \varphi_0} \right]. \end{aligned}\right\} \qquad (6)$$

We thus obtain the equation $r = f(\varphi)$ describing the shape of the radiation shield having optimum-weight characteristics. The curve arrived at is seen in Fig. 2. Similar reasoning is used to solve the problem of a disk-shaped radiation source.

The equation (6) derived for the geometry of the radiation shielding barrier fails to take into account multiple scattering within the shielding. The variation in shielding thickness due to multiple scattering effects may be taken into account by what is known as the method of successive (iterated) approximations [3] for values of $\underline{r}$ found by means of (6).

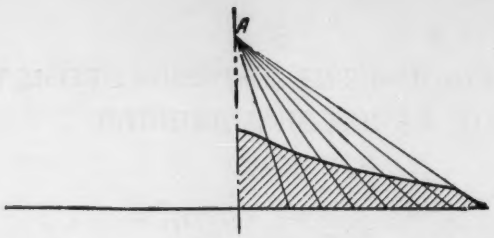

Fig. 2. Geometry of optimum-weight radiation shield.

It must also be noted that the variation in the dose rate at the point in question due to scattered radiation (e.g., scattered in air) is not taken into account in the calculations. The contribution of scattered radiation to the dose rate for a radiation shielding geometry such as described by (6) will obviously be larger than that for a radiation shield of constant thickness.

The experiments which we performed using a linear Co^{60} source, 1 meter in length showed that, with the shielding geometry calculated on the basis of (6), the measured dose rate agrees, within the limits of experimental error, with the dose rate specified for this design, and that the weight of the shielding barrier is 20% less than that designed on the basis of multiple attenuations.

LITERATURE CITED

1. E. P. Blizard, "Shield optimization with respect to weight," USAEC Reactor Handbook. Physics (McGraw-Hill, N. Y., 1955) Vol. 1, p. 709
2. L. E. El'sgol'ts, The Calculus of Variations [in Russian] (Moscow-Leningrad, Gostekhizdat, 1952).
3. Materials of the USAEC. Reactor Shielding Design Manual.

ANGULAR DISTRIBUTION OF RADIATION EMITTED BY Au^{198}, SCATTERED IN THE AIR ABOVE THE EARTH

V. N. Sakharov, V. I. Kolesnikov-Svinarev,
V. A. Nazarenko, and E. I. Zabidarov

Translated from Atomnaya Énergiya, Vol. 7, No. 3, pp. 266-267
September, 1959
Original article submitted February 18, 1959

In the work discussed below, an experimental material was produced which may prove of value in the design of shielding against γ radiation, and in calculations of multiple scattering of γ photons.

The total radiation intensity at distances up to 600 m removed from the source (r), and the angular distribution of radiation at distances of 150, 250, and 400 m were derived in the course of the work. Measurements were carried out with the source and detector placed at a height of 1.5 m above the earth. At some points, the measurements were conducted using a source supported at the top of a slender duralumin mast, 25 m in height.

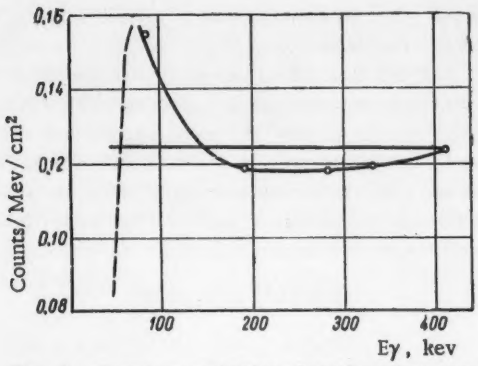

Fig. 1. Counter sensitivity plotted against energy of γ radiation.

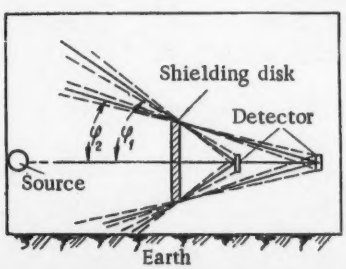

Fig. 2. Diagram of the experiment.

For measurements at large distances from the source, a powerful gamma emitter was made of Au^{198}, having an activity of ~ 10,000 C. The total radiation intensity was measured with a Geiger counter of the type described in reference [1]. The sensitivity response of this counter as a function of γ-radiation energy is shown in Fig. 1. Note that multiply scattered γ photons from the Au^{198} source, at energies of 120-410 kev, are registered by the counter with uniform sensitivity. Each event registered in the counter corresponded to a γ-ray energy flux of $8 \pm \pm 0.4$ Mev/cm^2 passing through the counter. Radiation at energies of 60-120 kev was registered by the counter with slightly enhanced sensitivity. However, the maximum increase in sensitivity did not exceed 20%. Radiation at energies below 50 kev completely escaped detection by the counter. In referring to measurements of the radiation intensity in what follows, we accordingly have in mind only radiation $E\gamma > 50$ kev.

The angular distribution was measured by a radiation detector assembly consisting of an array of four counters placed in series. The effective volume of the detector setup was $4.5 \times 4.5 \times 0.5$ cm. This detector was placed in back of a thick leaden disk measuring 21 cm in diameter, in a manner such that the centers of the disk and of the detector coincided on the same straight line with the center of the source. The arrangement of the disk, source, and detector may be seen in Fig. 2. It is clear that the leaden disk shields the detector from any radiation arriving at the point of measurement at angles smaller than φ. This angle φ is read off from the straight line joining the source at the point of measurement. By varying the distance between disk and detector, it was possible to obtain information on the angular distribution of the radiation for angles φ from 0 to 90°. The results of the measurements performed are shown in Figs. 3 and 4.

As we see from Fig. 3, when the source and detector are placed close to the ground, the intensity of the radiation at great distances from the source proved to be roughly half that established for a homogeneous air medium. When the source was placed in

elevation above the gound, this difference was lessened, e.g., at a height of 25 m, the radiation intensities at the same distances differed by only 1.5 times. The data fit well with the considerations voiced in [4] as to the effects of having the source at a distance from ground level on the intensity of radiation in air.

Data on the angular distribution of scattered radiation are given in Fig. 4, where we have indicated the percentage contribution owing to γ photons arriving at the point at angles smaller than the specified

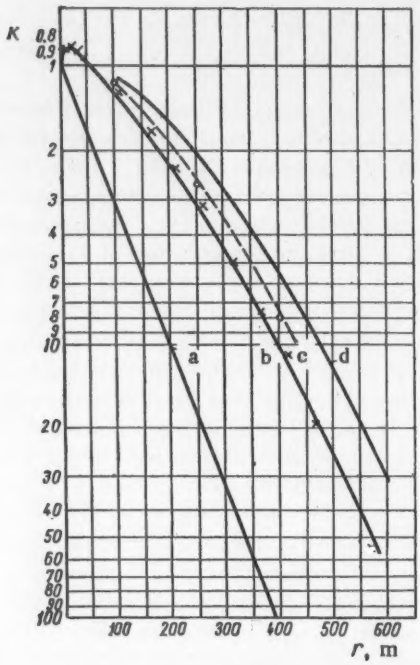

Fig. 3. Absorption coefficients and intensities of nonscattered radiation on the distance between source and detector: a) absorption coefficients K (at T = 0°C and H = 740 mm Hg), showing the number of times by which the intensity of radiation in the air above the ground is weakened as a result of interaction with airborne matter; b) the same for the source placed 25 meters above ground level; c) exponential law of attenuation of the intensity of primary radiation from the source, with scattered radiation effects neglected; d) law of attenuation of radiation intensity of emissions of Au^{198} in a homogeneous air medium [2, 3].

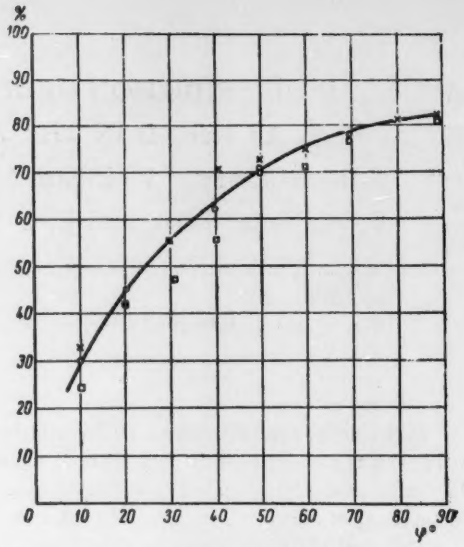

Fig. 4. Angular distribution of the scattered radiation. Distance from radiation source (in m): O) 150; X) 250; □) 400.

angle φ. As we see, within the limits of the statistical scatter of the radiation counter counting rate ($\pm$ 10% for r = 400 m), the angular distribution of the radiation at substantial distances was independent of the distance from the source, i.e., the angular distribution represented by the curve plotted in Fig. 4, while stable over the first 100-150 m, varied very slightly as r was increased further.

The authors take this opportunity to express their acknowledgement to O. I. Leipunskii, with whom the idea underlying the experiment originated, and to V. A. Rogachkov, V. A. Shabashov, V. N. Rodionov, whose kind assistance was of great value in the work with the powerful γ-ray emitter under field conditions.

LITERATURE CITED

1. V. N. Sakharov, Atomnaya Énergiya 3, 61 (1957).*
2. V. N. Sakharov, Atomnaya Énergiya 3, 57 (1957).*
3. S. G. Tsypin, V. I. Kukhtevich, and Yu. A. Kazanskii, Atomnaya Énergiya 2, 71 (1956).*
4. O. I. Leipunskii and V. N. Sakharov, Atomnaya Énergiya 6, 585 (1959).*

*Original Russian pagination. See C. B. translation.

GAMMA RAYS EMITTED IN INELASTIC SCATTERING OF NEUTRONS AT 3 MEV ENERGY

A. L. Androsenko, D. L. Broder, A. I. Lashuk

Translated from Atomnaya Énergiya, Vol. 7, No. 3, p. 268
September, 1959,
Original article sumbitted January 6, 1959

The inelastic scattering of fast neutrons on nuclei is of considerable interest both for the study of the structure of the nucleus and for the pratical design of fast reactors, biological shielding in nuclear facilities, etc.

The present paper reports studies of the energy levels in nuclei,based on measurements of the energy of γ rays emitted in the inelastic scattering of neutrons of energy E_0 = 3 Mev. The energy spectra of gamma rays emitted from titanium, chromium, strontium, iodine, barium, tungsten, iridum, and iridium, and bismuth nuclei were measured by means of a scintillation γ spectrometer using NaI(Tl) crystal scintillators.

Experimental arrangement. The D(d, n)He^3 reaction was utilized as a neutron source. A beam of deuterons accelerated to an energy of 200 kev impinged on a target of deuterium adsorbed on zirconium. This neutron source, with a power of 10^7 neutrons/sec, was brought to approximately 2 m from the massive accelerator parts.

A lead cone 36 cm in height with a base diameter of 5.8 cm was used to shield the crystal from direct impingement of radiation emanating from the target. The crystal with accompanying photomultiplier tube and preamplifier, the test samples, and the cone were suspended from the ceiling of the room on caprone filaments 0.7 mm in diameter.

The elements to be tested were prepared in the form of rings. The height of the heavy-element rings was 30 mm, and that of the light-element rings was 40 mm. The rings had an I.D. of 60 mm and an O. D. of 85 and 95 mm for heavy and light elements, respectively. While measurements were in progress, the rings were fitted around the crystal.

The scintillation γ spectrometer consisted of a single NaI(Tl) crystal 40 mm in diameter and height, connected to a photomultiplier via a light-pipe of plexiglass 6 mm thick, a nonoverdriven amplifier and a 128 channel kicksorter with ferrite memory storage unit. The energy resolution of the spectrometer was 10% for gammas emitted by Zn^{65}.

Monitoring for constancy of neutron flux was handled by a full-wave boron counter set at a distance of 2 m from the accelerator target, at right angles to the direction of deuteron flux.

Results of the measurements. In order to find out what was the contribution of either γ rays or of neutrons scattered from surrounding objects and scattering agents to the cyrstal count, measurements of the pulse spectrum for pulses due to a carbon scatterer were taken after each run of measurements with the scatterer being tested. All of the results were reduced to a uniform monitor count, and the background measured with the carbon scatterer was subtracted. However, in the low-energy region of the energy spectrum (down to 0.3 Mev), the background was not subtracted, since this would have been associated with difficulties arising in the scaling process, owing to nonuniform absorption coefficients of the γ rays of those energies, for carbon and heavier elements being tested. The γ-ray spectra in that energy region were therefore arrived at, for certain elements, without deduction of background.

Figures 1-4 (see following pages) give the spectra of the γ rays accompanying the inelastic scattering of 3-Mev neutrons on nuclei of strontium, barium, tungsten, and iridium. The Table presents energies of γ quanta as measured in the course of our work and as reported by other authors.

In conclusion, the authors view it their welcome duty to thank A. K. Krasin for his constant interest in the work and his cooperation in setting up the experiment, A. N. Serbinov for his kind assistance, and I. I. Bondarenko and V. V. Stavinskii for their fruitful discussions.

LITERATURE CITED

1. V. Scherrer, B. Allison and W. Faust, Phys. Rev. 96, 386 (1954).
2. I. Van Loef and D. Lind, Phys. Rev. 101, 103 (1956).
3. R. Kiehn and C. Goodman, Phys. Rev. 95, 989 (1954).
4. R. Day, Phys. Rev. 102, 767 (1956).

THE EFFECT OF THE SPACE CHARGE ON THE MOTION OF PARTICLES IN ACCELERATORS

V. I. Kotov and V. A. Pushtarik

Translated from Atomnaya Énergiya, Vol. 7, No. 3, pp. 268-272
September, 1959
Original article submitted April 20, 1959

The question of the effect of the space charge of a beam on the free oscillations of particles acquires much significance in relation to the problem of obtaining high currents in accelerator machines. This problem has been discussed in the literature [1, 2], but the screening effect of the vacuum chamber walls and of the electromagnet pieces has not been taken into due account. The work reported by the authors takes into account both these factors, with only the horizontal chamber walls being considered in the problem, since the screening effect contributed by the vertical walls is substantially less.

Let us visualize a beam of particles as an infinitely long cylinder of radius ρ. Now, if we assume the walls of the vacuum chamber to be ideally conducting and take the permeability of the iron to be infinitely large, we shall find the following expressions to hold, outside of the beam, for the vector and scalar potentials [3]:

$$\left.\begin{aligned} A &= -\pi N e \beta \rho^2 \ln\left[\operatorname{ch}^2\frac{\pi x}{h}\sin^2\frac{\pi z}{h} + \right.\\ &\left. + \operatorname{sh}^2\frac{\pi x}{h}\cos^2\frac{\pi z}{h}\right];\\ \varphi &= \pi N e \rho^2 \ln\left[\frac{\operatorname{ch}\frac{\pi x}{\alpha h}+\cos\frac{\pi z}{\alpha h}}{\operatorname{ch}\frac{\pi x}{\alpha h}-\cos\frac{\pi z}{\alpha h}}\right], \end{aligned}\right\} \quad (1)$$

where A is the component of the vector potential along the beam axis; $\beta = v/c$; N is the number of particles in a unit volume; $\underline{x}$ and $\underline{z}$ are deviations from the beam axis in the horizontal and vertical directions; α is the ratio of the vertical aperture of the chamber to the spacing $\underline{h}$ between the electromagnetic pole pieces. Assuming $\rho/h << 1$ and solving the Maxwell equations for the inner region of the beam, we get:

$$\left.\begin{aligned} \mathscr{E}_x &= 2\pi e N x\left[1-\frac{\pi^2}{6\alpha^2}(\rho/h)^2\right];\\ \mathscr{E}_z &= 2\pi e N z\left[1+\frac{\pi^2}{6\alpha^2}(\rho/h)^2\right];\\ H_x &= 2\pi e N \beta z\left[1+\frac{\pi^2}{3}(\rho/h)^2\right];\\ H_z &= -2\pi e N \beta x\left[1-\frac{\pi^2}{3}(\rho/h)^2\right]. \end{aligned}\right\} \quad (2)$$

$\mathscr{E}_{x,z}, H_{x,z}$ are components of the electric and magnetic fields. The calculation of those fields leads to the following equations for free oscillations:

$$\left.\begin{aligned} x'' + k^2[1-(n-\delta n_x)]\,x = 0,\\ z'' + k^2[n+\delta n_z]\,z = 0, \end{aligned}\right\} \quad (3)$$

where differentiation is carried out along the length of an arc of the equilibrium orbit σ; $\underline{k}$ is the curvature of the orbit; $\underline{n}$ is the index of the accelerator guide magnetic field;

$$\delta n_{x,z} = -\frac{2\pi e^2 N}{k^2 E \beta^2}\left[(1-\beta^2) \pm \frac{\pi^2}{6}(\rho/h)^2(1/\alpha^2-2\beta^2)\right] \quad (4)$$

(here the upper sign refers to δn_x and the lower sign refers to δn_z; E is the total energy of a particle).

From (3), it is not difficult to derive the formula for the frequency variation of free oscillations [4, 5].

$$\Delta\nu_{x,z} = \frac{Le^2N}{2E\beta^2}\left[(1-\beta^2) \mp \right.$$
$$\left. \mp \frac{\pi^2}{6}(\rho/h)^2(1/\alpha^2-2\beta^2)\right]\overline{|\Psi_{x,z}|^2}. \quad (5)$$

The quantity $\overline{|\Psi_{x,z}|^2}$ is the mean value of the square of the modulus of Floquet's function, which in our case is normalized such that the Wronskian

$$\Psi_{x,z}\Psi^{*1}_{x,z} - \Psi^{*}_{x,z}\Psi^{1}_{x,z} = -2i,$$

where L is the perimeter of the orbit. If the operating point falls at the center of a cell bounded by resonance bands, then assuming that $|\Delta\nu_{x,z}| = 1/4$ (i.e., is equal to the distance to the nearest resonance), we find the limitation on the beam current for a beam injected into the accelerator chamber.

From (5), we see that the screening effect (second term within the brackets) yields a contribu-

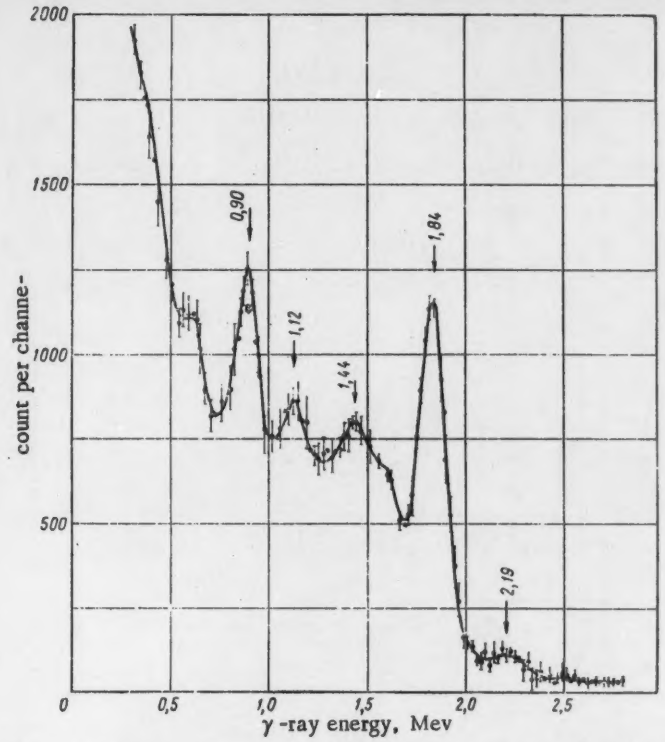

Fig. 1. Spectrum of pulses excited by γ rays accompanying inelastic scattering of 3-Mev neutrons in strontium.

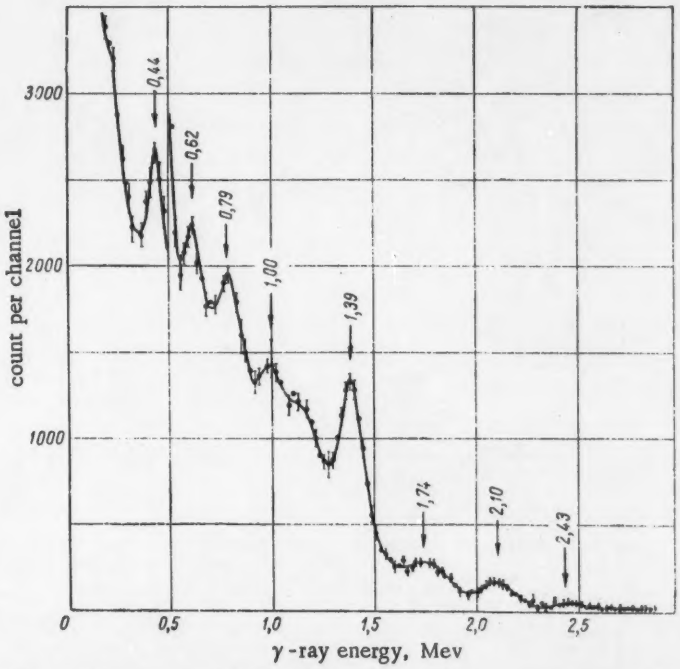

Fig. 2. Spectrum of pulses excited by γ rays accompanying inelastic scattering of 3-Mev neutrons in barium.

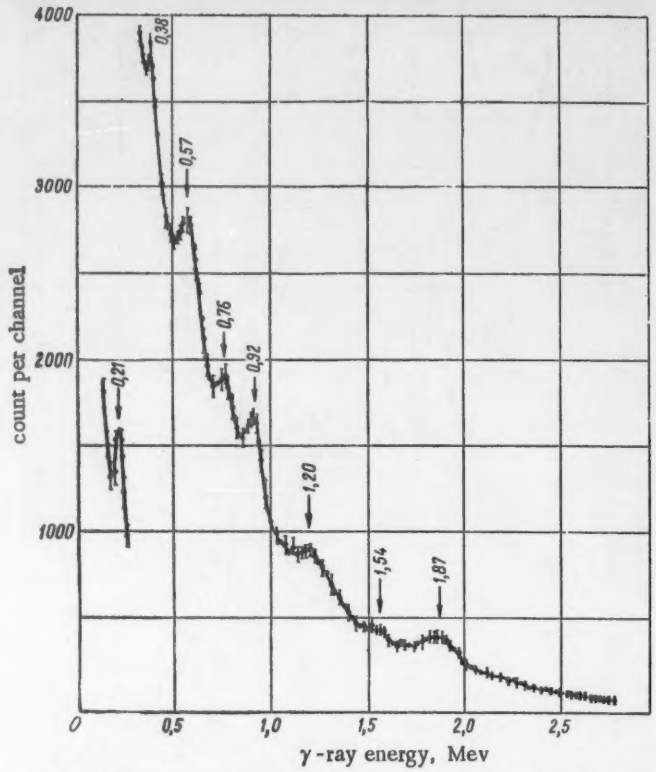

Fig. 3. Spectrum of pulses excited by γ rays accompanying inelastic scattering of 3-Mev neutrons in tungsten.

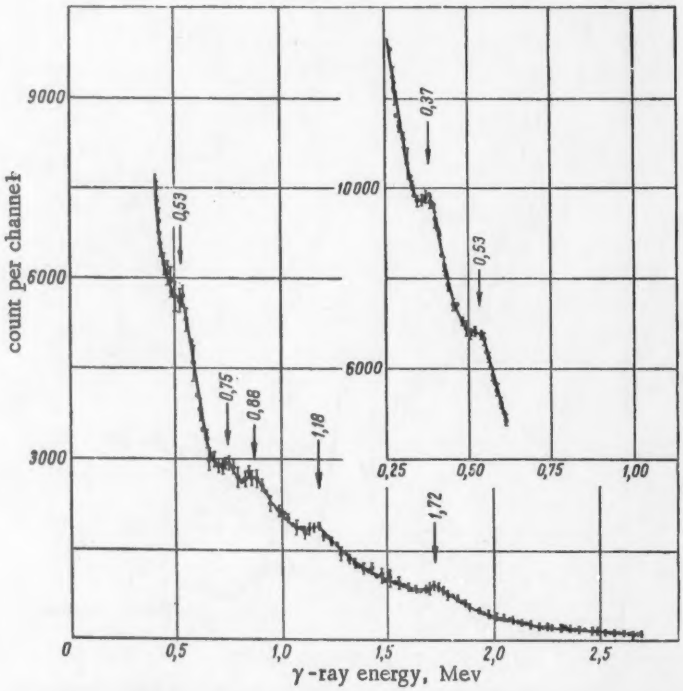

Fig. 4. Spectrum of pulses excited by γ rays accompanying inelastic scattering of 3-Mev neutrons in iridium.

Element	γ-ray energy, Mev				
	Our results	Findings reported by other authors			
		[1]	[2]	[3]	[4]
Ti	0,43±0,03	—	—	—	—
	(0,64±0,03)	—	—	—	—
	0,96±0,03	0,92±0,05	—	—	—
	1,32±0,04	1,30±0,06	—	—	—
	2,02±0,04	2,2 ±0,18	—	—	—
Cr	(0,80±0,03)	0,75±0,03	—	—	—
	0,99±0,03	0,97±0,04	—	1,02	—
	1,42±0,04	1,43±0,06	—	1,44	—
	1,93±0,04	—	—	—	—
Sr	(0,37±0,03)	—	—	—	—
	0,90±0,03	—	—	—	—
	1,12±0,04	—	—	—	—
	1,44±0,04	—	—	—	—
	1,84±0,04	—	—	—	—
	2,19±0,04	—	—	—	—
I	—	0,21±0,01	0,208±0,002	0,200	—
	0,35±0,03	0,33±0,01	0,390±0,010	—	—
	0,42±0,03	0,42±0,02	0,435±0,004	0,410	—
	0,62±0,03	0,63±0,03	0,632±0,006	0,630	—
	0,76±0,04	—	0,750±0,020	—	—
	0,98±0,04	1,04±0,05	0,950±0,020	—	—
	1,25±0,04	—	—	—	—
	1,76±0,04	—	—	—	—
Ba	0,44±0,03	0,47±0,02	—	—	—
	0,62±0,03	0,60±0,03	—	—	—
	0,79±0,03	0,78±0,04	—	—	—
	1,00±0,04	1,06±0,05	—	—	—
	—	1,19±0,06	—	—	—
	1,39±0,04	1,41±0,06	—	—	—
	—	1,51±0,06	—	—	—
	1,74±0,04	—	—	—	—
	2,10±0,05	2,10±0,1	—	—	—
	2,43±0,06	—	—	—	—
W	0,21±0,03	—	—	—	—
	0,38±0,03	—	—	—	—
	0,57±0,03	—	—	—	—
	0,76±0,03	—	—	—	—
	0,92±0,03	—	—	—	—
	1,20±0,04	—	—	—	—
	1,54±0,04	—	—	—	—
	1,87±0,05	—	—	—	—
Ir	0,37±0,03	—	—	—	—
	0,53±0,03	—	—	—	—
	0,75±0,03	—	—	—	—
	0,88±0,03	—	—	—	—
	1,18±0,04	—	—	—	—
	1,72±0,04	—	—	—	—
Bi	0,57±0,03	0,49±0,02	—	—	—
	0,90±0,03	0,94±0,05	—	0,895±0,025	0,904±0,009
	1,29±0,03	—	—	—	—
	1,61±0,03	1,62±0,7	—	1,56±0,035	1,615±0,016
	—	—	—	—	—
	2,53±0,04	2,6±0,1	—	—	2,600±0,020

Note: Values enclosed in parentheses indicate energies of γ lines whose existence is in doubt.

tion of the order of 10-20% in the nonrelativistic case. Contrariwise, in the relativistic case ($\beta \simeq 1$), it may play a paramount role, leading to an additional limitation on the number of sectors accumulated as the particles accumulate in the accelerators.

LITERATURE CITED

1. S. Barden, Phys. Rev. 93, 1378 (1954).
2. V. B. Berestetskii, L. L. Gol'din, and D. G. Koshkarev, Pribory i Tekh. Éksp. No. 3, 126 (1956).
3. W. R. Smythe, Static and Dynamic Electricity (McGraw-Hill, N. Y., 1950).
4. G. Luders, Nuovo cimento, Suppl. ser. 10, 2, (4), 1075 (1955).
5. A. A. Kolomenskii, Zhur. Tekh. Fiz. 26, 1978 (1956).

RELATION BETWEEN THE THERMAL PROPERTIES AND THE ATOMIC AND MOLECULAR STRUCTURE OF CARBON IN HOMOGENEOUS GRAPHITIZATION

V. I. Kasatochkin, V. K. Zamoluev and A. T. Kaverov

Translated from Atomnaya Énergiya, Vol. 7, No. 3, pp. 272-275
September, 1959
Original article submitted November 21, 1957

The properties of carbon materials which are of practical engineering significance, in particular its thermal properties, are related to the atomic and molecular structure of those materials.

X-ray diffraction analysis data have shown the coexistence of amorphous and crystalline phases in the process of homogeneous graphitization of carbon (at 2000°-2800° C) [1]. This process must therefore be assigned to the category of orientation processes, which are similar to processes involved in the formation of oriented polymers [2].

Homogeneous graphitization of carbon is characterized by a continuous improvement in the spatial orderedness of the crystal lattice of graphite, through azimuthal orientation [3] of parallel-layer elementary atomic lattices of carbon in groups (packets) formed prior to the crystallization stage.

This letter reports results obtained in research on the specific heat, thermal diffusivity, and thermal conductivity, as well as x-ray powder determinations of the degree of graphitization of petroleum coke under isothermal conditions, for a range of different temperatures and furnace times. Petroleum cracking coke of 1.405 g/cm^3 density with an ash content of 0.08% and a 5.13% yield of volatiles was used in the experiment. The dry weight of the samples ranged 0.50-0.60 g/cm^3, and the grain composition ranged from 0 to 0.5 mm.

Graphitization was accomplished in a furnace with a graphite heating unit, in an atmosphere of nitrogen and argon. The maximum departure of the temperature from set point were ± 25° C. The degree of graphitization was determined[4] on the basis of measurements of the interlayer spacing $d_{(002)}$ from the formula

$$\gamma = \frac{d_{max} - d}{d_{max} - d_{min}},$$

where d is the measured interlayer spacing; d_{min} = 3.356 A is the interlayer spacing in the crystalline lattice of critically graphitized carbon; d_{max} = 3.425 A is the interlayer spacing of nongraphitized carbon. X-ray patterns of the graphitization products were obtained by filtered radiation of copper and iron in cylindrical 70- and 43- millimeter diffraction cameras.

The specific heat and the thermal diffusivity constant of the samples were determined at 20-35° C according to the method of the regular thermal regime [5] modified for the study of trace quantities of matter [6]. The results of parallel experiments differed by not more than 1%.

On the basis of experimental data on the determination of the specific heat c_p, the thermal diffusivity a, and the weight by volume δ, the value of the thermal conductivity constant λ was calculated as $\lambda = a c_p(\delta)$.

Figure 1 shows the degree of graphitization as a function of temperature and of the isothermal holding time, corresponding to the equation

$$K = K_0 l^{-\frac{E}{kT}},$$

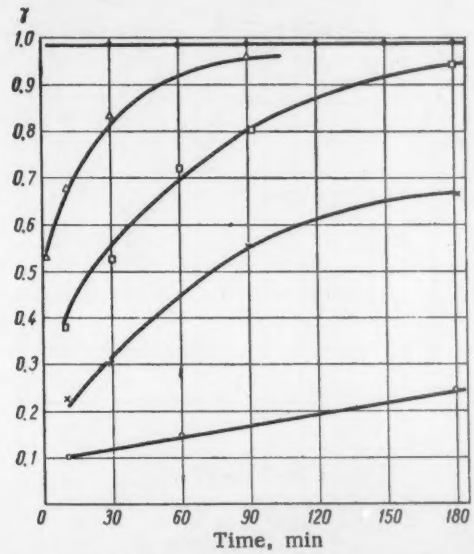

Fig. 1. Interlayer spacings $d_{(002)}$ as a function of the time of isothermal graphitization of cracking coke. Temperature, °C; O) 2000; X) 2150; □) 2300; Δ) 2420; o) 2800;

where E = 95 kcal/g-atom is the energy of activation of the graphitization process; $K_0 = 10^4$.

The results of studies of the specific heat c_p, thermal diffusivity a, and thermal conductivity λ of the samples as temperature functions and as functions of the isothermal holding time in the furnace, as well as a function of the degree of graphitization γ are plotted in Figs. 2-4.

The regular patterns observed in the variation of the quantitites γ, c_p, a, and λ may be explained by the kinetics and the mechanism operating in the structural-chemical transformations. The original coke had the structure of a three-dimensional polymer in the form of an assemblage of relatively small planar monolayers of carbon interconnected by side-chain atomic groups containing, in addition to carbon, hydrogen, oxygen, and many other elements [3]. In the precrystallization stage of heat treatment (up to ~ 1800° C), thermal destruction of the side-chain radicals took place, accompanied by a growth of carbon monolayers due to the coalescence of the latter and the formation of packets of parallel monolayers connected by side chains of carbon with monolayers of the neighboring packets. These processes were accompanied by the escape of volatile products with the attendant loss of a large quantity of the terminal atomic groups, and led to an increase in the fraction of carbon in the monolayers being included into the structure of the three-dimensional polymeric carbon skeleton. The structural-chemical transformation in this stage of heat treatment found their reflection in a reduction in specific heat c_p (reduction by ~ 50%) and an increase in the thermal diffusivity constant a (Fig. 3). During the graphitization stage proper, orientation processes occurred in the stacking of carbon monolayers into place in the crystal lattice of graphite, those processes being linked to the chemical processes involved in the destruction of the side carbon chains, as indicated by the high value of the energy of activation of the graphitization process (~95 kcal/g-atom).

A lowering by ~ 1/3 in the specific heat during the graphitization stage pointed to loss of two degrees of freedom in the overall vibrational spectrum of carbon atoms.

The physical causal agent for that effect is related to the redistribution of the frequency of thermal lattice vibrations (as indicated earlier for lamellar structures [7] in the monolayers of carbon freed from the side valency chains during the process of destruction of the side carbon chains.

The linear behavior of the dependence of the specific heat c_p, thermal diffusivity constant a, and thermal conductivity λ on the degree of graphitization γ (Fig. 4), if the initial period of graphitization (~ 0.1), during which stacking processes in the

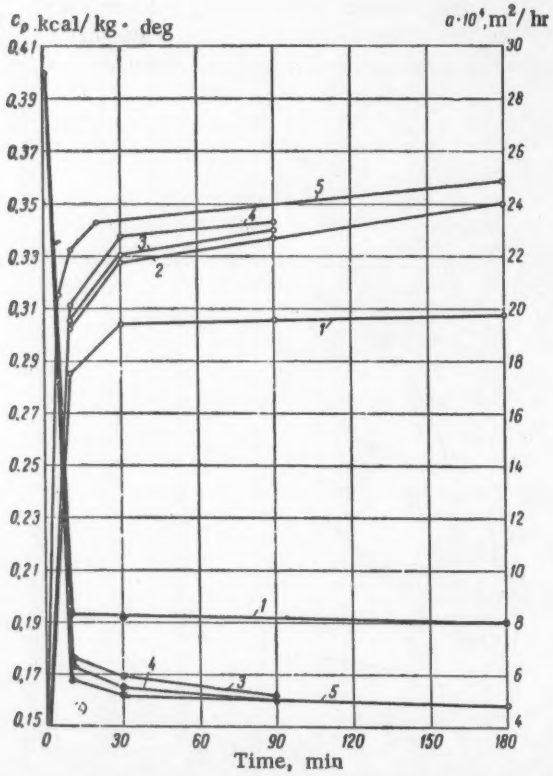

Fig. 2. Measurements of the specific heat (o) and thermal diffusivity (O) as a function of the time of isothermal graphitization of cracking coke. Temperature, in °C: 1) 2000; 2) 2300; 3) 2400; 4) 2600; 5) 2800.

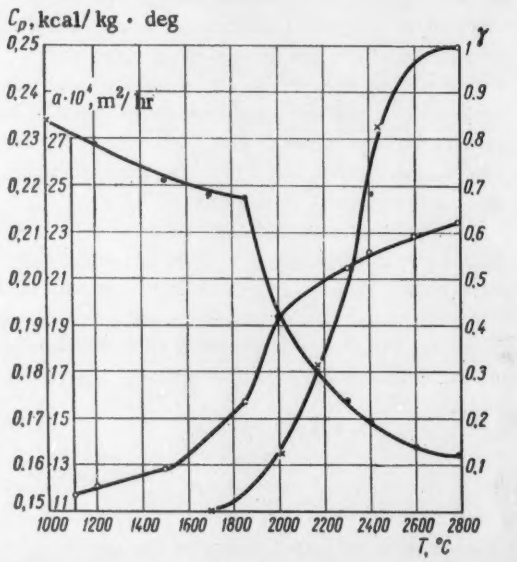

Fig. 3. Variations in the specific heat (o) thermal diffusivity constant (O) and degree of graphitization (X) as a function of the temperature of graphitization of cracking coke. (Time of graphitization: 30 min).

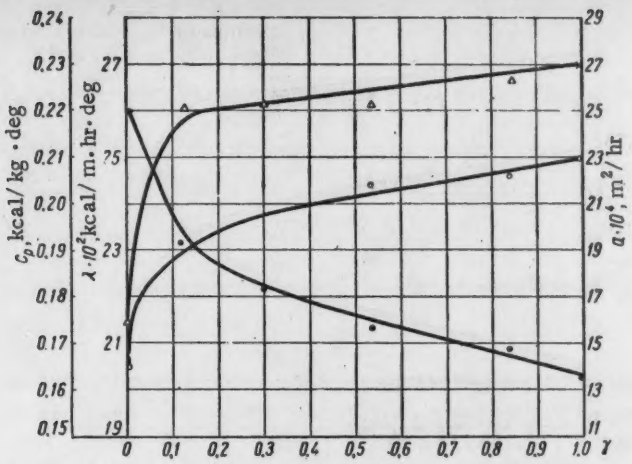

Fig. 4. Specific heat (o) thermal diffusivity constant (O) and thermal conductivity (Δ) as functions of the degree of graphitization.

precrystallization stage are still possible, is excluded, points to structural and chemical transformations of the polymeric carbon backbone.

Relatively small increases in the thermal conductivity λ, the basic changes which occurred during the precrystallization stage, were noted during the graphitization stage. In order to obtain carbonaceous material exhibiting relatively high thermal conductivity combined with rather high mechanical strength properties, it was not necessary, therefore, to effect the complete graphitization of the carbon. Heat treatment of the original petroleum coke stock need be carried through no further than the initial stages of graphitization. In order to enhance heat stability, which is related to the thermal diffusivity, efforts must be made to reach critical graphitization of the carbon. Data obtained enable us to also explain the small degree of variability in the specific heat of neutron-irradiated graphite [8, 9]. When graphite is subjected to neutron bombardment, the three-dimensional ordering of the carbon, γ, suffers considerably, and the interlayer spacing d between the periodic carbon monolayers increases, with accompanying swelling of the graphite [8].

The graphite monolayers in samples having a high degree of graphitization of the carbon [$\gamma \sim 1$) are practically without side bonding (carbon chains). The internal changes in the monolayers in response to neutron bombardment, the azimuthal disorientation (and consequently the lowering of γ and increase in d) are not associated with the transformations in the spatial polymeric carbon backbone, and are therefore without effect on changes in specific heat. We may add to this fact that the swelling of the graphite in itself testifies to the absence of side links between the monolayers of neighboring crystallites.

The results of the research may be used to produce carbonaceous materials from petroleum coke having preengineered thermodynamic properties.

LITERATURE CITED

1. R. Franklin, Acta Cryst. 4, 253 (1951); R. Franklin, Proc. Roy. Soc. 209, 196 (1951).
2. V. A. Kargin and G. L. Slonimskii, Uspekhi Khim. 24, 785 (1955).
3. V. I. Kasatochkin, Izvest. Akad. Nauk SSSR, OTD 9, 32 (1951).
4. V. I. Kasatochkin and A. T. Kavernov, Doklady Akad. Nauk SSSR 117, No. 5 (1957).
5. G. M. Kondrat'ev, The Regular Thermodynamic Regime [in Russian] (Gostekhizdat, Moscow, 1954).
6. V. K. Zamoluev and V. I. Kasatochkin, Izvest. Akad. Nauk SSSR, OTN 11, 190 (1957). V. K. Zamoluev and V. I. Kasatochkin, Koks i Khimiya 6, 21 (1957).
7. V. V. Tarasov, Doklady Akad. Nauk SSSR 46 117 (1945); V. V. Tarasov, Trudy Inst. Krist. Akad. Nauk SSSR 10, 304 (1954).
8. Hennig and Howe, Report 751, Geneva Conference (1955) Vol. 8.
9. W. De Sorbo and W. Tyler, J. Chem. Phys. 26, 244 (1957).

THE TRANSPORT EQUATION IN ISOTOPE SEPARATION GEAR

G. Barvikh and R. Ya. Kucherov

Translated from Atomnaya Énergiya, Vol. 7, No. 3, pp. 275-276
September, 1959
Original article submitted January 6, 1959

In this contribution, an equation describing the transport of isotopes in separatory equipment is derived. No assumptions are made in the derivation as to the method of separation used, the design of the equipment, or the character of the fluid dynamic flows, which enables us to utilize the equation for the study of a wide variety of separatory devices. The equation was derived by a method first used in the study of a thermal diffusion column [1, 2], and is based on an assumption that the variation in concentration over the transverse cross section of the equipment is small, which is a restraint well satisfied in most cases of isotope separation.

A considerable number of the processes used for isotope separation are described by the equation

$$\vec{\tau}_1 - \vec{\tau} c = -\beta [\nabla c + \vec{\delta} c (1-c)], \qquad (1)$$

where $\vec{\tau}_1$ is the convection velocity of the light isotope; $\vec{\tau}$ is the convection velocity of the isotope mixture; c is the molar fraction of the light isotope in the isotope mixture. Coefficients β and $\vec{\delta}$ are, generally speaking, functions of the coordinates. Their value is dependent on the method of separation in use. For example, in the thermal diffusion process, β is the diffusion coefficient, $\vec{\delta} = \alpha \nabla \ln T$ (α being the thermal diffusion constant, and T the temperature); in centrifugation

$$\vec{\delta} = \frac{m_2 - m_1}{kT} \omega^2 \vec{r}$$

(ω is the angular velocity, m_i is the mass of a molecule of the ith isotope, and k is Boltzmann's constant).

In what follows, we shall restrict ourselves to the steady-state two-dimensional problem, for the sake of simplicity. For process equipment possessing cylindrical symmetry, the equation is derived in similar fashion.

A diagram of the separatory process equipment is shown here. The flow of the mixture of isotopes, admitted to the bottom of the equipment and discharging from the top, is equal to I. The corresponding flow of light isotope is I_1. Then, obviously,

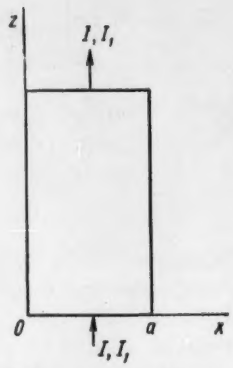

Diagram of separatory equipment.

$$I = \int_0^a \tau_z dx;$$

$$I_1 = \int_0^a \tau_{1z} dx.$$

Let us now write out (1) for the components:

$$\tau_{1x} - \tau_x c = -\beta \left\{ \frac{\partial c}{\partial x} + \delta_x c (1-c) \right\}; \qquad (2)$$

$$\tau_{1z} - \tau_z c = -\beta \left\{ \frac{\partial c}{\partial z} + \delta_z c (1-c) \right\}. \qquad (3)$$

We introduce the notation

$$G(x, z) = \int_0^x \tau_z \, dx; \quad \varphi(x, z) = -\beta \left\{ \frac{\partial c}{\partial z} + \delta_z c (1-c) \right\}$$

Next, we take the integration of (3) with respect to x from 0 to a:

$$I_1 - I c_a = \int_0^a \varphi \, dx - \int_0^a G(x, z) \frac{\partial c}{\partial x} dx, \qquad (4)$$

where c_a is the value of $c(x, z)$ at $x = a$. We then eliminate $\partial c/\partial x$ from (4). For this, we integrate the equation of continuity of the light isotope, div $\vec{\tau} = 0$:

$$\tau_{1x} = -\frac{\partial}{\partial z}\int_0^x \tau_{1z}\,dx \tag{5}$$

and transform (5), with the aid of (3) and the equation div $\vec{\tau} = 0$:

$$\tau_{1z} = -\frac{\partial}{\partial z}\int_0^x \varphi\,dx - \int_0^x \tau_z \frac{\partial c}{\partial z}\,dx + c\tau_x - \int_0^x \tau_x \frac{\partial c}{\partial x}\,dx. \tag{6}$$

Substituting (6) into (2) and introducing the notation

$$\psi(x, z) = \frac{1}{\beta}\left(\frac{\partial}{\partial z}\int_0^x \varphi\,dx + \int_0^x \tau_z \frac{\partial c}{\partial z}\,dx\right) - \delta_x c(1-c), \tag{7}$$

we get

$$\frac{du}{dx} = \frac{\tau_x}{\beta}u + \psi\tau_x,$$

where

$$u = \int_0^x \tau_x \frac{dc}{dx}\,dx.$$

We then integrate this equation, and keeping in mind the fact that $dc/dx = 1/\tau_x \cdot du/dx$, we find

$$\frac{dc}{dx} = \frac{1}{\beta}e^{\int_0^x \frac{\tau_x}{\beta}dt}\int_0^x \psi\tau_x e^{-\int_0^{x'}\frac{\tau_x}{\beta}dt}\,dx' + \psi. \tag{8}$$

Substituting (8) into (4) yields:

$$I_1 - Ic_a = \int_0^a \varphi\,dx - \int_0^a G(x, z)\left[\frac{e^{\int_0^x \frac{\tau_x}{\beta}dt}}{\beta} \times \int_0^x \psi\tau_x e^{-\int_0^{x'}\frac{\tau_x}{\beta}dt}\,dx' + \psi\right]dx. \tag{9}$$

When $G(x, z)$ may be represented in the form $G(x, z) = X(x)Z(z)$, it is easily demonstrated, with the aid of the equation of continuity div $\vec{\tau} = 0$, and the obvious condition $\tau_x = 0$ at $x = 0$, that $G(x, z)/\tau$ is independent of x. This enables us to transform (9) to the form

$$I_1 - Ic_a = \int_0^a \varphi\,dx - e^{\int_0^a \frac{\tau_x}{\beta}dt} \times \times \int_0^a \psi G(x, z)\, e^{-\int_0^x \frac{\tau_x}{\beta}dt}\,dx. \tag{10}$$

Put $\Delta c = c(z, 0) - c(z, a)$. In accord with (2), $\Delta c \simeq a\delta_x$. In the separation of isotopes, $a\delta_x \ll 1$. This allows the possibility of replacing the values of c, dc/dz and d^2c/dz^2 entering into the integrands by c_a, dc_a/dz, and d^2c_a/dz^2, respectively, retaining accuracy to terms of the order of $(a\delta_x)^2$, and to then remove them from under the sign of the integral with respect to x. In addition, terms proportional to d^2c_a/dz^2 and $\alpha_z\, d/d_z[c_a(1-c_a)]$, also of the order of $(a\delta_x)^2$, may be discarded. Equations (9) and (10) acquire the form

$$I_1 - Ic_a = H(z)\,c_a(1-c_a) - K(z)\frac{dc_a}{dz}. \tag{11}$$

If $G(x, z)$, which must be found by solving the hydrodynamic problem, is known, the task of calculating $H(z)$ and $K(z)$ reduces to quadratures. When (10) and the constraint $\delta_z \ll \delta_x$ are valid, as is usually the case in isotope separation equipment, then

$$H(z) = e^{\int_0^a \frac{\tau_x}{\beta}dt}\int_0^a \delta_x G(x, z)\, e^{-\int_0^x \frac{\tau_x}{\beta}dt}\,dx; \tag{12}$$

$$K(z) = e^{\int_0^a \frac{\tau_x}{\beta}dt}\int_0^a \frac{G^2}{\beta} \times e^{-\int_0^x \frac{\tau_x}{\beta}dt}\,dx + \int_0^a \beta\,dx. \tag{13}$$

Equation (11) may be put to use in studies of both elementary separation equipment and of column-type devices with a complex configuration of hydrodynamic flow patterns (cf., e.g. [3]).

LITERATURE CITED

1. W. Furry, R. Jones and L. Onsager, Phys. Rev. 55, 1083 (1939).
2. K. Cohen, The Theory of Isotope Separation. (McGraw-Hill, New York, 1951).
3. G. Barvikh and R. Ya. Kuchervo, Symposium: Production of Isotopes, Powerful γ facilities, Radiometry, and Dosimetry [in Russian] (Izd. AN SSSR, 1958) p. 120.

THE INTERNAL CIRCULATION OF EXTRACTABLES AND TECHNOLOGICAL DESIGN OF AN EXTRACTION COLUMN IN TRIBUTYLPHOSPHATE EXTRACTION

A. M. Rozen

Translated from Atomnaya Énergiya, Vol. 7, No. 3, pp. 277-281
September, 1959,
Original article submiited May 7, 1958

A very familiar property of tributylphosphate (TBP) which sets it off from many other industrial solvents is its capacity to yield relatively stable chemical compounds with extractable components [1], which results in a competition between various substances in the organic phase and, as a consequence, in the exclusion of some compounds in favor of others.

Uranyl nitrate displayed a particularly vigorous ability to crowd out competitors. Owing to the high value of the partition ratio ($K_U \approx 40$ [2]), uranyl nitrate was capable, even at moderate concentrations, of displacing HNO_3 ($\tilde{K}_H \approx 0.2$) and other compounds from the organic phase. In this connection, at the bottom of the tower, where uranyl nitrate is absent

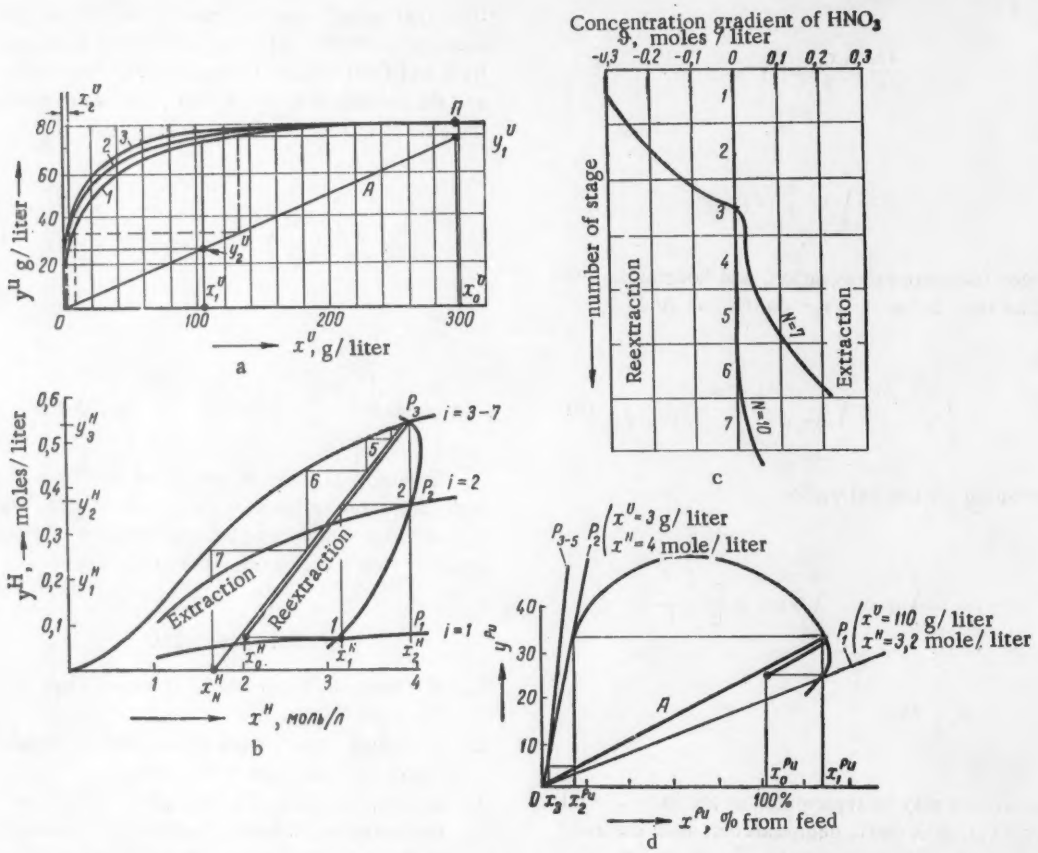

Fig. 1. x-y plot of the extraction and nature of variation in concentration gradient: a) uranyl nitrate (1, 2, 3 equilibrium lines for acidities, x^H = 2, 3, 4 moles / liter, A, operating line, II, critical point); b) HNO_3 (1. . .7. numbers of stages); c) variation in concentration gradient of HNO_3 along height of tower; d) plutonium.

and the partition coefficients of HNO_3 and of trace elements present are comparatively large, those substances are extracted efficiently. At the top of the extraction tower, on the other hand, uranyl nitrate being present there in a large yield, forces out the remaining elements from the organic phase, i.e., reextraction of the latter takes place under the effect of uranium. An internal circulation appears, leading to a buildup of some compounds in the midportion of the extraction tower; the peak concentration may be several times in excess of input (cf. Fig. 2a). In this letter, we take up briefly the question of this internal circulation on the basis of x-y diagrams plotted in somewhat unusual form. The further solution of the problem (whether by graphic or analytic means) presents no great difficulty.

Consider first the distribution of bulk elements, and then the distribution of trace elements governed by the former. A graphic analysis of the extraction in multicomponent systems, where the partition coefficient α depends on the concentration of several different components (e.g., α^U on x^U and x^H), may be carried out by the method of successive iterations, (approximations), plotting individual equilibrium curves for each plate. Since the equilibrium curves for uranium do not vary much as acidity is increased, the x-y diagram for uranyl nitrate has the usual form (Fig. 1a). Equilibrium curves may be based on data from the literature [2] (e.g., for 20% TBP in kerosene), the operating line may be based on assigned terminal points or one such point and the average ratio of flow of phases $\bar{n} = \bar{V}/\bar{L}$.* The stages are plotted, to a first approximation, on the equilibrium curve corresponding to an initial acid concentration x_0^H (dashed line), and to a second approximation by taking the variations in acid concentration on each plate. The corresponding relationship between concentrations and stage number of tower height, at HETS = const and n = 4.0, is seen in Figs. 2a, 2b.

The x-y diagram of HNO_3 (Fig. 1b) differs in the plotting of individual equilibrium curves for each plate on which uranyl nitrate is to be found (usually involv-

* In practice, sufficient accuracy may be secured by assuming $\underline{n}$ equal to the ratio of flows, at entrance to the extraction column, of the aqueous phase.

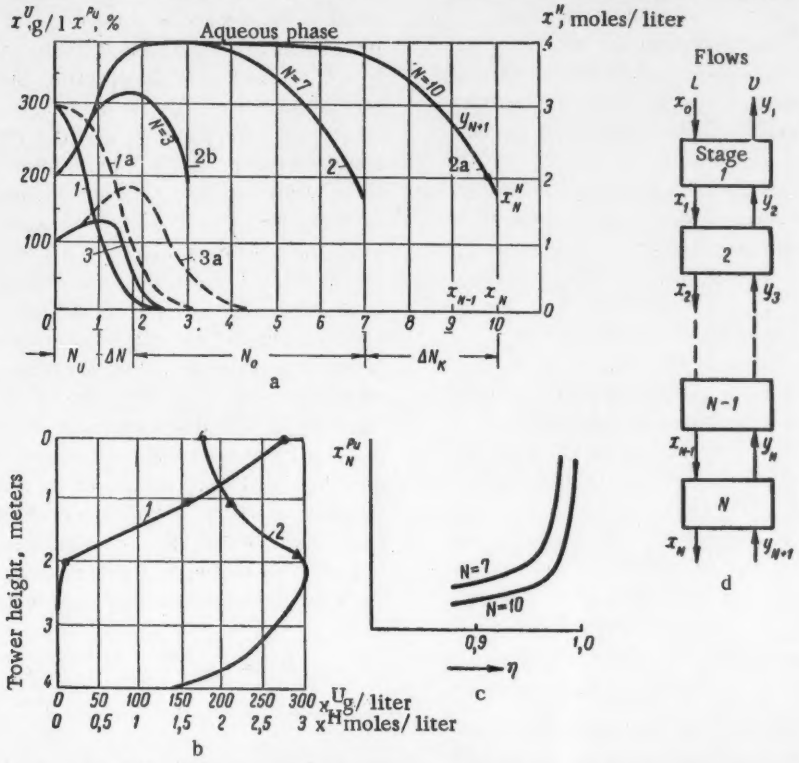

Fig. 2. Distribution of concentrations along the height of the extraction tower: a) design distribution of concentrations by stages, in the aqueous phase; 1) uranyl nitrate; 2) HNO_3 at number of stages N = 7 (2a. N = 10; 2b. at N = 3); 3) plutonium (1a and 3a uranyl nitrate and plutonium at $\underline{n} = 3.85$, $\eta = 0.95$); b) distribution along height of packed column: 1) uranyl nitrate, 2) HNO_3; c) dependence of concentration of plutonium in discard on η; d) diagram of tower in the form of a cascade of stages.

ing two or three of the top plates, e.g., in Fig. 1 x_1^U = 110 g/liter, x_2^U = 3 g/liter, $x_3^U \approx 0$; the numerical symbols are given to correspond to Fig. 2d); for the remaining plates, the equilibrium curve for the pure acid is used. In the extraction process, a transition occurs from the equilibrium curves P_1 to P_2 and P_3, while the total equilibrium curve acquires the form of a loop (Fig. 1b). A peculiar form is taken by the operating line. It rotates through 180° at the point of transition from extraction to back-extraction, at that point, the concentration gradient $\vartheta = y_p - y$ and the transverse flow of material $j_\perp = k\vartheta$ change signs (Fig. 1c), while the acid concentration runs through a maximum. The operating line is not bounded by the inflow and exit points (Fig. 1b); furthermore, those points are not fully specified: only the initial concentrations of the acid in the aqueous (x_0^H) and organic (y_{N+1}^H) phases and the ratio of flows n = V/L (i.e., the slope of the operating line tan $\alpha = \lambda = 1/n$) are given, while the corresponding values of the second set of coordinates (x_N^H and y_1^H) are unknown. The position of the operating line is therefore chosen by assigning some value of y_1^H or x_N^H and dividing the series of trial plots, in order to obtain a specified value of y_{N+1}^H or x_0^H for each particular number of plates considered [x_N^H and y_1^H may be found to an approximation by assuming that the partition coefficients $\alpha^H(x^H, x^U)$ are dependent solely on x^U, and using (1) and (2)].

The maximum buildup of acid, x_{max}^H, is bounded by the intersection of the operating line with the equilibrium curve, and increases as n = V/L; at n = 2, x^H = 3 moles/liter, and at n = 4, x_{max}^H = 4 moles/liter. Since x_{max}^H is bounded, then, as the number of plates are increased, a plateau appears in the concentrations, as seen in Fig. 2a. As is evident from inspection of Figs. 2a and 2b, the graphs plotted may be extended, to some degree of approximation, to packed columns.† However, the HETS in the uranium zone is somewhat higher than in the uranium-free region.

Extraction of trace elements. The partition coefficient of element M is determined by the concentration of bulk elements (uranyl nitrate and HNO_3), $\alpha^M = \alpha^M(x^U, x^H)$. Accordingly, it is not difficult to construct the equilibrium curve for each plate: $y_{equilb.\ i} = \alpha^M(x_i^U, x_i^H)\, x_i^M$, where i is the number of the plate, and x_i^U and x_i^H are as determined above. All of the constructions may be carried out for NHO_3 graphically (as an example, we have in Fig. 1d the x-y diagram for Pu (IV); α_{Pu} is taken from data reported in [3]). However, in some cases it is simpler to perform an analytical calculation. Using the equations for the operating line $y_i = y_{N+1} + \lambda(x_{i-1} - x_N)$ and for equilibrium $y_i = \alpha_i x_i$ as recurrent expressions, we find the concentrations of the element of interest in the discard (x_N) and in the organic phase at exit (y_1):

$$x_N = \frac{x_0 + n y_{N+1}(1 - \Pi\bar{\alpha}_i + \Sigma\Pi\bar{\alpha}_i)}{1 + \Sigma\Pi\bar{\alpha}_i}; \qquad (1)$$

$$y_1 = \frac{y_{N+1}\Pi\bar{\alpha}_i + \lambda x_0 \Sigma\Pi\bar{\alpha}_i}{1 + \Sigma\Pi\bar{\alpha}_i}, \qquad (2)$$

where $\lambda = 1/n$; $\bar{\alpha}_i = \alpha_i/\lambda = \alpha_i n$; $\Pi\bar{\alpha}_i = \bar{\alpha}_i\bar{\alpha}_2 \ldots \bar{\alpha}_n$; $\Sigma\Pi\bar{\alpha}_i = \bar{\alpha}_1 + \bar{\alpha}_1\bar{\alpha}_2 + \ldots + (\bar{\alpha}_1\bar{\alpha}_2 \ldots \bar{\alpha}_n)$. The degree of extraction of the element, Γ, at $y_{N+1} = 0$ is

$$\Gamma = \frac{x_0 - x_N}{x_0} = \frac{\bar{\alpha}_1(1 + \bar{\alpha}_2 + \bar{\alpha}_2\bar{\alpha}_3 + \ldots + \bar{\alpha}_2\bar{\alpha}_3 \ldots \bar{\alpha}_n)}{1 + \Sigma\Pi\bar{\alpha}_i}. \qquad (3)$$

Analyzing the x-y diagrams and (1)-(3), we may break the trace elements down into two groups. When the partition coefficient of the element is comparatively small in the absence of uranium ($\alpha_0 < 1/n$, $\alpha_0 < 1$), the buildup (as in the case of HNO_3) will be bounded by the intersection of the operating line with the equilibrium curve, and the degree of buildup $x_{max}/x_0 \leq 1/(1-\bar{\alpha}_0)$; when $\bar{\alpha}_0 \ll 1$, then that element will be extracted poorly, and will pass almost in its entirety, for practical purposes, into the discard. In that case, we find, from (3), $\Gamma = \bar{\alpha}_1 \ll 1$, $x_N = x_0(1 - \bar{\alpha}_1) \approx x_0$, the separation factor $K = 1/\Gamma \approx 1/\bar{\alpha}_1$.‡ Elements for which $\bar{\alpha}_0 = \alpha_0 n > 1$ may be considered readily extractable ($\Gamma \approx 1$, $x_N \approx 0$). In that case, the buildup is not bounded and will be dependent on the number of plates on which uranyl nitrate is found in amounts sufficient to secure reextraction, i.e., for the constraint $\alpha_{min} < 1$ to be observed. If this constraint is not satisfied on at least one plate ($n > 1/\alpha_{min}$), then there will be no buildup of the element at all; the element will be extracted monotonically [e.g., Pu (IV)] at n > 5. The degree of internal buildup in a readily extractable element comprises (provided the uranium barrier is acting on m plates):

$$q_{max} = \frac{x_{max}}{x_0} = \frac{1}{(\alpha_1 n)(\alpha_2 n) \ldots (\alpha_m n)}.$$

† Measurements performed by S. Medvedev and E. Rodionov.

‡ It is clear that for similar trace elements, saturation by uranium of the exiting organic phase entails a decrease in α_1 and will lead to improved separation.

Thus, for Pu (IV), m = 1, $\alpha \approx 0.18$, and the degree of buildup $q_{max} = 1/(4 \cdot 0.18) = 1.4$ (Fig. 2a). The buildup will be all the greater, the smaller the value of α_1, i.e., the greater the saturation of TBP with uranium at exit from the extraction column.

The buildup will rise sharply with an expansion of the uranium zone, e.g., as n decreases (curves 1a and 3a in Fig. 2a), etc., right up to the critical region corresponding to the intersection of the operating line with the equilibrium curve for uranium. At the transition beyond the critical region, the inadequacy of the volume of solvent leads to discard of the basic components.

Accordingly, the degree of approximation to the critical regime $\eta = \eta(n, x_0^U, T_0) = y_1/yP(x_0^U)$ is an important characteristic of the tower; on η depends on the buildup and the losses in valuable components (see Fig. 2c), and the required accuracy in control.

In the presence of a uranium barrier and buildup, additional plates are required for the complete extraction of valuable components (such as plutonium).

In schematizing the distribution and visualizing $\alpha \approx \alpha_0 = \text{const}$ in the uranium-free region, while $\alpha = \alpha_1 = \text{const}$ in the uranium-loaded region, we find

$$N = N_0 + N_U + \Delta N = \frac{\lg q \frac{\alpha_0 n}{\alpha_0 n - 1}}{\lg \alpha_0 n} + N_U + \frac{\lg q_{max}}{\lg \alpha_0 n}. \quad (4)$$

where N_0 is the number of plates required to extract the element in the absence of uranium; N_U is the number of plates in the uranium zone; ΔN is the number of plates required to reduce the concentration of the element from the maximum to the initial concentration; $q = 1/(1-\Gamma)$ is the degree of separation with respect to the particular element.

The increase in the required number of plates associated with internal circulation is rather high, e.g., for Pu (IV) at $\Gamma = 99.99\%$, $N_0 = 4.5$ and $N_U + \Delta N \approx 2$ (a 40% increase). In addition, there is also a certain reserve margin of plates ΔN_K required to

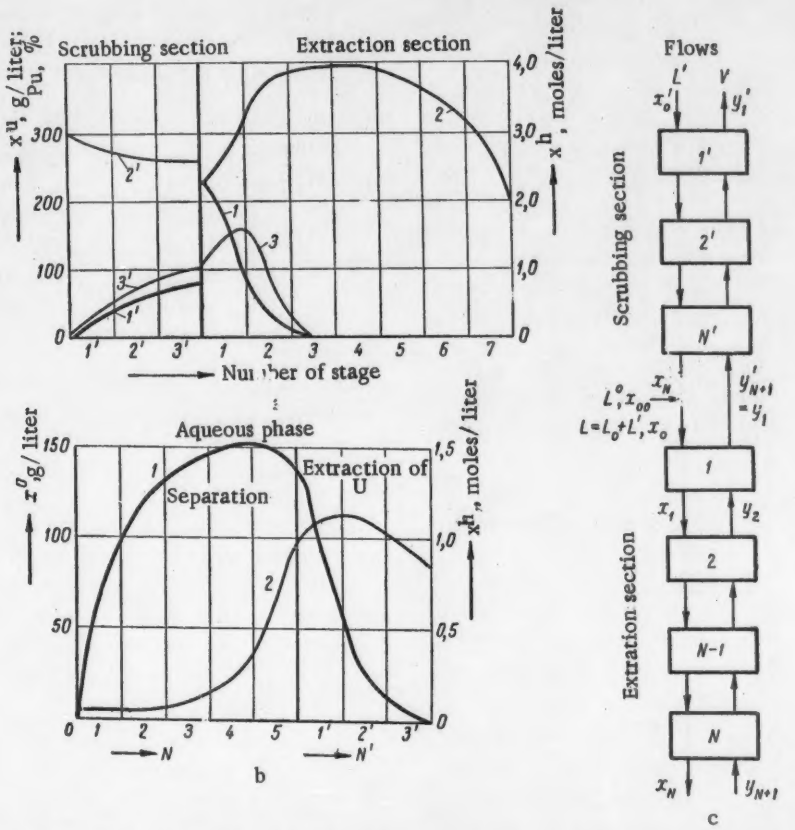

Fig. 3. Extraction with scrubbing and solvent recovery: a) Distribution of concentrations by stages in extraction with scrubbing operation (1. uranyl nitrate, 2. HNO_3, 3. Pu); b) distribution of concentrations by stages in the case of recovery in aqueous phase (1. uranyl nitrate, 2. HNO_3); c) diagram of extraction and scrubbing tower.

avoid waste during excursions in the direction of the critical mode of operation, in the course of process control (Fig. 2a).

More complicated cases, such as extraction with scrubbing, or solvent recovery (Fig. 3), are approached in similar fashion. In the first case, the concentrations of the elements in the aqueous phase at the feed point of the basic solution vary stepwise in line with the displacement equation $L'x'_{N+} L_0x_{00} = (L' + L_0)x_0$; the concentration in the organic phase varies smoothly, on the other hand. The concentration of bulk elements are found by graphical means, and the concentrations of trace elements are found by either graphical or analytical means (in the latter case, the solution of the system of equations for the scrubbing and extraction sections of the tower is required, using the displacement equations as the conditions which must be obeyed, and assuming $y_1 = y'_{N+1}$). By assuming $y_{N+1} = 0$, we find the concentrations of the discharging streams:

$$y_i' = \frac{\frac{x_0'}{n'}(AC+BD)+\frac{x_{00}}{n}AC(1+B)\left(1-\frac{n}{n'}\right)}{(1+B)D}; \quad (5)$$

$$x_N = \frac{\frac{n}{n'}x_0'+\left(1-\frac{n}{n'}\right)(1+B)x_{00}}{D}, \quad (6)$$

where

$$A=\Pi\bar{\alpha}', \quad B=\Sigma\Pi\bar{\alpha}', \quad C=\Sigma\Pi\alpha, \quad D=(1+B+AC).$$

For most compounds, $x'_0 = 0$, and the equations required for the calculations are simplified. In particular, the concentration of the elements remaining in the organic phase after the scrubbing operation will be

$$y_i' = y_1A/(1+B) = \frac{\Pi\bar{\alpha}'\Sigma\Pi\bar{\alpha}\left(1-\frac{n}{n'}\right)\frac{x_{00}}{n}}{1+\Sigma\Pi\bar{\alpha}'+\Pi\bar{\alpha}'\Sigma\Pi\bar{\alpha}}. \quad (7)$$

From (7) and (3), we find that the separation factor in scrubbing, $K = y_1/y_i' \simeq 1/\Pi\,\alpha' = 1/(\alpha_1' n)$ $(\alpha_2' n)$. . . The scrubbing step therefore effectively removes only those elements having rather small partition coefficients (if $\alpha_i' \leq 1/n$). Scrubbing, by setting up additional circulation of the uranyl nitrate, brings the extraction section of the transfer unit closer to the critical mode of operation; the ratio of process flows of phases $n_0 = V/L_0$ must be increased slightly compared to extraction without scrubbing: $n_0 = f(n', \eta)$.

The performance of a tower for solvent recovery of uranium and plutonium (Fig. 3b) is viewed similarly. It is interesting that, at large flow ratios ($n > 10$), a sharp increase in acid concentration on the last plates leads to the uranium being displaced by the acid, i.e., to internal circulation of the uranyl nitrate.

LITERATURE CITED

1. I. K. Flanary, Report No. 539 (Geneva Conference, 1955) Vol. 9.
2. A. M. Rozen and L. P. Kharkhorina, Zhur. Neorg. Khim. 2, 1956 (1957); A. M. Rozen, Atomnaya Énergiya 2, 445 (1957).**
3. A. M. Rozen and E. I. Moiseenko, Zhur. Neorg. Khim. 4, 1209 (1959).

** Original Russian pagination. See C. B. translation.

A NEW GRAPHICAL AND ANALYTICAL METHOD FOR CALCULATING THE DOSE FIELD OF EXTENDED SOURCES

A. V. Bibergal'

Translated from Atomnaya Énergiya, Vol. 7, No. 3, pp. 281-284, September, 1959
Original article submitted March 4, 1959

In the solution of a number of problems encountered in the design of powerful γ facilities for radiation processing of objects and in the design of radiation shielding, the dose field of sources of different (and sometimes complex) configurations must be determined.

Exact solutions are available only for the simplest types of extended sources [1, 2], some of which are of no practical interest. For several other cases of practical interest, nomograms have been developed or auxiliary coefficients have been determined through numerical integration of the equations derived for the dose rate [3-5].

Up to the present, there is no generally applicable method of calculating the dose field of extended sources which would make it possible to carry out the analysis in any desired case (in a homogeneous medium or in its absence) to some exactly determined approximation.

The method proposed for calculating the dose field of extended sources makes it possible to dispense with numerical integration, and to obtain approximate expressions, with a desired degree of accuracy, in elementary or tabulated functions. We shall consider this method in the light of examples of calculations of source configurations of practical interest which have no generalized solutions up to the present writing.

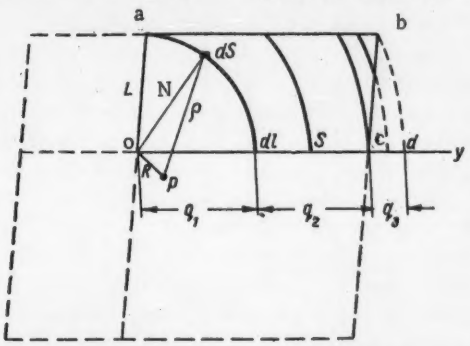

Fig. 1. Transition from a rectangular planar source LS with constant surface activity q to a fictitious linear source O d = J with variable specific linear activity over different segments: $Oy_1 \leq L \ldots q_1$; $L \leq y_2 \leq S \ldots q_2$; $S \leq y_3 \leq \sqrt{L^2 + S^2} \ldots q_3$.

Infinitely thin rectangular plane of finite dimensions. In order to calculate the dose rate at any point p found over a planar rectangular source, outlined in Fig. 1 by a dashed line, it is sufficient to find the dose rate due to a rectangular segment Oabc of the source, having dimensions L and S for any relationship of the sides.

Let the distance of the point p from the radiating plane be R, and let the specific surface activity be q, the width of segment Oabc be S = nL ($n \geq 1$). All elements of the plane segment which are found at some equal distance ρ from the point p make the same contribution at that point to the dose rate, and may be replaced by a source dl found at the distance ρ, but exhibiting an activity equal to the sum of the activities of the replaced elements dS.

In other words, the dose rate which is established at point p by the segment Oabc may also be derived from a linear source Od of length J, having an activity distributed in obedience to some law along the length of the source (cf. Fig. 2). The total activity of the linear source J will then be equal to the total activity of the segment Oabc.

We shall find out how the activity is distributed along the length of the fictitious linear source J.

The elements of the plane which are found at some uniform distance from the point p lie on arcs of circles of radius r, described from a point O (Fig. 1). The linear specific activity of the source J at each

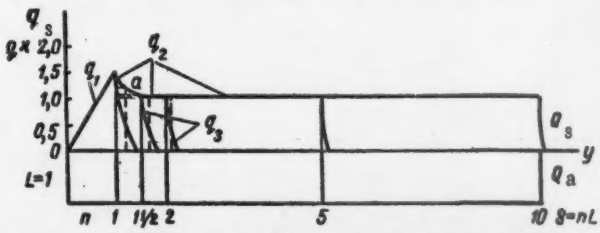

Fig. 2. Distribution of specific linear activity along fictitious linear source, for different ratios of the sides S/L = n of the planar rectangular source replaced.

point of the source is proportional to the length of the corresponding part of the arc sweeping over the area of the segment Oabc of the planar source.

At first, the linear specific activity increases over the interval of the linear source $O \leq y \leq L$, in obedience to the rule

$$q_1 = q\frac{\pi}{2}y. \qquad (1)$$

The linear specific activity over the segment $L \leq y \leq S$ then drops off according to the law

$$q_2 = qy \operatorname{arctg} \frac{L}{\sqrt{y^2 - L^2}}. \qquad (2)$$

From the point y = S to the point $y = \sqrt{S^2 + L^2} = J$, the linear specific activity drops off to zero, obeying the law

$$q_3 = qy\left[\operatorname{arctg}\frac{L}{\sqrt{y^2-L^2}} - \operatorname{arctg}\frac{\sqrt{y^2-S^2}}{S}\right]. \qquad (3)$$

Figure 2 depicts the distribution of the specific linear activity along the fictitious linear source, whose action at point p is equivalent to the action of a segment Oabc of the planar source equivalent. The diagram shows how the distribution of the activity varies as the ratio S/L = n is increased.

For q_2 and q_3, we may assume a linear distribution pattern to hold. We then obtain

$$q_1 = q\frac{\pi}{2}y = ay \text{ for } O \leqslant y \leqslant L.$$

In place of q_2 and q_3, let us take

$$q_2' = q\frac{S+\sqrt{L^2+S^2}}{2} \times \operatorname{arctg}\frac{L}{\sqrt{\left(\frac{S+\sqrt{L^2+S^2}}{2}\right)^2 - L^2}} = qc \qquad (4)$$

for

$$L \leqslant y \leqslant \frac{S+\sqrt{L^2+S^2}}{2}.$$

The mean error in a linear approximation following (4) is 2-5% depending on the source parameters and source geometry.

The dose rate from the segment Oabc of the planar finite source in air will be

$$\mathcal{P} = K_\gamma q\left\{\frac{\pi}{4}\ln\frac{L^2+R^2}{R^2} + \frac{C}{R}\left[\operatorname{arctg}\frac{S+\sqrt{L^2+S^2}}{2R} - \operatorname{arctg}\frac{L}{R}\right]\right\}. \qquad (5)$$

A check was carried out on (5) by comparing results with a nomogram generalizing the results of analysis by numerical integration, which was in turn performed for several values of the sides ratio of the segment Oabc [3]. Agreement was found to be within the experimental limits of error in the determination of the values on the nomogram for all values of R/S and L/S for which the nomogram was constructed.

When the planar source was placed in an absorbing medium, with multiple scattering taken into account, the dose rate due to segment Oabc was determined from the equation

$$\mathcal{P} = K_\gamma q\left\{-\frac{\pi}{2}\left(A_1\left[E_i(-b_1) - E_i\left(-b_1 \sec \operatorname{arctg}\frac{L}{R}\right)\right] + A_2 \times \left[E_i(-b_2) - E_i\left(-b_2 \sec \operatorname{arctg}\frac{L}{R}\right)\right]\right) + \frac{C}{R}\left[A_1 \int_0^{\operatorname{arctg}\frac{S+\sqrt{L^2+S^2}}{2}} e^{-b_1 \sec\varphi}\,d\varphi + A_2 \int_0^{\operatorname{arctg}\frac{S+\sqrt{L^2+S^2}}{2}} e^{-b_2 \sec\varphi}\,d\varphi - A_1 \int_0^{\operatorname{arctg}\frac{L}{R}} e^{-b_1 \sec\varphi}\,d\varphi - A_2 \int_0^{\operatorname{arctg}\frac{L}{R}} e^{-b_2 \sec\varphi}\,d\varphi\right]\right\}. \qquad (6)$$

Figure 3 shows the variation in radiation dose rate at a distance R = 50 cm along the axes of a rectangular planar source 200 × 100 cm, having a specific surface activity a = 1 mg-equiv/cm^2 in air and in an absorbing medium (water). The presence of an absorbing and scattering medium not only lowers the dose rate, but also equalizes the dose field at the same time over the planar source.

Planar source in elliptic form. A calculation of the dose rate in air and in an absorbing medium for a radiation source in the form of a disk, for a point located above the center of the disk, may be found in the literature [2]. We now derive the equation for the more general case, where the source has the form of an ellipse with any assigned eccentricity. Let there be given an ellipse with semimajor axis a and semiminor axis b (see Fig. 4). The distribution pattern of

the activity along the fictitious linear source over the interval $0 \leq \rho \leq b$ is

$$q_1 = 2\pi q\rho \qquad (7)$$

(where q is the specific activity associated with a unit area of the ellipse).

For the interval $b \leq \rho \leq a$, we get

$$q_2 = 4\rho\alpha q,$$

where

$$\alpha = \arctan\frac{y}{x} = \arctan\left[\frac{\delta}{a}\sqrt{\frac{a^2-\rho^2}{\rho^2-\delta^2}}\right]$$

$$\text{и } q_2 = 4\rho q \arctan\left[\frac{\delta}{a}\sqrt{\frac{a^2-\rho^2}{\rho^2-\delta^2}}\right]. \qquad (8)$$

Figure 5 shows the distribution of activity along a fictitious linear source of length a = 1 for the three cases: a = b, a= 2b and a = 10b. When $a \neq b$, a linear approximation is possible in the form

$$q_2' = \frac{a-\rho}{a-b}\,2\pi\delta q. \qquad (9)$$

The total activity of the linear source then remains equal to the total activity of the ellipse. The distribution of activity at a remote part of the source is the only activity distribution to vary somewhat. Utilizing (7) and (9), we obtain, for a source in air

$$\mathcal{P} = \pi K_\gamma q\left\{\ln\frac{R^2+b^2}{R^2} + \frac{2b}{a-b}\times\right.$$
$$\left.\times\left[\frac{a}{R}\left(\operatorname{arctg}\frac{a}{R} - \operatorname{arctg}\frac{b}{R}\right) - \frac{1}{2}\ln\frac{a^2+R^2}{b^2+R^2}\right]\right\}. \qquad (10)$$

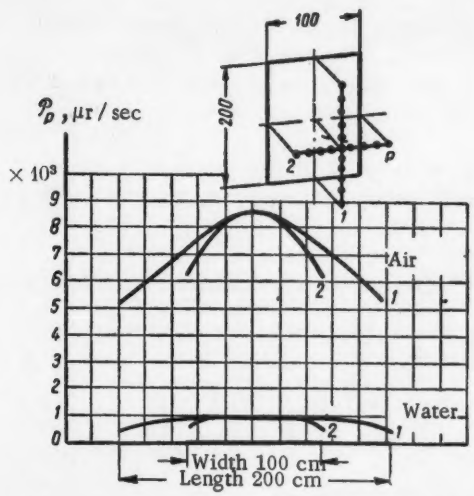

Fig. 3. Distribution of dose rate over a planar rectangular source (Co^{60}) in air and in an absorbing medium.

For a source placed in an absorbing medium

$$\mathcal{P} = -2\pi qK_\gamma\left\{A_1\left[E_i(-b_1) - E_i\left(-b_1\operatorname{secarctg}\frac{b}{R}\right)\right]\right.$$
$$\left. + A_2\left[E_i(-b_2) - E_i\left(-b_2\operatorname{secarctg}\frac{b}{R}\right)\right]\right\} +$$
$$+ 2\pi qK_\gamma\frac{b}{a-b}\left\{\frac{a}{R}\left[A_1\int_{\operatorname{arctg}\frac{b}{R}}^{\operatorname{arctg}\frac{a}{R}} e^{-b_1\sec\varphi}d\varphi + \right.\right.$$
$$\left.\left. + A_2\int_{\operatorname{arctg}\frac{b}{R}}^{\operatorname{arctg}\frac{a}{R}} e^{-b_2\sec\varphi}d\varphi\right] +\right.$$
$$+ A_1\left[E_i\left(-b_1\operatorname{secarctg}\frac{b}{R}\right) - \right.$$
$$\left. - E_i\left(-b_1\operatorname{secarctg}\frac{a}{R}\right)\right] +$$
$$+ A_2\left[E_i\left(-b_2\operatorname{secarctg}\frac{b}{R}\right) - \right.$$
$$\left.\left. - E_i\left(-b_2\operatorname{secarctg}\frac{a}{R}\right)\right]\right\}. \qquad (11)$$

Linear sources. The method of calculations proposed here may be used to find the equivalent sources which are placed differently with respect to the point where measurements are taken. Let there be a given linear source L with a constant specific activity q over its entire length. We shall now find the linear source l, placed perpendicular to the first (Fig. 6a, b), which is equivalent to it with respect to the dose rate established at the point p. The linear specific activity q_1 of this new source is a variable.

From Figure 6, we have

$$d\rho = dx = dy\sin\varphi = \frac{\sqrt{(x+R)^2-R^2}}{x+R}\,dx.$$

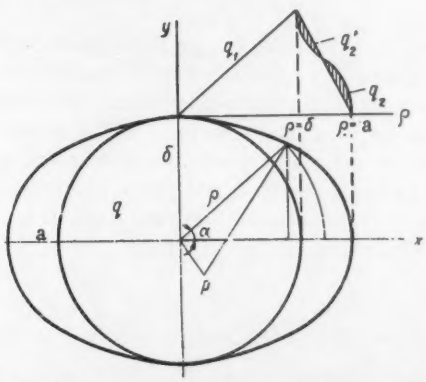

Fig. 4. Change from plane elliptic source with with a constant specific activity to a fictitious linear source, with the variable distribution of activity along the source.

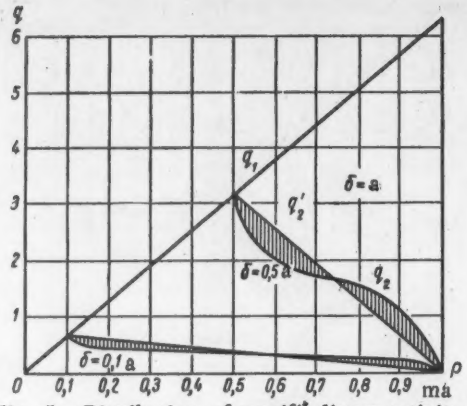

Fig. 5. Distribution of specific linear activity along a fictitious linear source for different ratios b/a = m (m ≤ 1).

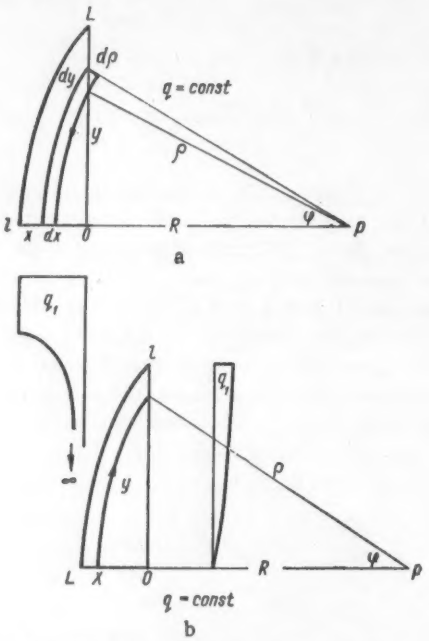

Fig. 6. Transition from a linear source with uniform activity distribution to a linear source with irregular activity distribution, the second placed perpendicular to the first: a) transition from a source placed along the x axis to a source placed along the y axis; b) transition from a source placed along the y axis to a source placed along the x axis.

Since

$$qdy = q_1 dx,$$

then

$$q_1 = q\frac{x+R}{\sqrt{(x+R)^2-R^2}}.$$

Equation (12) yields the distribution pattern for activity along the length of source l.

Let there now be given a linear source of length L laid out along the x axis, and having a uniform activity distribution pattern.

The source of length l equivalent to it, and placed along the y axis, will exhibit a specific linear activity obeying a distribution law

$$q_1 = q\frac{y}{\sqrt{R^2+y^2}}. \qquad (13)$$

Conclusion. The method proposed makes it possible to find approximate equations for the dose rate due to planar sources of different configurations, and the equivalent linear sources, with respect to dose rate, at a given point, and placed in different arrangements with respect to the first source. It would apparently be of some interest to extend this method to apply to three-dimensional sources.

LITERATURE CITED

1. T. Rockwell, Reactor Shielding Design Manual (Van Nostrand, Princeton, N. J., 1956).
2. G. V. Gorshkov, γ Radiation Emitted by Radioactive Objects. (Izd. Leningrad. Gos. Univ., 1956).
3. E. E. Kovalev, V. I. Popov, and L. N. Smirennyi. Atomnaya Énergiya 2, 181 (1957). *
4. I. A. Kalinin and P. Ya. Vertebnyi, Zhur. Fiz. Khim. 32, 2192 (1958).
5. E. E. Kovalev, Atomnaya Énergiya 2, 538 (1957). *

*Original Russian pagination. See C. B. translation.

SIXTH SESSION OF THE LEARNED COUNCIL OF THE JOINT INSTITUTE OF NUCLEAR STUDIES

M. Lebedenko

The sixth session of the Learned Council of the Joint Institute for Nuclear Studies met at Dubna from May 27 through June 2, 1959. Leading specialists in the field of nuclear physics came from 12 socialist countries to participate in the work of the session.

The delegations of the member nations of the Institute were headed by Petrik Pilika (Albania), Georgi Nadzhakov (Bulgaria), Albert Konya (Hungary), Le Van Thiem (Viet Nam), Heinz Barwich (German Democratic Republic), Tsien San-tsiang (China), Kim Hung Bong (Korea), Sodnom Namsrain (Mongolia), Andrzej Soltan (Poland), Horia Hulubei (Rumania), Cestmir Simane (Czechoslovakia), V. I. Veksler, N. N. Bogolyubov, and V. P. Dzhelepov (USSR). The chair was shared in succession by D. I. Blokhintsev, Director of the Joint Institute, and Vice-Directors Wang Hang-chang and E. Dzhakov.

Blokhintsev reported to the Council on the most significant research efforts brought to completion in the Institute's laboratories during the past half-year. Some of this work, in line with the decisions reached at the session, will be reported at the international conferences scheduled to meet at Kiev (on high-energy physics) and Geneva (on particle-accelerator engineering and related experimental techniques). Wang Hang-chang delivered a report on the development of international liaisons between the Institute and scientists in other lands.

The opening of the sixth session of the Learned Council coincided with the introduction into service of the new and splendidly equipped building housing the Laboratory of Theoretical Physics, where indeed the session was convened for a good part of the time. Members of the Learned Council heard reports on particular experiments of highest interest performed by a scientific staff of the Institute which is drawn from many nationalities. Some of those experiments produced new data on the structure of nucleons and on the production of mesons and antiparticles. Interesting experimental data were obtained using the proton synchrotron, in the work of a team of physicists headed by Wang Hang-chang and I. V. Chuvilo. Tens of of thousands of plates which they took will be useful in the further study of phenomena observed in interactions between pions and nucleons, and in the generation of "strange particles." New phenomena in the field of the decay of π-zero mesons was reported by a team of experimental researchers working in the Laboratory of Nuclear Problems.

The members of the Learned Council noted that many of the research efforts completed at the Laboratory of Theoretical Physics were in close correspondence with experimental observation.

In the resolution adopted by the sixth session of the Learned Council, it was noted that the achievement of round-the-clock and reliable operation of the proton synchrotron under the conditions for which it was designed is a signal accomplishment to be credited to the staff of the High-Energies Laboratory, and that it has made it possible to develop experimental work on a broad scope within a short period. The Learned Council singled out as one of the most noteworthy achievements in the field of advanced accelerator design the development and commissioning, at the Laboratory of Nuclear Problems, of an accelerator incorporating spatial variation of the magnetic field.*

The sixth session of the Learned Council pointed out that the Joint Institute, which was founded only three years ago, has already become a powerful research center occuping one of the foremost places in the vanguard of world science.

---

* D. P. Vasilevskaya et al., Atomnaya Énergiya 6, 657 (1959) [Original Russian pagination. See C. B. translation].

FOURTH SCIENTIFIC AND TECHNICAL CONFERENCE ON NUCLEAR ELECTRONICS

The IV Scientific and Technical Conference on Nuclear Radioelectronics, organized by the Main Control Board on the Uses of Atomic Energy, met in Moscow on April 20-25, 1959. Over 800 specialists from scientific research and industrial organizations of the Soviet Union participated in the conference.

Over 100 reports and communications were heard, covering research work in the field of design of sophisticated electronic equipment for experimental nuclear physics and nuclear engineering, and also covering instrumentation already designed and made available by industry.

The conference was opened by P. S. Savitskii.

Panel sessions were convened on particular topics such as nuclear radiation detectors, pulse-height analyzers and time analyzers, pulse equipment, automation of measurments and data processing, spectrometers, voltage and current amplifiers, and voltage and current stabilizers.

The major attention of the panel session on nuclear radiation detectors was devoted to scintillation techniques in radiation research, and to the design of appropriate instrumentation. In particular, questions touching upon the design of new electronic phototube multipliers for scintillation spectrometers and for recording pulses in the decinanosecond (10^{-10} sec) range were discussed, as were problems associated with the design of detectors of ionizing radiations with high efficiency in recording and high resolution, including plastic, gaseous, liquid, and hybrid scintillators.

Several reports dealt with research on the parameters of scintillators and phototube multipliers (stability and pulse-height discrimination in photomultipliers), the effect of crystal parameters on pulse-height discriminations, the choice of crystal-photomultiplier tube systems for a scintillation spectrometer, etc. A special subpanel session took up questions regarding fast neutron spectrometers and neutron detectors.

The panel session on pulse-height analyzers and time analyzers heard papers on the design of multichannel amplitude and time analyzers and their subassemblies and associated circuitry (readout instuments, memory storage, etc.), methods for decreasing resolving time in pulse-height analyzers, etc.

A significant number of the reports were devoted to the development and design of multichannel systems (a 1000-channel amplitude-time analyzer, a 1024-channel time analyzer with magnetic-drum memory, a 50-channel analyzer, etc.).

The panel session on automation of measurements and data processing heard reports on the extraction of data from multichannel analyzers with the aid of automatic printout devices, on the design of output digital printout devices for multichannel analyzers, automatic facilities for measuring activity in preparations, etc. One paper was devoted to an arrangement for semiautomatic processing of photographic plates of tracks in bubble chambers, a design worked out at the Institute of Theoretical and Experimental Physics of the Academy of Sciences of the USSR, and a design project for an automatic arrangement for the same purposes.

The panel on pulsed equipment devoted its sessions to papers dealing with the design of circuits and assembly units in pulsed equipment.

The spectrometer panel considered reports dealing with several developed spectrometer facilities.

The panel on voltage and current amplifiers and voltage and current stabilizers heard papers on stabilized power supplies which had been developed (using transistors), electrometer amplifiers in rod-lamps, etc.

The concluding plenary session was devoted to problems such as the radiation stability of semiconductors and standard radioactive sources for the monitoring and calibration of radiometric equipment.

The participants in the conference adopted a resolution envisaging the development of research and experimental work on the design of electronic equipment for nuclear physics studies.

An exposition on display during the conference demonstrated samples of electronic equipment designed at research establishments and produced by domestic industry, and also several specimens of foreign equipment.

On display were pulse-height analyzers, time analyzers, scintillation spectrometers, scalers, coincidence circuits, phototube multipliers, scintillators, and other equipment.

Below, we present a brief rundown of the characteristics of some of the specimens on display.

Automatic AZ-1 single-channel self-recording analyzer for automatic measurements of the energy spectra of radioactive radiation, and for automatic measurements of α-, β-, γ-radiation in large quantity from standard smaples (targets). The instrument records pulses of negative polarity with a rise time of from 0.01 to 1 μsec. The range of input pulses is from 0.01 to 25 v. The window has a width of 2.4. Irregularities in window width are ~ 1%. The resolving time is 5 μsec. The analyzer is equipped with a printing recorder. The time for recording a single result is 2.5 sec. The analyzer may be operated in two modes: the number of pulses per exposure may be measured, or the time corresponding to a given number of pulses may be measured. An automatic sample shift device is built to handle 40 samples.

Automatic AZA-2Ts single-channel pulse-height analyzer for measuring the spectra of radioactive radiation and for the automatic measurement of radiation intensity (assembled with an automatic sample changer capable of accomodating 50 samples). Recording of the measurement data is handled by a printing recorder. The amplitudes of input pulses range from 0.01 to 40 volts (11 range levels). Window width is 2.4. Resolving time is 5 μsec. Time of exposure lasts from 0.4 to 1,000 sec. There is a high-voltage power supply unit for the photomultiplier part. The instrument is made in the form of a stand. Power intake is 230 va, and the instrument weighs 75 kg.

Differential single-channel ADOI-3 analyzer with rate meter for measurements of energy spectra. A scintillation detector is used in the instrument. The resolving time is 8 μsec. The amplitudes of input pulses range from 0.25 to 25 v (11 ranges). Window widths are 1, 2, 5. The thresholds vary stepwise from 1 to 10%.

AIMA-2 pulse-height analyzer with 50 or 80 channels. The capacity of each channel is 2^{16} pulses in operation using 50 channels, and 2^{10} pulses in operation using 80 channels. Resolving time is 1.3 μsec. The input pulse amplitudes range 0-50 v. Peak duty factor of the analyzer is 5000 pulses per sec. Memory storage of the number of pulses in each channel is handled by a magnetic drum. The measurement data are displayed on a dual-beam screen, in binary and linear scales. There exists the possibility of analyzing only those pulses which are time-coincident with the control pulse. Resolving time for the coincidence circuit is 1.5 μsec.

BMA-50-channel pulse-height analyzer for automatic measuring of energy spectra of elementary particles and other products of nuclear interactions (Fig. 1). Channel widths are 0.2, 0.3, 0.5, 1.0, and 2.0 v: Range of pulse amplitudes 0.01-100 v. Resolving time 0.182 μsec: Capacity of each channel 16,000 pulses: Maximum counting rate 50,000 pulses/sec: Range of durations of input pulses 0.1-1000 μsec. The analyzer is equipped with a rate meter, dead-time indicator, monitoring pulse generator for calibration purposes, high-voltage rectifier for power delivery to the phototube multipliers, and a detachable cathode-follower circuit, as well as a preamplifier unit for reducing channel width and threshold by 20 times. Provisions are made for automatic switching of the analyzer to handle 8000 or 16,000 pulses in either channel, as desired. The analyzer circuitry incorporates about 1500 cold-cathode tubes and about 200 thermionic tubes. Analyzer operation may be gated by an external selector or without it.

AI-100 100-channel pulse-height analyzer using a ferrite-core memory for determining the amplitude spectrum of pulses distributed statistically in time (see Fig. 2.). Channel width instability is ± 1.5%: Channel width 1 v: Capacity of each channel 15,999 or 65,535 pulses: Range of input pulse duration 1-100 μsec: Average counting rate 10,000 pulses/sec: Average dead-time 70 μsec. The analyzer contains an amplifier (for amplifying pulses of 0.01-1 v), a rate meter with measurement ranges of 1000; 3000; 10,000; and 30,000 pulses per sec with an accuracy of ±10%. When any one channel is fully loaded, the analyzer is blocked; pulses beyond the hundredth channel are not recorded. The counting system uses a binary-decimal arrangement.

1024-channel time analyzer for operation in a neutron selector system over a broad range of energies, with high-intensity pulsed neutron flux. The analyzer is capable of handling an input duty cycle of up to 10,000 pulses per sec. Channel-width steps are 1, 2, 4, 8, 32 μsec. All the channels can be broken down into four groups (of 256 channels each). Each group may be assigned a different channel width. To secure a dead time of 1 μsec, a special intermediate memory unit is introduced into the analyzer circuitry, to keep counting losses at peak duty factor from exceeding 1.7%. The basic memory storage in the analyzer is based on magnetic cores. The maximum capacity of each channel is 2^{16} pulses. Measurement data may be presented on a linear scale in a CRT display either during the measurements or afterward. Definitive measurement data are printed out. The data are punched out on paper tape, with channel number indicated. Printing speed is 12 characters per second. Numerical values in binary coding may be obtained by reference to the display devices of the adding circuit in the basic memory unit.

GSP table-model γ spectrometer for measuring radioactive radiation spectra. The spectrometer incorporates a pulsed amplifier, a single-channel differential and integral analyzer, scaler, rate meter, monitoring integral discriminator, and a stabilized

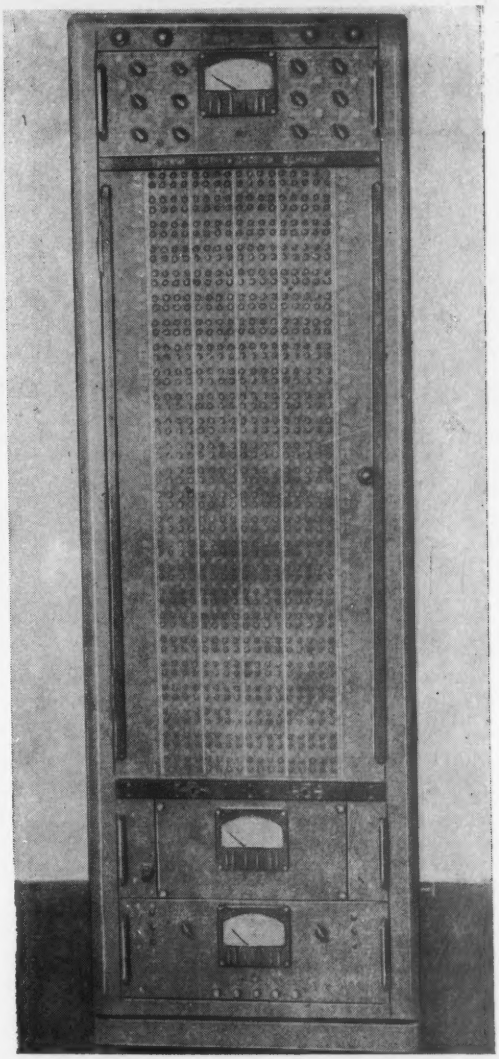

Fig. 1. 50-channel pulse-height analyzer, BMA-50.

positive voltage source rated at 0.7-2 kev. Input pulse heights range 0.01 to 25 v. Resolving time of the spectrometer is 5 μsec, and the capacity is 16,000 pulses.

PS-5 scaler for counting pulses with peak pulse repetition rate of 80,000 pulses per sec (Fig. 3). The scaler assembly includes a scaling unit, high-voltage rectifier, detachable cathode-follower circuit, gas-filled counters section and photoelectronic multiplier unit. The resolving time for binary pulses is 10μsec, and channel capacity 10^{16} pulses. The scaler is operated by gating with pulses of 0.5-10 μsec duration and 3 to 100 volts amplitude. Ranges of measurement are 1000, 10,000, and 100,000 pulses per second. The instrument reads to an accuracy of ± 10%. Data are read by neon glow-tube and dekatron indication. An electronic second-timer allows time intervals of up to 1000 sec to be read off. Counting may be halted and the electronic second-timer inserted after accumulating 10^3, 10^4, or 10^5 pulses, or after a time interval of 1, 10, 100, or 1000 sec has elapsed. The stabilized high-voltage rectifier provides a voltage of 400 to 2000 v across the output at a current of up to 3 ma. In response to a variation of ± 10% in network voltage, the output voltage varies by not more than ± 0.2%. The section containing gas-filled counters may be operated with any industrially available counter. The photoelectronic multiplier unit is designed for operation with the FÉU-19M photomultiplier tube.

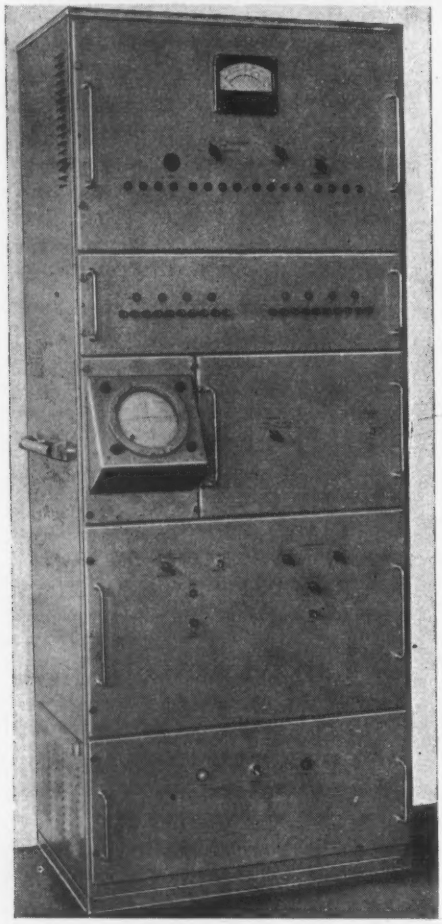

Fig. 2. 100-channel pulse-height analyzer with ferrite-core memory units, AI-100.

PS-0.1 scaler for counting pulses exhibiting a random time distribution (Fig. 4). This instrument is one of the units in a general-purpose "line" of instruments designed for nuclear research, and having a resolving time of 0.1 μsec. Channel capacity is 10 pulses. Sensitivity is from 5 to 30 v (regulated in steps of 5 v each), and the scaling system used is a scale-of-ten.

BDS-1 double-coincidence instrument (Fig. 5). This instrument, with two channels at its disposal, operates with two general-purpose scintillation transducers and places a pulse across the output if the pulses received from the transducers fall within a specified time interval. The instrument is gated from negative pulses of 3 v amplitude and higher, and of 10^{-8} sec duration. The minimum resolving time is 10^{-8} sec, and the resolving time may be varied from 10^{-8} to 10^{-7} sec. One of the channels is provided with a variable delay line of $0\text{-}10^{-7}$ sec. The instrument can handle a duty factor of 10^5 pulses per sec and may be operated as a time analyzer.

UIS-1 spectrometric non-overloading pulse amplifier for amplifying pulses arriving from scintillation transducers with NaI(Tl) crystals. A preamplifier (K = 10), mounted in the form of a separate unit housed inside the instrument, may be coupled to the main amplifier, if it is required to amplify pulses of ~ 10 mv. The amplifier consists of a power supply unit, a main amplifier, and the preamplifier. The maximum gain factor, with the preamplifier hooked in, is 10,000, and is 1000 without the amplifier. Pulse rise time is 0.2 μsec. Peak linear output signal is 100 v. Duty factor is 10^5 pulses per sec. The integral nonlinearity is ~ 1% (for a capacitive load of

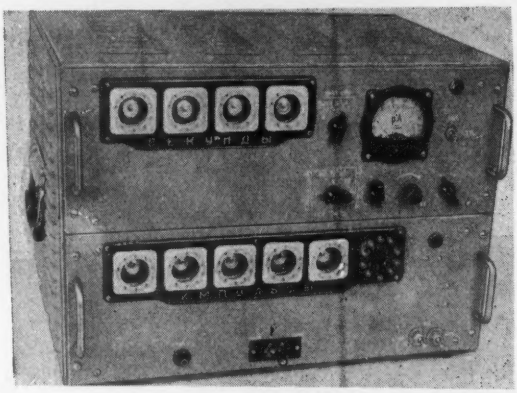

Fig. 3. PS-5 scaler.

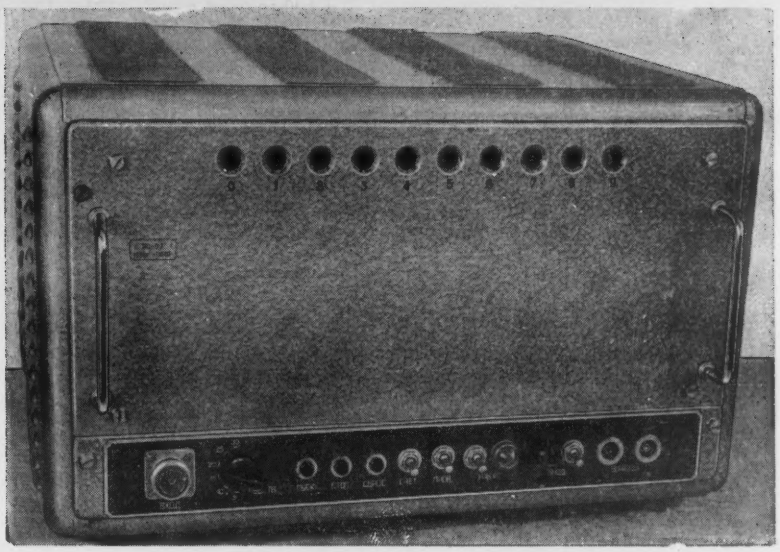

Fig. 4. PS-0.1 scaler.

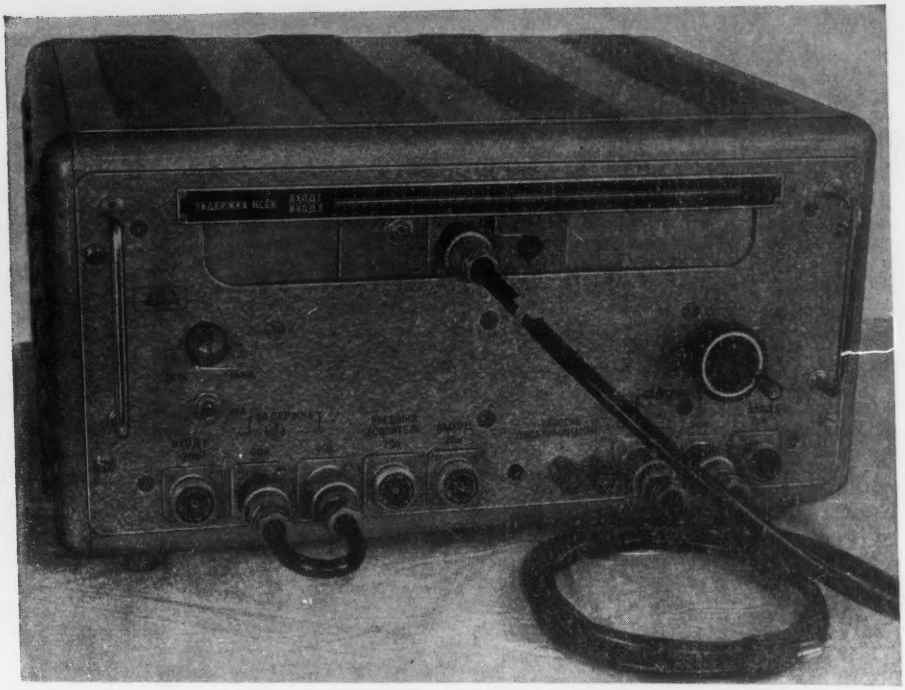

Fig. 5. BDS-1 double-coincidence instrument.

50-60 $\mu\mu$f). Gain instability is less than 1% for 8 hr of continuous operation, when the network voltage varies by ± 10%. Input and output pulses are of positive and negative polarity.

The RV timer is used for setting exact time intervals, and as a time-pulse oscillator. The timer is capable of setting 22 exposure times lasting anywhere from 10 sec to 12 hrs, with exposure-time error not in excess of 0.5%. Duration of time pulses 5-10 μsec, Amplitude 25-50 v.

SVV-9 miniaturized stabilized high-voltage rectifier as power supplies for from one to three photomultiplier tubes. The output stabilized voltage is negative. Provisions are made for stepwise voltage variations

from 0.8 to 2 kv, using a stepping switch (11-position switch) and slide-wire potentiometer. Load current may reach 2 ma; 0.04% instability in response to network voltage oscillations of ± 10% or load current swings from 0 to 2 ma. The ripple factor is 0.004-0.01%.

Photoelectronic multiplier tubes of various designs and types (spectrometric phototubes, timing phototubes) for working with directed light flux, and other photomultiplier types: Photomultipliers with phtocathodes ranging up to 250 mm in diameter were put on display.

Scintillation detectors using thallium-activated NaI, measuring up to 150 mm in diameter and up to 60 mm in height, CsI(T1) crystals 80 mm in diameter and 25 mm in height, anthracene crystals 40 mm in diameter and 20 mm in height, plastic scintillation phosphors based on polystyrene with PTP+POPOP additive, measuring up to 200 mm in diameter and up to 150 mm in height, etc.

Instruments for testing and tuning electronic equipment and for taking their characteristics (oscillators, amplifiers, quartz-crystal calibrators), vacuum-tube voltmeters, etc), were put on display, including the GKI-5 millimicrosecond-range square-wave generator, which yields pulses lasting 7-500 millimicroseconds (17 values) with amplitudes ranging from 0 to 250 v and rising wavefront lasting 5-6 m μsec; the GITA-3 pulse generator, which produces pulses ranging 0 to 200 v in amplitude, with a pulse repetition rate of 50 cps, square-wave pulse duration of 2 μsec, minimum rise time 10^{-8} sec, and pulse height stability of 10^{-3} to 10^{-4}; the GMI-1 millimicrosecond-range pulse generator, producing pulses of positive and negative polarity having amplitudes up to 45 v and durations ranging from $3 \cdot 10^{-9}$ to $1.5 \cdot 10^{-8}$ sec, rising wavefront $1.5 \cdot 10^{-9}$ sec, and pulse repetition rate of 50-6000 cps; the 4E-2 electronic frequency meter designed for automatically measuring frequencies of electrical oscillations, pulse repetition rates in the 10 cps to 10 Mc range of frequencies, measurements of pulse cycle duration (starting from 100 μsec of higher), counting the number of electrical oscillations, measuring the duration of pulses and time intervals between pulses (longer than 10 μsec), etc.; the OS-4 high-speed oscillograph, with a sweep duration of 10 to 1000 m μsec (in 5 discrete values) having a time-marker pulse lasting 2, 10 and 50 m μsec, with vertical-deflection amplifier bandwidth of 1000 Mc.

Components and modular units used in the assembly and design of industrially available radio engineering and electronic equipment were displayed widely, these including: 10 standardized electronic circuit units, normalizers, signaling devices, constant voltage converters, trochotron starting stage, bipolar cathode-follower circuit, standard scaling circuit, electronic stabilizers, gas stabilizers, semiconductor rectifiers, etc.; 2) multipurpose components in the MTsIS digital measuring system(100-256 character memory units and matrices); 3) MnO_2-Zn storage battery systems, including the GB-120, GB-300, GB-5400, and GB-900 batteries, which provide voltages up to 1000 v and currents up to 100 μa (service life extending to 250 hr); 4) silver-zinc storage battery system includings the STsS-15, STsS-12, STsS-3, STsS-1.5, STs-0.5, and STs-0.1 batteries, all of which function as new electrochemical reversible current sources (specific capacity rating attains 100 w-hr per kg weight, peak capacity ranges from 0.12 to 16 amp-hr, with the weights of the batteries ranging respectively from 4.0 to 275.0 g); 5) alkali manganese-zinc batteries including the MTs-1K, MTs-2K, MTs-3K, and MTs-4K battery types, serving as power supplies for semiconductor equipment and other instruments (the capacity ratings of these batteries, for a voltage of 0.8 v and discharge current of 5 ma, extends from 0.13 to 1.15 amp-hr; as to the size of the batteries: height ranges from 6.6 to 9.6 mm, diameters from 15.8 to 30.3 mm, and weights from 4 to 20 g).

The Fourth Scientific and Technical Conference on Nuclear Electronics will contribute to the successful development of work in the USSR on devising sophisticated electronic equipment in the service of nuclear physics and nuclear engineering.

The proceedings of the conference will be published by Atomizdat in the form of a separate symposium in the book format.

L. P.

NEW ITEMS AT THE EXPOSITION IN THE "ATOMIC ENERGY FOR PEACEFUL PURPOSES" PAVILION

V. Orlov

(From the exposition of the achievements of the national economy of the USSR)

The "Atomic Energy for Peaceful Purposes" exhibition has been greatly expanded for 1959, and now occupies two full buildings.

The new building houses the following section of the exposition: "International Cooperation by the Soviet Union in the Field of the Peaceful Utilization

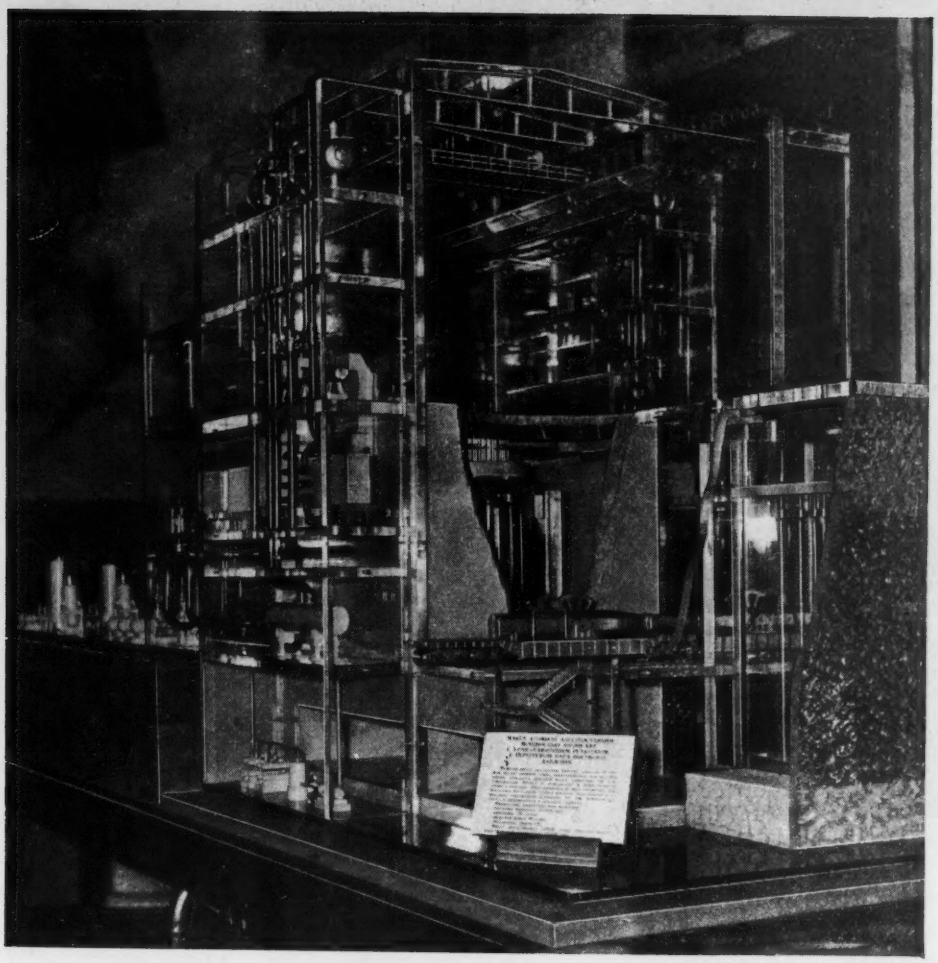

Fig. 1. Scale model of 400 Mw(e) nuclear power station.

of Atomic Energy, and the Joint Institute for Nuclear Studies," "Nuclear Power Engineering," and "Thermonuclear Research."

The "International Cooperation" section informs the visitor, by means of photographs, figures, and repeating newsreel shows, of the many aspects in which the Soviet Union is rendering technical aid and tendering scientific collaboration to other countries, in the training of specialists, in the building of nuclear research centers. Here, we see on display models of several reactors built by the Soviet Union in other countries. The activities of the Joint Institute for Nuclear Studies are illustrated,in particular,by the theme "Charged-Particle Accelerators." Illuminated moving-light display panels explain the operating principles of the synchrocyclotron and proton synchrotron, and a model of the 680 Mev synchrocyclotron is demonstrated. Some examples of nuclear research instrumentation are on display in the same hall.

Models and live display panels are also featured in the demonstrations of nuclear-electric power generating stations and particular nuclear reactors being planned, now under construction, or presently in operation: diagrams, a model,and the technological channel of the world's first nuclear-electric power station; a live panel and a scale model illustrating a 420 Mw atomic-electric power station powered by a water-cooled, water-moderated reactor; a live-panel and scale model of the 400 Mw uranium-graphite superheated-pressurized-steam reactor power station (Fig. 1); an electrified moving display panel of the 50 Mw (e) boiling-water-reactor nuclear power plant now being built; a diagram of a test reactor burning gaseous fuel; a moving panel of a fast reactor, and photographs, drawings, and diagrams of fast reactors BR-1, BR-2, BR-3, BR-5, and BN-50.

A scale model of the 150 Mw(e) nuclear power plant incorporating a gas-cooled heavy-water moderated reactor, located in the middle of the hall, was the center of much interest. The reactor will burn natural uranium fuel. The design of this power station was carried through by the joint efforts of

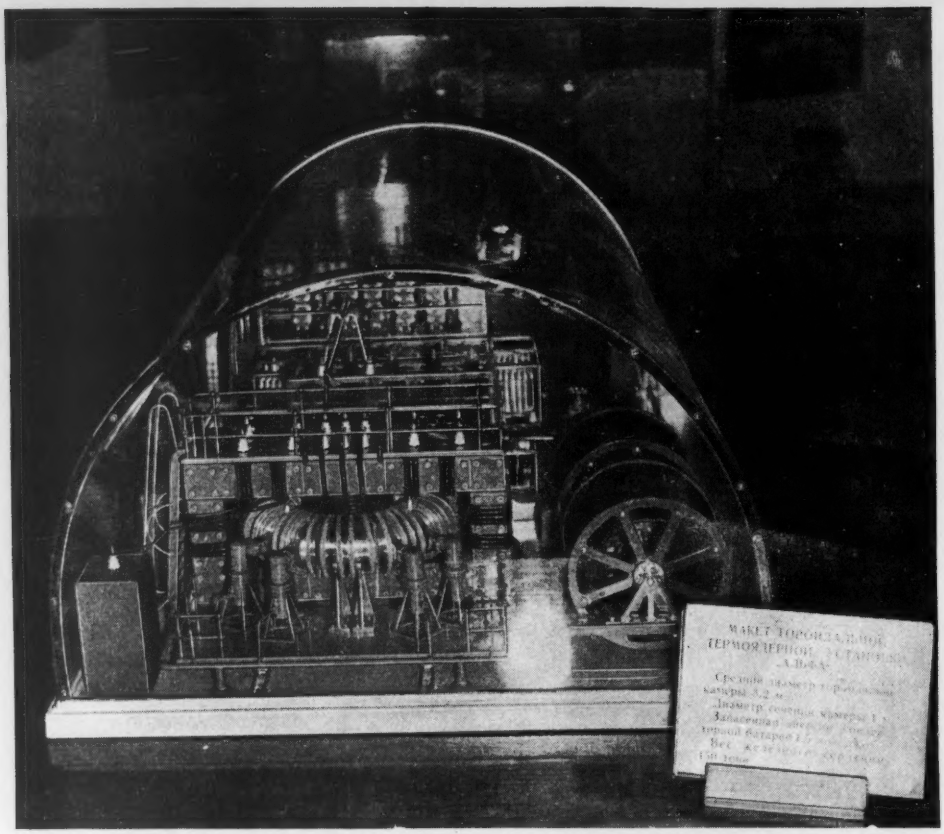

Fig. 2. Scale model of the "Alpha" toroidal thermonuclear facility.

Soviet and Czechoslovak specialists. A power station along these lines will be erected in Czechoslovakia.

A new section, "Thermonuclear Research in the USSR," has been added to the exhibits.

The exhibits in this section explain fusion reactions of light nuclei, and tell of the conditions required for achieving controlled thermonuclear reactions, and of the history of the development of research on controlled fusion reactions in the USSR.

The display illustrates three basic methods for obtaining a high-temperature plasma: pulsed processes, quasi-stabilized processes (charge stabilization by external magnetic field), and magnetic traps.

An operating pulse-discharge experimental facility with a ceramic discharge chamber is demonstrated in this section. A facility such as this was the one in which neutrons emitted in the gaseous discharge process were first produced at the Institute of Atomic Energy of the Academy of Sciences of the USSR, in 1952. A porcelain discharge chamber for a pulsed thermonuclear facility is also demonstrated here. Also demonstrated are scale models of the first adiabatic magnetic trap (scale 1 : 6), toroidal pinch chambers, arrangements in which a plasma ring is obtained in a transverse magnetic field, a magnetic adiabatic trap (scale 1 : 10), the "Alpha" toroidal thermonuclear machine (Fig. 2).

The publishing and publicity activities relating to exhibitions on the peaceful uses of atomic energy are reflected by an exhibit set up inside the lightweight-glass structure of the new building. The stands display books published in the USSR and abroad, trophies, scrolls, medals awarded to exhibits of the USSR; colored posters advertise periodicals and books put out by Atomizdat press, and Soviet "Atoms for Peace" exhibits in foreign countries. Literature published by Atomizdat is also placed on sale in that section.

Other sections of the pavilion have also been amply refurbished with new exhibits.

The section "The Atomic Nucleus and Related Research Techniques" has on display a facility which provides a graphic demonstration, to the visitors, of the penetrating power of various types of radioactive radiations, and the shielding properties of many materials.

The section "Raw Materials for Nuclear Power, and Materials Used in Reactor Design" has fathered a new topical subsection; "Working of Uraniferous Ore Deposits." The high level of techniques achieved in safety practices in underground, highly productive, sublevel methods, sophisticated methods for grading and classifying ores (radiometric beneficiation), shaft-head facilities, techniques for hydraulic dust suppression, etc. are shown.

Also on display are radiometers used in ore grading: the RSR-3 "Strela" ore-grading radiometer, designed for assay of ores in large yield (in hoppers and automatic-loading and hauling devices) by means of γ-ray emissions, and automatic classification of hoppers into groups depending on the content of radioactive metal; the RSU-T radiometric scintillation device, designed for express-analysis of ores by means of γ radiation, while the ores are in motion along the conveyor belt. The efficiency of the scintillation detector is 5-8 pulses/sec for 1 μr/hr. The resolving time is not longer than 15 μsec.

Several new logging and prospecting radiometers are also on display in this section:

Portable γ logging scintillation radiometer, PRKS, designed for measuring the intensity of radioactive emissions and evaluating the relative uranium and thorium content in ores directly at the ore deposits. The device may be operated under high-humidity conditions;

KRS logging scintillation radiometer, capable of logging cores down to 1000 m below ground. Besides measuring the magnitude of the intensity of γ radiations, the radiometer is capable of determining the relative uranium and thorium content in ores directly at the deposit site. The instrumental error over the 0-50°C temperature range is not in excess of 15%. The scintillation transducer is manufactured in hermetically sealed encapsulation;

"Rupor" ore-prospecting radiometer using gas-filled counters, available in two modifications: RPR-1 is designed for measuring the intensity of γ emissions under field or mine conditions and for logging boreholes to depths of 2 m, and RPP-1 is designed for the detection of the presence of radioactive ores, and also for measurements of the intensity of γ and β radiations from rocks under field conditions. The instrument is power-supplied by batteries. The weight of the entire portable assembly amounts to 3 kg;

"Kristall" SPR-2 prospecting scintillation radiometer, for recording γ radiations of energies above 50 kev, and hard β emissions. Sensitivity threshold is not higher than 2.2 μr/hr for a gamma background level of 8 μr/hr. The instrument is capable of operation over a range of temperatures from -20° to + 50°C and in 98% humidity. The entire weight of the assembly is 3 kg.

"Sputnik-1" companion portable prospecting radiometer, for detecting radioactive substances, and for qualitative and quantitative analysis with respect to γ and β emissions. The sensitivity threshold is not higher than 8 μr/hr for a gamma background of 15 μr/hr. The instrument is capable of operation over a range of temperatures from -10° to +40°C, and in 95 ± 3% humidity. Weight is 1.6 kg.

"Pioneer" pocket γ- and β-indicator for detection of radioactive emissions.

The section "Radiation Shielding and Health Physics" has been supplemented by a coverall of "lavsan" textile (distinguished by its heat stability, high mechanical strength, and stability to quite a few corrosive acids), the air-inflated overalls LG-4 made from polyvinyl chloride by a high-frequency welding technique, and used in work under hot conditions where the surrounding air and equipment is heavily contaminated with radioactive matter.

Some new instruments are on display in this section:

SU-1 automatically actuated alarm annunciator for monitoring of radioactive contamination (Fig. 3). This instrument is designed to sound an automatic alarm whenever the contamination on surfaces of the body or clothing by β- and γ-active substances exceeds safety levels. The sensitivity threshold is controlled within the range 0.03-3 μr/sec (with respect to γ emissions from Co^{60}). The alarm annunciator operates in the presence of a gamma background of up to 0.4 μr/sec, automatically compensating for the background;

RK-01 pocket dosimeter for measuring γ-and β-radiations in shops and laboratories, and under field conditions. The dosimeter circuitry is transistorized. The power is fed from a single 1 KSU-3 "Saturn" battery. It weighs 600 g. Error is within ±10%. The dosimeter can operate without recharging for 200 hr;

KPN-2 portable fast and thermal neutron radiometer. The instrument is equipped with three replaceable detectors, is capable of determining the intensity of fast neutron flux of energy ranging from 0.5 to 14 Mev, and is also capable of measuring thermal neutron

Fig. 3. Automatic alarm signaling device SU-1 for monitoring radioactive contamination.

flux intensity. The instrumental error does not exceed ± 20% of scale value. Power may be fed from the lines or from a STsS-5 battery;

IFK-1 assembly for determining the total γ-exposure dose obtained by personnel during the working day;

DFE-10 photoelectric densitometer for measuring the diffuse optical density of segments of a developed photographic layer on a transparent substrate;

IV-1 facility for measuring degree of contamination of water by β-active substances. The instrument is provided with an alarm system indicating whenever water contamination exceeds a previously set level. It is capable of exercising continuous monitoring control over contamination of water by radioactive substances. Instrumental error stays within ± 30% of nominal scale readings.

The section "Isotope Production" is attracting increased attention because of the graphically illustrated "Table of Radioactive and Stable Isotopes Produced in the USSR." Also on display are types of radioactive emission sources, internal packings, remote-control appurtenances for handling hot preparations, and a mock-up of a hot cell.

Other sections in the exhibit, "The Uses of Radioactive Isotopes in Industry," "The Uses of Radioactive Isotopes in Biology and Agriculture", and "The Uses of Radioactive Isotopes in Medicine" have also been supplemented with new displays.

BRIEF COMMUNICATIONS

USSR. In the Physics Institute of the Academy of Sciences of Armenian SSR an analyzer of pulse amplitudes has been developed, which employs logarithmic transformation for conversion of pulse amplitude into duration; owing to this, the measuring of pulses in all channels is realized with the same relative accuracy.

The analyzer was designed to be used with a five-layer proportional counter in the field of cosmic-ray study.

USSR. Tallinsk Experimental Plant of Instrumentation (Estonian SSR) has taken over manufacture of 12 types of instruments which are based on utilization of radioactive isotopes; the instruments are intended for the automatization of various processes in the metallurgical, chemical, mining, food and other branches of industry and transportation.

The first group of automatic regulators of level of petroleum products has been issued.

NEW LITERATURE

BOOKS, SYMPOSIA, PERIODICALS

Verkhovskii, B. I. The Use of Radioactive Isotopes in Process Control. Academy of Sciences Press, 1959, 83 pages, 1 ruble, 25 kopeks.

This book, in popular style, deals with the phenomenon of radioactive decay, the properties of radioactive radiation and methods for detecting radiations. Process control instruments based on the use of the penetrating power of radioactive radiation scattered by β- and γ-sources, or the ionizing power of radioactive radiation, and instruments utilizing neutron sources, are described.

D'yachenko, P. E. Moscow, Mashgiz, 1958, 215 pp. 8 rubles.

D'yachenko, P. E. Use of Radioactive Isotopes in Industry. Moscow, Mashgiz, 1958, 215 pages, 8 rubles.

General information is provided on radioisotopes, methods for detecting them and methods used in introducing them into the objects to be tested. Examples of the use of radioactive isotopes in technical laboratories and in industry are cited.

Weiss, K. F. Standard Radioactive Preparations. Translated from the German. Moscow, Fizmatgiz, 1958. 244 pages, 8 rubles, 45 hopeks.

This is a monograph treating of the properties and methods used in the manufacture and measurement of the absolute activity of standard radioactive preparations: γ standards of radium, radiothorium, actinium, Co^{60}, Cs^{137}, Na^{22}, Mn^{54}; β standards of Ra (D + E), ($U + UX_1 + UX_2$) and Tl^{204}; α standards of uranium, Pu^{239}, Po^{210}; a special section is reserved for the manufacture and calibration of neutron standards

The book is written for the wide readership of persons working with hot preparations.

Nukleonika (Poland). Vol. IV, No. 3 (1959). Janik, E. Scattering and Slowing Down of Neutrons by Bound Nuclei; Baran, W. Dependence of the Reactor Period on the Multiplication Constant Under Subcritical Conditions; Pinkas, K. Method for Studying Uranium Raw Materials of Domestic Origin and Results of the Method; Radoszewski, T. Absolute Methods for Measuring β and γ activity; Lesynski, J. GM Halide Counters; Pawlikevicz, J. Nuclear Facilities in the Merchant Fuel; Colloquium Sponsored by the Radiochemical Division of the Institute for Nuclear Research. Chronicle.

Journal of Nuclear Materials. April 1, 1959 saw the appearance of the first issue of "Journal of Nuclear Materials" (English title). The periodical will be devoted to problems of metallurgy, ceramics, and solid state physics in nucleonics applications. The periodical is being published in Amsterdam by the North Holland Publishing Co., and is, at the present time, a quarterly.

ARTICLES FROM THE PERIODICAL LITERATURE

N. K. Abrosimov, "On the cyclotron with a concave accelerating slit," Zhur. Tekh. Fiz. 29, 726-728 (1959).

V. S. Apastasevich, "Equilibrium conditions of electron beams," Zhur. Tekh. Fiz. 29, 738-744 (1959).

O. S. Andreeva and M. I. Lebedev, "Some β-radiation features in work with uranium metal," Med. Radiologiya 4, 58-62 (1959).

Yu. I. Belyakov and E. I. Agishev, "Use of a pulsed mass-spectroscope in studying the evolution of gas from metals," Zhur. Tekh. Fiz. 29, 796 (1959).

V. Kh. Vavilov et al., "Contribution on the performance of 'Atomic' current sources with double energy transformation," Fiz. Tverd. Tela 1, 826-827 (1959).

I. M. Verkhovskii et al., "Use of the radioactive isotope technique in studying the process of pneumatic beneficiation," Nauchn. Doklady Vyssh. Shkoly. Gornoe delo, No. 1, 215-219 (1959).

P. Vlasyuk, "Radioactive isotopes (and their use in agricultural engineering)", Nauka i Peredov. Opyt Sel. Khoz. No. 4, 39-44 (1959).

A. A. Vorob'ev, "A note on the acceleration of relativistic electrons in the ionosphere, with their paths controlled by the geomagnetic field," Izvest. Vyssh. Ucheb. Zaved. Fizika No. 2, 171-172 (1959).

L. I. Gel'man and L. S. Borin, "Operating atomic-electric power generating stations in the USA," Energomashinostroenie No. 4, 43-48 (1959).

L. N. Gertsizger, "A remote-controlled gaussmeter," Pribory i Tekh. Éksp. No. 1, 33 (1959).

L. N. Gertsiger, "A telemetering arrangement for measuring the intensity of the magnetic field," Pribory i Tekh. Éksp. No. 1, 33-35 (1959).

B. N. Gershman, "Contribution to the kinetic theory of the propagation of magnetohydrodynamic waves in plasma," Izvest. Vyssh. Ucheb. Zaved. Radiofizika 1, 3-20 (1958).

G. V. Gordeev, "Effect of terminal boundaries on the rotation of a plasma in a magnetic field," Zhur. Tekh. Fiz. 29, 759-762 (1959)

Yu. G. Grigor'ev et al., "Contribution to the problem of the rational use of x-ray testing," Med. Radiologiya 4, 3-15 (1959).

A. V. Gurevich, "On the variation in the modulation of intense r-f waves in a plasma (ionosphere)," Izvest. Vyssh. Ucheb. Zaved. Radiofizika 1, 21-31 (1958).

V. V. Zheleznyakov, "On the interaction of electromagnetic waves in a plasma. "Izvest. Vyssh. Ucheb. Zaved. Radiofizika 1, 32-45 (1958).

V. S. Zavel'skii et al., "Conference on the use of radioactive isotopes and radiations in the automobile and tractor industry (Moscow, November, 1958)," Avtomob. i. Trakt. Promysh. No. 5, 42-44 (1959).

L. I. Zlobin et al., "Techniques for Measuring radioactivity in humans (review article)," Med. Radiologiya 4, 85-87 (1959).

L. I. Zlobin et al., "Behavior of certain types of phototube multipliers in a weak magnetic field," Pribory i Tekh. Éksp. No. 1, 140-141 (1959).

S. P. Kapitsa, "On one principle for bunching fast electrons," Zhur. Tekh. Fiz. 22, 729-731 (1959).

L. M. Kovrizhnykh and A. N. Lebedev, "Contribution to the theory of betatron capture," Zhur. Tekh. Fiz. 29, 732-737 (1959).

L. B. Koznova, "Effect of dose rate on the biological effect," Med. Radiologiya 4,48-52 (1959).

E. Koptelov, "The use of atomic energy for peaceful purposes," Stroitel' No. 5, 28-29 (1959).

A. A. Korzhev et al., "Health physics problems in the use of radioisotopes (in the petroleum industry)," Bezopasnost' Trude v Promysh. No. 4, 17-17 (1959).

V. V. Krotov, "Utilization of the strong-focusing principle for contouring electrical deflectors," Zhur. Tekh. Fiz. 29, 716 (1959).

V. P. Kuznetsov, "Radioactive elements and raising the cotton crop," Trudy Sredneaz. Nauchn.-Issle. Inst. Irrigatzii No. 97, 43-57 (1959).

P. I. Levin and V. I. Kuznetsov, "Use of radioisotopes for determining gas leakage sites in underground gas pipelines," Gorodskoe khozaistvo Moskvy No. 4, 19 (1959).

N. I. Leont'ev and Yu. K. Udovichenko, "The Omegatron," Pribory i Tekh. Éksp. No. 1, 101-105 (1959).

F. M. Lyass, "Viewing facility in a gamma-therapy cabinet." Med. Radiologiya 4, 87-88 (1959).

Yu. I. Moskalev, "Experiments on the distribution of Ce^{144} (in an organism)," Med. Radiologiya 4, 52-58 (1959).

G. F. Nevskaya, "Dosimetric characteristic of the GUT-Co-400-1 gamma instrumentation," Vestnik Rentgenol. i. Radiol. No. 2, 63-67 (1959).

T. A. Potapova and S. T. Prokhorov, "Use of radioactive tracers for the study of the distribution and behavior of impurities in alloy production," Tsvetnye Metal. No. 5, 78-80 (1959).

A. P. Salikov, "Centralized municipal space heating from atomic heat-power stations," Teploenergetika No. 6, 77-79 (1959).

Ya. A. Smorodinskii, "Spatial structure of the atomic nucleus," Priroda No. 6, 3-12 (1959).

I. E. Starik and K. F. Lazarev, "On the form of occurrence of uranium and thorium atoms in radioactive minerals," Radiokhimiya 1, 60-65 (1959).

V. G. Stepanov and V. S. Bezel', "On the possibility of exciting an electron plasma of high concentration by means of radioactive isotopes," Izvest. Vyssh. Ucheb. Zaved. Fizika No. 2, 36-38 (1959).

G. Tleubergenova, "Determination of the thorium-uranium ratio in minerals and ores using thick-layered photographic plates," Zhur. Anal. Khim. 14, 211-216 (1959).

Ya. B. Fainberg, "Variable-phase focusing in linear accelerators," Zhur. Tekh. Fiz. 29, 568-579 (1959).

Ya. B. Fainberg and M. F. Gorbatenko, "Electromagnetic waves in a plasma placed in a magnetic field," Zhur. Tekh. Fiz. 29, 549-562 (1959).

A. Henig, "Radioisotopes in civil engineering (articles from Brno, Czechoslovakia)," Nauka i Zhizn' No. 5, 65 (1959).

N. V. Churaev, "Use of radioactive tracers for the study of the performance of a drainage system (in peat bog workings)," Nauch. Doklady Vyssh. Shkoly. Gornoe Delo No. 1, 21-25 (1959).

N. I. Shapiro et al., "On the 'oxygen effect' observed in radiation injury to plant and animal cells," Doklay Akad. Nauk SSSR 126, 191-194 (1959).

C. Allain and P. Thome, "Deformation of fuel elements under radiation bombardment," Rev. met. 56, 443-450 (1959).

T. Allen et al., Phys. Rev. Letters 2, 383-385 (1959).

H. Atkinson, J. Appl. Phys. 30, 637-645 (1959).

H. Atkinson et al., J. Appl. Phys. 30, 646-649 (1959).

E. Bagge and L. Schmieder, "Study of spark counters," Atomkernenergie 4, 169-181 (1959).

J. Barker, Nuclear Power 4, 119-120 (1959).

B. Beaudry and A. Daane, Trans. Met. Soc. AIME 215, 199-203 (1959).

J. Beranek, "Basic economic problems involved in reprocessing spent fuel," Jaderna Energie 5, 117-123 (1959).

F. Bollenrath and K. Lindackers, "Effect of γ radiation on solids, particularly metals," Atomkernenergie 4, 201-203 (1959)

R. Bolles and N. Ballou, Nuclear Sci. and Eng. 5, 156-185 (1959).

W. Bratina, Canad. J. Phys. 37, 579-590 (1959).

C. Cawthorne, Nuclear Eng. 4, 263-265 (1959).

L. Cranberg and J. Henshall, J. Appl. Phys. 30, 708-710 (1959).

W. De Bear, Nucleonics 17, 108-109, 112, 113 (1959).

R. Deutsch, Nuclear Sci. and Eng. 5, 150-155 (1959).

J. Devvoght, Nuclear Sci. and Eng. 5, 190-194 (1959).

J. Dungey, Phil. Mag. 4, 585-593 (1959).

L. Dzung, "Thermodynamic factors in the choice of coolant for nuclear reactors," Industries Atomiques 3, 61-64 (1959).

D. Fair, Nuclear Power 4, 104-109 (1959).

H. Fickel and R. Tomlinson, Canad. J. Phys. 37, 531-536 (1959).

P. Fields et al., Arkiv. Fysik 15, 225-228 (1959).

A. Fraas, Nuclear Power 4, 118-119 (1959).

K. Geiger, Canad. J. Phys. 37, 550-556 (1959).

F. Gerard, "The EDF-1 and EDF-2 atomic power plants at Chinon," Industries Atomiques 3, 55-58 (1959).

W. Gillingham, Nuclear Energy Engr. 13, 250-253 (1959).

W. Gillingham, Nuclear Energy Engr. 13, 293-297 (1959).

F. Goulding, Nucleonics 17, 64-71 (1959).

J. Haefling and A. Daane, Trans. Met. Soc. AIME 215, 336-338 (1959).

M. Haissinsky, "Basic problems in the radiolysis of liquid solutions," Industries Atomiques 3, 37-46 (1959).

I. Halpern, Nuclear Phys. 11, 522-530 (1959).

W. Harris and I. A. M. A. Kingsley, Arch. Industr. Health 19, 540-565 (1959).

E. Harrison, Am. J. Phys. 27, 314-317 (1959).

J. Kittel and S. Paine, Nuclear Energy Engr. 13, 301-305 (1959).

W. Kliefoth, "New gas-cooled reactor projects," Atomkernenergie 4, 196-201 (1959).

D. Krucoff, Nucleonics 17, 100, 102, 104, 105, 106 (1959).

P. Kruger, Nucleonics 17, 116-118, 120, 122, 124, 126 (1959).

J. Kulp et al., Science 129, 1249-1255 (1959).

C. Lee, Science 129, 1280 (1959).

J. Lehmann, Rev. met. 56, 456-481 (1959).

R. Levy-Mandel, Industries Atomiques 3, 47-54 (1959).

S. Loh, Canad. J. Phys. 37, 619-635 (1959).

P. Margen, Nuclear Eng. 4, 259-262 (1959).

E. Martel, Science 129, 1197-1206 (1959).

K. McCollom 17, 72-79 (1959).

K. Meredith and M. Waldron, J. Inst. Metals 87, 311-317 (1959).

B. Mitra, Indian J. Phys. 33, 149-157 (1959).

A. Neyron, "Electric circuits used in the operation of an electromagnetic isotope separator," Industries Atomiques 3, 65-74 (1959).

Nuclear Power 4, 89-91 (1959).

Nuclear Power 4, 122-124 (1959).

R. Palange et al., Sewage and Industr. Wastes 31, 565-573 (1959).

M. Panyr, "Health system in laboratories and shops where hot substances are handled," Jaderna Energie 5, 161-164 (1959).

G. Perlow and A. Stehney, Phys. Rev. 113, 1269-1276 (1959).

J. Roalsvig et al., Canad. J. Phys. 37, 607-613 (1959).

A. Robson, Nuclear Power 4, 98-101 (1959).

R. B. Roof, Phys. Rev. 113, 820-825 (1959).

S. Rothman and E. Fisher, Nuclear Sci. and Eng. 5, 195-196 (1959).

G. Safford and E. Melkonian, Phys. Rev. 113, 1285-1293 (1959).

H. Sandmeier and D. O'Shea, Nuclear Sci. and Eng. 5, 186-189 (1959).

H. Schmidt, "The 10 Mw high-temperature 'dragon' reactor," Atomwirtschaft 4, 211-215 (1959).

M. Sempert, "Nondestructive materials-testing in the 31 Mev 'Brown Boveri' betatron," Atomwirtschaft 4, 201-210 (1959).

B. Sen, Indian J. Phys. 33, 158-164 (1959).

J. Sharpe, Nucleonics 17, 82-85 (1959).

J. Silar and J. Smola, "Scintillation α probe with large surface area," Jaderna Energie 5, 124-128 (1959).

J. Simorda, "Equipment for studying radiation processing of plastics and rubber," Jaderna Energie 5, 151-156 (1959).

N. Sjostrand, Arkiv. Fysik 15, 145-146 (1959).

N. Sjostrand, Arkiv. Fys. 15, 147-158 (1959).

R. Smallman and K. Westmacott, J. Appl. Phys. 30, 603-616 (1959).

M. Sodha, Phys. Rev. 113, 1163-1164 (1959).

E. Spalaris, Nuclear Eng. 4, 253-258 (1959).

W. Starr, J. Appl. Phys. 30, 594-595 (1959).

H. Stoddart, Nucleonics 17, 78-81 (1959).

K. Svoboda, "Some new techniques in studying the possibility of producing radioactive isotopes of high specific activity, based on utilization of the process of hot-atom chemistry accompanied by the (n, γ) reaction," Jaderna Energie 5, 157-160 (1959).

P. Thome and B. Bailly du Bois, Rev. met. 56, 451-456 (1959).

J. Tyror, Nuclear Power 4, 94-97, 124 (1959).

K. Van Duuren et al., Nucleonics 17, 86-94 (1959).

S. Walker and R. Pywell, Nuclear Energy Engr. 13, 261-266 (1959).

A. Willis, Trans. Met. Soc. AIME 215, 245-251 (1959).

E. Wilson, "Krypton-85 atomic light sources," Atomwirtschaft 4, 191-194 (1959).

RESEARCH by Soviet EXPERTS

Translated by Western Scientists

SPECTRA AND ANALYSIS

by A. A. Kharkevich

The first handbook directed toward acousticians and others working in those fields which require the analysis of oscillations—ultrasonics, electronics, shock and vibration engineering. This volume is devoted to the analysis of *spectral concepts* as they are applied to oscillations in acoustics and electronic engineering, and to a discussion of the methods of spectral analysis. Contents include KOTEL'NIKOV'S theorem for bounded spectra, the spectra and analysis of random processes, and (in connection with the latter) the statistical compression of spectra.

cloth **236 pages** **$8.75**

ULTRASONICS AND ITS INDUSTRIAL APPLICATIONS

by O. I. Babikov

This work is concerned with ultrasonic control methods which are applied in industry, and also with the action of high-intensity ultrasonic oscillations on various technological processes. Considerable attention is devoted to ultrasonic pulse methods of flaw detection and physicochemical research. It is an invaluable aid to scientific researchers, engineers, and technicians working in fields which make use of ultrasonic methods industrially, as well as being a convenient reference for a broad category of readers who might wish to become acquainted with the current state of ultrasonic instrumentation.

cloth **265 pages** **$9.75**

Tables of contents upon request

CONSULTANTS BUREAU

227 West 17th Street • New York 11, N.Y. • U.S.A.

RESEARCH BY SOVIET EXPERTS

Translated by Western Scientists

RADIATION CHEMISTRY
PROCEEDINGS OF THE FIRST ALL-UNION CONFERENCE
MOSCOW 1957

More than 700 of the Soviet Union's outstanding research scientists participated in this conference sponsored by the Academy of Sciences and the Ministry of the Chemical Industry. Each of the 56 reports read in the various sessions covers either the theoretical or practical aspects of radiation chemistry, and special attention is given to radiation sources used in radiation-chemical investigations. The general discussions which followed each report and reflected various points of view on the problem under analysis are also included.

PRIMARY ACTS IN RADIATION CHEMICAL PROCESSES	$25.00
RADIATION CHEMISTRY OF AQUEOUS SOLUTIONS (Inorganic and Organic Systems)	$50.00
RADIATION ELECTROCHEMICAL PROCESSES	$15.00
THE EFFECT OF RADIATION ON MATERIALS INVOLVED IN BIOCHEMICAL PROCESSES	$12.00
RADIATION CHEMISTRY OF SIMPLE ORGANIC SYSTEMS	$30.00
THE EFFECT OF RADIATION ON POLYMERS	$25.00
RADIATION SOURCES	$10.00

Individual volumes may be purchased separately

Special price for the 7-volume set $125.00

Tables of contents upon request.

CONTEMPORARY EQUIPMENT
FOR WORK WITH RADIOACTIVE ISOTOPES

Of the 110 isotopes produced in the USSR during 1958, 92 were obtained by neutron irradiation. The methods and technological procedures used in the production of isotopes and the preparation of labeled compounds from them are reviewed in detail. Shielding and manipulative devices for work with radioactive isotopes are illustrated as well as described fully. These collected reports are of interest to all scientits and technologists concerned with radioactive isotopes.

Tables of contents upon request.

Durable paper covers 66 pp. illus. $15.00

PRODUCTION OF ISOTOPES

The eighteen papers which comprise this volume were originally read at the All-Union Scientific and Technical Conference on the Application of Radioactive Isotopes, Moscow, 1957. The reports consider the problems and achievements of Soviet scientists in the production of radioactive isotopes by irradiation of targets in Soviet reactors and cyclotrons. Not only is this work of significance to producers of isotopes, but many of the papers will prove useful to isotope users as well.

Tables of contents upon request.

Durable paper covers 136 pp. illus. $50.00

Payment in sterling may be made to Barclay's Bank in London, England.

CONSULTANTS BUREAU

227 West 17th Street • New York 11, N.Y. • U.S.A.